TUDelft

Delft University of Technology

Energy flux method for identification of damping in high-rise buildings subject to wind

Sánchez Gómez, Sergio

Important note
To cite this publication, please use the final published version (if applicable).
Please check the document version above.

ENERGY FLUX METHOD FOR IDENTIFICATION OF DAMPING IN HIGH‑RISE BUILDINGS SUBJECT TO WIND

ENERGY FLUX METHOD FOR IDENTIFICATION OF DAMPING IN HIGH-RISE BUILDINGS SUBJECT TO WIND

Proefschrift

ter verkrijging van de graad van doctor
aan de Technische Universiteit Delft,
op gezag van de Rector Magnificus prof. dr. ir. T.H.J.J. van der Hagen,
voorzitter van het College voor Promoties,
in het openbaar te verdedigen op donderdag 21 maart 2019 om 12:30 uur

door

Sergio SÁNCHEZ GÓMEZ

Ingeniero Industrial,
Centro politécnico Superior, Zaragoza, España,
geboren te Reus, Catalunya.

Dit proefschrift is goedgekeurd door de promotor:

prof. dr . A.V . Metrikine

Samenstelling promotiecommissie:

Rector Magnificus,	voorzitter
Prof. dr. A.V. Metrikine,	Technische Universiteit Delft

Onafhankelijke leden:

Prof. ir. R. Nijsse	Technische, Universiteit Delft
Prof. dr. ir. A.R.M. Wolfert,	Technische Universiteit Delft
Prof. dr. M. Boltežar,	University of Ljubljana
Prof. dr. W. Lacarbonara,	Sapienza University of Rome
Prof. dr. A. Cunha,	University of Porto
Dr. ir. C.P.W. Geurts,	TNO

An electronic version of this dissertation is available at
`http://repository.tudelft.nl/`.

A mis padres y a Floor.

ACKNOWLEDGEMENTS

Writing these words, it seems that a very special and unique adventure has come to an end. I do not have enough words to express my gratitude to all the people who accompanied me in this adventure.

I begin with TNO, thanking Carine van Bentum for giving me the opportunity to work on this very interesting project, teaching me the demands and necessities of the building industry and especially for guiding me all these years. Thanks also to my TNO colleagues, Okke Bronkhorst and Jitse Pruiksma, for the long, challenging, interesting and inspiring discussions. A special mention goes to Johan Kraus, not only for his technical help but also for being a friend during the tough moments.

I would like to express my most sincere gratitude to my main supervisor, Andrei Metrikine. Thank you for enlightening me with so many good ideas and for sharing your knowledge which was a source of inspiration and encouragement. This work would have not been possible without you. I would like to thank my colleagues from the group of Structural Mechanics and Offshore Engineering for their help and support.

Many thanks to Prof. Walter Lacarbonara and Biaggio Carboni for hosting me at Sapienza University in Rome. They gave me the help and freedom to use their facilities and share in their knowledge providing a great contribution to this thesis.

I would like to take this opportunity to deeply thank Sven Lentzen who, even though he was not part of this work, was the person who first awakened my interest for research and encouraged me to walk this path. To all my friends that were there when I needed them, my most sincere thanks.

To my parents for giving me the opportunity to be who I am today, and the freedom to choose my own path with their unconditional support. To my family for their love and support.

Last but not least, I thank Floor. When I first embarked to this journey, everybody stated very clearly that this is a journey I must travel alone. You, Floor, are very much responsible for me taking this decision. However, I must say that I never felt alone. Somehow, you embarked to the same journey with me, and that really made the journey much easier. Thank you for sharing all the frustrations and successes. I cannot thank your love and support enough.

Sergio Sánchez Gómez
Delft, November 2018

SUMMARY

Buildings are becoming taller, lighter, slenderer. These changing characteristics make tall buildings more sensitive to environmental loads, including wind gusts. A building is considered "tall" when its height and slenderness influence the design. Given the demand of improving building performance, the serviceability limit state (SLS) has become the most important design criterion of tall buildings. The structural serviceability is directly related to the building motions generated by wind gusts. These motions can influence the well-being of the building occupants. Whereas the human perception of movement is related to the jerk sensation, acceleration is the widely accepted parameter for measuring comfort level. In literature, a few well-established criteria for determining human perception to building vibrations can be found. In this work, the van Koten criteria are used to study human perception of building vibrations, using data collected from full-scale measurements of several high-rise buildings in The Netherlands. Whereas results clearly show that acceleration levels are barely perceptible, people still often feel insecure in the interior of high-rise buildings, meaning that human perception is extremely subjective.

Dynamic systems are governed by their mass, damping, and stiffness. Damping can be understood as the energy dissipation in a system. Therefore, it determines the maximum acceleration that can be felt. Given its physical complexity, damping is the most uncertain parameter to be predicted. Presently, there are several damping predictors to determine damping in high-rise buildings. The resultant damping obtained by means of damping predictors is the result of the contribution of two main energy dissipation sources: the soil foundation interaction and the internal damping in the structure. Using these predictors, damping related to soil-foundation is a constant value, whereas structural damping increases with respect to the amplitude of vibration. Unfortunately, the use of these predictors result in large scatter compared to the experimentally identified damping values of buildings located in The Netherlands. Given that the parameters of these predictors are tuned based on full-scale experimental values, the discrepancy between experimentally identified damping of the buildings and the resultant values obtained by means of damping predictors is not easy to explain. In this work, a predictor based on the same principles, and tuned to fit the data collected from the full-scale measurements is presented and applied. Unfortunately, this predictor does not give enough insight to understand the behaviour of the dissipation mechanisms in a tall building.

It is therefore the aim of this work to develop a tool for better assessing the energy dissipation in high-rise buildings to improve damping prediction. In a tall building, there are three types of energy dissipation (i.e the structural energy dissipation; soil energy dissipation and energy dissipation caused by the wind around the building). In this work, the aerodynamic damping caused by the wind around a building is considered negligible. To get a better overall damping prediction, an attempt to identify the contribution of the different damping sources to the overall damping is carried out. However, given the fact

that wind loads cannot excite higher frequency modes in a tall building, the energy dissipation of specific areas of the structure cannot be adequately identified by using modal based techniques. Therefore, a different approach is needed to identify the energy dissipated in local areas without a modal description of the structure. In this work, the energy-flux analysis is proposed as a damping identification tool. This approach isolates a certain area of the structure to formulate an energy balance around it. The connection between this local area and the rest of the structure is made via the energy flux, which accounts for the energy coming in and going out of the local area. By doing this analysis, the energy dissipation of a local area can be identified. In Chapters 4 and 5, an energy-flux analysis is used to identify the energy dissipation in local areas of the structure. Then, a damping operator can be quantified. Another advantage of this approach is the added possibility of studying the behaviours of different damping operators by computing their energy dissipation. To validate the method two lab-scale structures, a lab-scaled beam, a lab-scaled steel-frame building and a full-scale high-rise building are used. This is done in the following manner. First, the structures are instrumented using accelerometers in the case of the lab-scale beam and accelerometers and strain gauges in the case of the lab-scale steel frame and high-rise building. Then, equivalent viscous damping is experimentally identified by means of the collected data. Second, a model representative of the structure to be analysed is developed. The model is made with continuous and discrete structural elements (e.g. beams, springs, dashpots). These models are used in order to interpret energy change, energy flux and dissipation energy. The energy balance can be formulated around a specific area of the model. Then, by making use of experimental data, the energy enclosed in this specific area can be computed, and energy dissipation can be identified. To compare percentages of critical damping, the energy dissipation is formulated in terms of a damping operator. This operator can be used to compute equivalent viscous damping, which makes use of the energy-flux analysis by comparing it to the experimentally identified equivalent damping values. Based on the results presented in this work, it is proven that this approach is a consistent framework for damping identification.

In Chapter 6, a basic model for tall-building damping assessment during the design phase is presented. The model combines different models. The cone model describes the soil-foundation interaction and a Euler-Bernoulli beam model represents the building. Assuming a small vibration field, the mechanism responsible for the energy dissipation in the building is presumed to be directly related to the building's deformation. Therefore, the influence of building damping is studied based on the bending of the beam model used to describe the building. This influence varies with the change in the building deformation caused by different foundation stiffnesses. Likewise, the influence of soil-building interaction damping varies when changing the soil-foundation stiffness. Results provide evidence that the soil-foundation interaction of tall buildings may play an important role in the overall damping identification for certain soil characteristics, like the ones present in The Netherlands.

CONTENTS

1

INTRODUCTION

1.1. A BRIEF HISTORY AND FUTURE OF HIGH-RISE BUILDINGS

Since the legendary Tower of Babel, humans have attempted to build taller and taller structures. It seems to be genetic. Give a child a set of cubes and she will try to pile them into a tower. Is it therefore intrinsic to the human behaviour? An answer to this question has not yet been given.

Over the years, construction philosophy has changed tremendously as shown in Fig. 1.1.
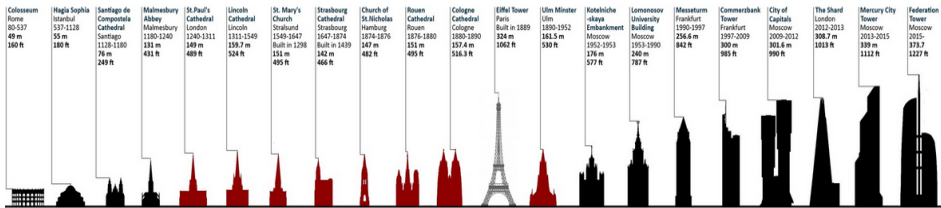
Figure 1.1: Historical evolution of structures in Europe.

Large structures were symbols of power and wealth in ancient cultures. They were often constructed for religious purposes, as perhaps the Egyptian were. Many, ancient constructions attract a great engineering interest, even today.

The first modern tall buildings were erected in Chicago and New York in the 1880s motivated by a great economic boom. Chicago's Home Insurance building, rising a mighty 12 stories, was completed in 1884 and it is widely considered to be the first tall building of the industrial era. Architects Louis Sullivan and Dankmar Adler were the first to use the term "tall office building" in 1896.

Owing to technological marvels, the development of technology and manufacturing techniques has grown rapidly. This has enabled architects and engineers to successfully accomplish engineering feats, erecting buildings higher than ever before while complying

1

with established safety regulations. These buildings are built primarily for office work activities. Entire business districts hence have evolved.

Later, motivated by the massive concentration of urban areas, tall buildings were adopted for housing. Thus, the number of high-rise buildings increased tremendously over the years, as shown in Fig. 1.2.
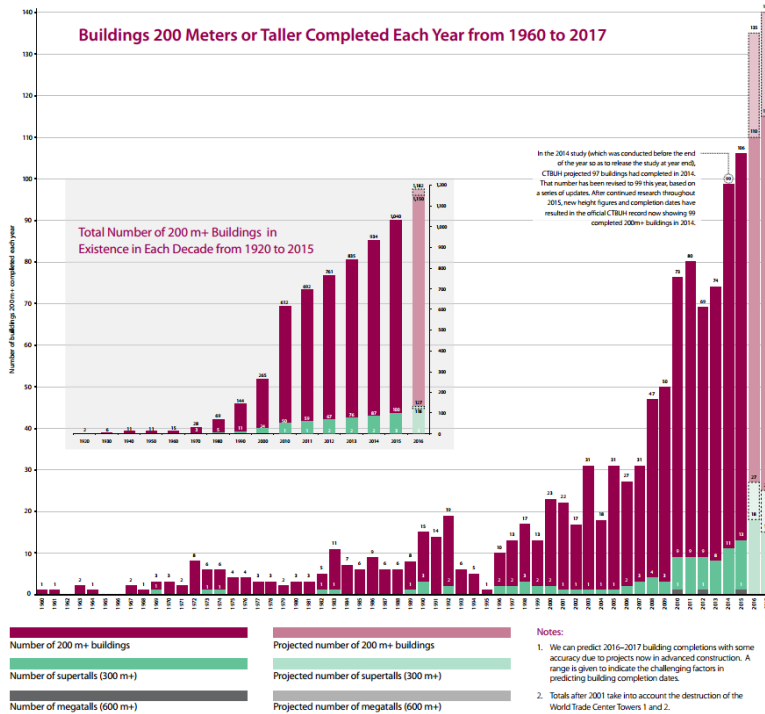
Figure 1.2: Number of 200 m+ buildings completed each year from 1960 to 2015, with projections through 2017 (CTBUH, 2015).

The term, "tall building" is not strictly defined. It depends on people's perception and the geographical location. However, from an engineering perspective, a building can be considered tall when its height and slenderness influence the design. Slenderness can be defined as the ratio between the height and the length of the base of the building. Generally, high-rise buildings have high slenderness ratios. This is opposite to the structures built decades and centuries in the past. The Egyptian pyramids, for example, have very low slenderness. For many years, the main demand of a building from the structural perspective was to ensure its structural integrity. Therefore, the main design criteria were related to the ultimate limit state (ULS). Nowadays, besides ensuring structural integrity, modern buildings must fulfil many other serviceability conditions related to comfort (e.g. air quality, sunlight). From the structural perspective, serviceability should ensure that building motions generated by environmental loads do not exceed certain thresholds that may affect the comfort of building occupants. Thus, the main design

criteria of modern tall buildings are more closely related to the serviceability limit state (SLS).

1.2. PROBLEM STATEMENT AND PURPOSE OF THE STUDY

Buildings are becoming taller, slenderer and lighter. The large increases in height make buildings more sensitive to dynamic loads, such as wind. Strong wind gusts make tall buildings oscillate. This phenomenon is commonly referred to as wind-induced vibrations. Generally, they do not lead to structural safety issues because of their generally low amplitudes. However, they can generate the perception of insecurity, creating a nuisance to the building occupants. The construction industry is therefore aware of the importance of providing high levels of comfort in terms of structural serviceability. Otherwise, common activities of living and working with others (Fig. 1.3) could not be carried out adequately.
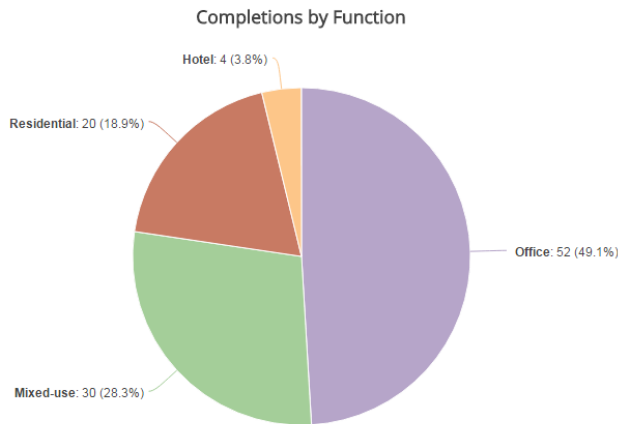
Figure 1.3: Number of 200 m+ buildings completed by sorted by function (CTBUH, 2015).

Structural serviceability is directly related to the accelerations experienced by buildings caused by environmental loads. Dynamic systems are governed by mass, stiffness and damping. Damping determines the maximum building accelerations, and thus becomes the main design parameter of SLS. Current damping predictors are quite rudimentary, leading to a large discrepancy between predicted and measured damping values. This is because generally damping cannot be determined until after the building is constructed.

In some cases, systems generating additional damping in a building are installed. Nowadays, there is a wide range of additional damping systems available. The selection depends on the structural system, the external forces (e.g. wind loading) and the required performance criteria of the building. To install an additional damping system, several essential aspects must be accounted for in the design of the building and the additional damping system. This makes the erection of buildings extremely expensive and introduces new unknowns to the building design. Therefore, in many situations, the installa-

1

tion of an additional damping system is not the most desirable solution.

In summary, erecting tall buildings that guarantee high standards of comfort has become a real challenge for structural engineers and constructors. It is therefore the purpose of this research to develop and provide tools to improve damping predictions in high-rise buildings during the design stage.

1.3. STATE-OF-THE-ART DAMPING PREDICTION OF TALL BUILD-INGS SUBJECT TO WIND

Currently, damping predictors exist to assess damping in buildings under wind excitations both in the Serviceability Limit State (SLS) and the Ultimate Limit State (ULS). Generally, wind-induced vibrations lead to low-amplitude oscillations related to the building's SLS. However, if wind gusts are sufficiently strong, ULS's related to large displacements can be reached. Davenport and Hill-Carrol [1] were the first to define intrinsic material damping, radiation damping, frictional damping and aerodynamic damping as primary mechanisms of energy dissipation in a tall building subject to wind loads. They suggested a damping predictor based on full-scale measurements for the SLS of tall buildings. Jeary [2, 3] also described different mechanisms of energy dissipation in a building and progressed further with the concept of amplitude dependent damping showing the relevance of the friction damping caused by crack formation during high amplitude vibrations and establishing a relationship between damping and vibration amplitude. He therefore distinguished three damping regimes with respect to the building vibration amplitude. The first regime is low-amplitude building vibration, where damping is constant with respect to the amplitude. In the second regime, total damping increases with the amplitude of building vibration. The third regime represents the very-high vibration amplitudes related to earthquake scenarios. Each damping regime is named as follows: low-amplitude plateau; non-linear regime and high-amplitude plateau. Accordingly, he developed a damping predictor based on full-scale measurements to determine damping in the low-amplitude plateau and the non-linear regime. The high-amplitude plateau cannot be described by his predictor, because it is out of the scope of wind-induced vibrations. Lagomarsino [4] claimed that the main mechanism of energy dissipation in steel buildings should be related to the friction in the joints. Thus, material damping was considered negligible. Consequently, he developed a theoretical model to predict friction damping in a building. However, he concluded that the model was not directly applicable, so he developed an empirical formula based on full-scale measurements. Tamura [5] formulated a damping predictor based on full-scale measurements and the Jeary's concept of amplitude-dependent damping, distinguishing between steel and concrete buildings. He also implemented a friction model to describe the primary mechanism of damping during wind induced vibrations [6, 7].

Whereas SLS-based knowledge in tall-building design has grown tremendously over the years, the above described damping predictors provide an unacceptable deviation with respect to the experimentally identified damping values of instrumented buildings located in The Netherlands. Therefore, erecting tall buildings that fulfil comfort demands remains a challenge.

1

1.4. RESEARCH OBJECTIVE AND APPROACH

It is known that damping determines accelerations experienced by the building during the vibration process. Furthermore, exceeding certain acceleration thresholds may lead to a nuisance for the building inhabitants. It is therefore the aim of this work to improve damping prediction in tall buildings by studying the contribution of the various damping sources activated during building vibration to the total damping.

From the literature, it is reasonable to distinguish the sources of energy dissipation in a building, as described in Fig. 1.4

MLBS: Main load bearing structure

NSE: Non-structural elements

Aero: Aerodynamic load

SSI: Soil-Structure interaction
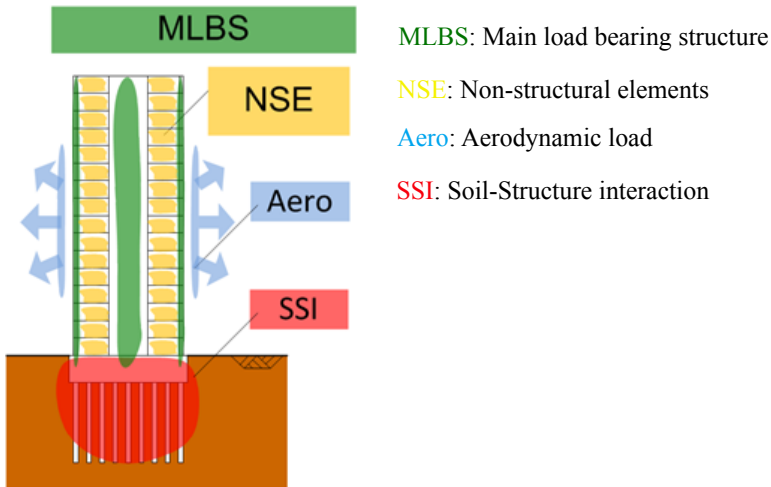
Figure 1.4: Sources of energy dissipation in a tall building.

Each energy dissipation source described in Fig.1.4 may be governed by one or more damping mechanisms. The main load-bearing structure (MLBS) dissipates energy at the material level caused by the deformation of the material. If large deformations occur, cracks in the material can appear, creating an additional source of energy dissipation to non-linear damping. The same behaviour is expected from the non-structural elements and joints. At low vibration amplitudes these elements help to dissipate energy via simple deformation. However, when vibration amplitudes are sufficiently large, non-linear behaviour, caused by friction between surfaces, is expected. With soil-structure interaction (SSI), two main mechanisms of energy dissipation can be distinguished. Wave radiation occurs when building vibrations excite waves in the soil, and material damping occurs with the dissipation of energy due to the friction between the soil particles. Aerodynamic damping is introduced by the wind surrounding the structure, and it is the most extensively studied one [1, 8].

To improve damping prediction, problem simplification by identifying the contribution of each damping source separately is called for. Unfortunately, this is not straightforward

1

with current modal based identification techniques, because they do not allow identification of energy dissipated in a specific structural location, unless sufficient number of modes are included. However, the higher modes are difficult to measure.

To deal with this drawback, energy-flux analysis is developed and used in this thesis. The energy flux is a well-established concept in several research fields [9–19], but not in the field of structural mechanics. The energy-flux analysis for damping identification may be seen therefore as a novel approach. This method allows us to isolate certain parts of the structure accounting for the energy exchange by means of the energy flux. Having computed the energy content of a specific part of a structure, and the energy exchanged at chosen boundaries, the energy dissipated within those boundaries can be computed. Then, a damping force based on the computed energy dissipation can be determined.

In this work, energy-flux analysis is first applied for damping identification on a lab-scale beam. Then, a more complex lab-scale structure is used for identification of energy dissipation at the connections. Finally, the energy method is used to study the damping contributions of the foundation and superstructure in a full-scale structure. As a final contribution to this work, the combination of well-established models with experimental data is used to provide insight and to establish the basis for further research into the application of the method.

1.5. THESIS OUTLINE

This thesis contains two parts: experimental measurements and modelling, divided into seven chapters. Chapter 2 deals with experimental measurements and the definition of comfort criteria. Chapter 3 presents the groundwork for modelling. Chapters 4 and 5 present lab- and full-scale experiments with modelling. In Chapter 6, basic mechanical models are used for damping prediction at the design stage of a high-rise building.

Chapter 2 describes the measurement campaigns conducted for several buildings located in The Netherlands. Experimental data are presented using the power-spectral density (PSD) function for better comprehension. This helps us, identify the resonant frequencies of the buildings. To identify building damping, two techniques are used: half-power bandwidth (HPBW) method and the random decrement technique (RDT). The HPBW method is a technique based on a single-degree-of-freedom (SDoF) system in the frequency domain. Thus, only an equivalent damping value for the whole structure can be identified. The RDT is a time-domain technique with the ability to assess damping at a certain vibration frequency. The collected data from the measurements are used in analytical models for damping identification and comparisons. Well-established damping predictors are used to identify the effective modal damping of the instrumented buildings. Moreover, based on insight provided by the established predictors and the data extracted from instrumented buildings, a damping predictor is proposed. Finally, a relation between the measured accelerations and human vibration perception is made using established criteria.

In Chapter 3, beam models and the energy variation law for modelling high-rise buildings is described. Classical beam theory is used for this. Equations of motion and energy variation law are derived, making use of the Lagrange formalism. In this chapter, the focus is placed on the axial and flexural deformations, whereas a brief description of the Saint-Venant torsional theory is also given. The energy variation law is later used as the

1

groundwork for damping identification in high-rise buildings.

In Chapter 4, the energy-flux analysis is used to identify the overall damping of a lab-scale beam. The energy balance is formulated around the scale-beam, and the energy dissipated is quantified using the experimental data. The quantified energy dissipation is assumed to be caused by material damping, and the result is compared to damping identified directly (without the use of the energy-flux analysis) from experimental measurements. Second, damping in the joints of a lab-scale steel-frame structure is identified. In this case the energy balance is formulated in the vicinity of the joints of the structure to quantify the energy dissipated. Damping matrices are built from identified energy dissipation. Finally, the results are compared with the directly identified modal damping.

In Chapter 5, the energy dissipation in the superstructure and the soil-foundation interaction of a tall building located in The Netherlands is identified independently of each other by means of the energy-flux analysis. This is done by formulating the energy balance in the superstructure and the soil-foundation separately. For the energy balance, the energy-flux term connects these structural parts by accounting for the energy that flows from one part to another.

In Chapter 6, basic mechanical models of high-rise buildings are used to model high-rise buildings to study the damping contribution of different energy dissipation sources to the total damping. Thus, a beam model, combined with springs and dashpots attached at one end mimicking SSI, is used. The springs and dashpots representing the resistance and dissipative capacities of the soil are quantified by the cone model.

Chapter 7 provides the main conclusions of this thesis.

2

FULL-SCALE MEASUREMENTS

In this chapter, equivalent viscous damping ratios associated with lower vibration modes of several instrumented tall buildings subject to wind-induced vibrations in The Netherlands are identified by means of two techniques: half-power bandwidth (HPBW) and random decrement technique (RDT). The HPBW is a frequency-domain technique based on the dynamics of a SDoF system, in which an equivalent viscous damping at the resonance frequency is identified. RDT is a time-domain technique, from which an equivalent viscous damping at a specific mode can be identified. Two techniques are used, because they provide complementary insight and enable a comparison of the identified damping. A point of interest to structural engineers is that this method provides practical insights into damping prediction. It seems customary to first use available damping predictors to assess the usability of those in the instrumented buildings. Then, the outcome of the predictors with the damping identified by means of the RDT can be compared. Therefore, a damping predictor based on the collected data from the instrumented buildings is proposed.

Finally, the evaluation of the building's serviceability, per the measured accelerations in the instrumented buildings, is studied using the H. van Koten criteria. Thus, the impact of vibrations to the well-being of building occupants and the expected damages to the structure can be evaluated.

2.1. THEORY OF WIND-INDUCED VIBRATIONS

Structural vibrations originated by wind are caused by the wind velocity variations around the building. Wind velocity grows with altitude and decreases near the earth's surface because of obstacles. An illustration of wind-speed growth profile with respect to height is given in Fig. 2.1.

Wind speed comprises a mean and a fluctuating component, as shown in Figure 2.1. Thus, the wind pressure can be approximated as follows,

$$p_{\text{wind}} = \frac{1}{2}\rho_{\text{air}}\left(V(z) + \tilde{v}(z)\right)^2 \approx \frac{1}{2}\rho_{\text{air}}V(z)^2 + \rho_{\text{air}}V(z)\tilde{v}(z), \tag{2.1}$$

9

2
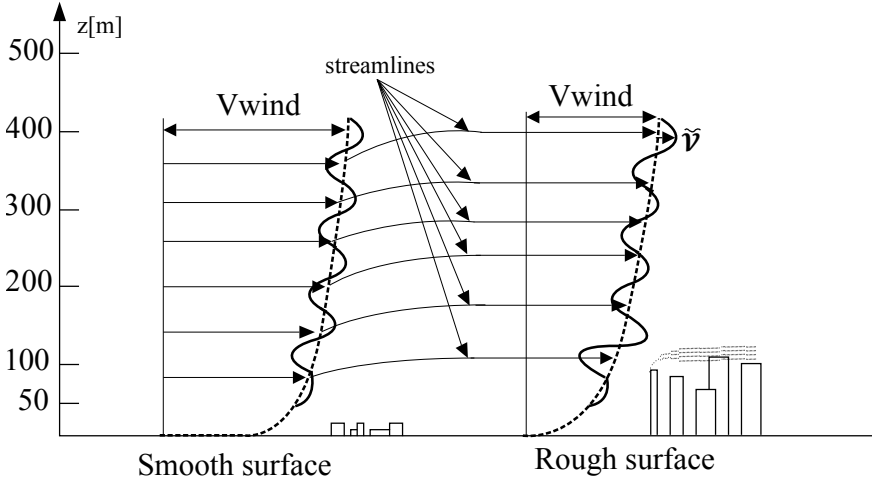
Figure 2.1: Wind profile.

where $V(z)$ is the mean wind-speed component, $\tilde{v}(z)$ is the fluctuating component; and it is assumed that $|\tilde{v}(z)| << V(z)$. An expression to assess the mean wind speed with respect to height can be formulated from the fluid dynamics theory, as shown in Eq. 2.2 [20].

$$V(z) = v(h_0) \frac{\ln\left(\frac{z-d}{z_0}\right)}{\ln\left(\frac{h_0-d}{z_0}\right)} \tag{2.2}$$

where $v(h_0)$ is the average wind speed, d is the height of the building, z_0 is the roughness determined by the terrain and h_0 is the reference height. This expression gives a good approximation for heights lower than 200m. Alternatively, the mean wind speed can be calculated using the following expression [20]:

$$V(z) = v(h_0) \left(\frac{z-d}{h_0}\right)^{\alpha} \tag{2.3}$$

where α is the power-law exponent. Forces acting upon structures from wind gusts appear in the three main directions: along-wind, cross-wind and torsional. Along-wind is important for buildings with rectangular shapes, whereas cross-winds affect circular-shaped buildings. Wind gusts contain a turbulent part associated with the mean wind speed, as shown in Fig. 2.1. This turbulence is largest in the direction of the mean wind speed. However, it is present in all directions. It is convenient for design purposes to compute the turbulent part of the wind in the frequency domain. Several researchers [21] have developed analytical expressions for along-wind amplitude spectrum responses. In Eurocode EN 1991-1-4, the frequency spectrum is described by Eq. 2.4 [22].

$$\frac{S_L(f,z)f}{\sigma_L^2} = \frac{6.8 f_L(f,z)}{(1 + 10.2 f_L(f,z))^{\frac{5}{3}}} \tag{2.4}$$

where f is the frequency in Hertz. Then,

$$\sigma_L^2 = 5.13 \left(\frac{z_0}{0.05}\right)^{\alpha} \tag{2.5}$$

and

$$f_L(f,z) = \frac{f L(z)}{V(z)} \qquad L(z) = 300 \left[\frac{z}{200}\right]^{\alpha} \qquad \alpha = 0.67 + 0.05 \ln(z_0). \tag{2.6}$$

The Solari spectrum, computed by means of Eq. 2.4, is shown in Fig. 2.2.
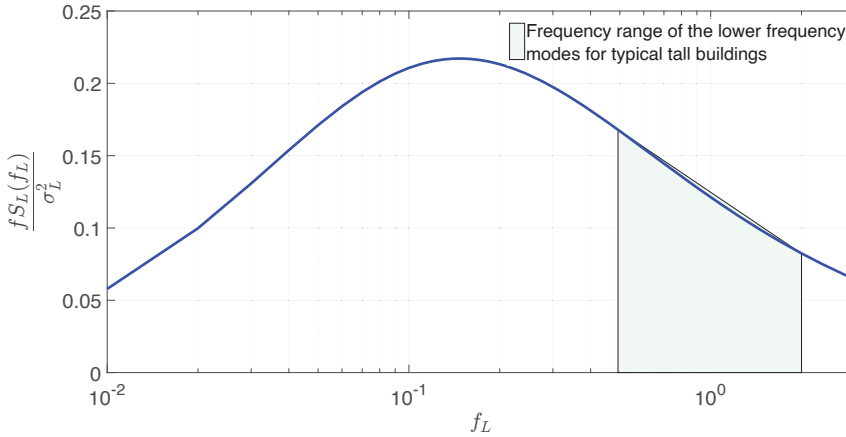
Figure 2.2: Solari spectrum amplitude.

From Fig. 2.2, it can be noted that the frequencies enclosed in the tail of the spectrum coincide with lower-frequency modes for typical tall buildings. Whereas these modes are enclosed within the low-energy content of the spectrum, the energy is sufficient to make the buildings vibrate. Thus, if the frequency of the excitation load coincides with a natural frequency of the structure, the latter may resonate without the need of introducing large-energy content. To use the Solari spectrum as an input to perform calculations of wind-induced vibrations, the term, $S_L(f)$ should be computed. For a typical tall building, this results in negligible energy content in frequency ranges larger than 2 Hz. Consequently, higher frequency modes of tall structures are not excited. This behaviour can be observed in the performed measurements shown in Section 2.4, where only the fundamental modes of each vibrational direction (two translational directions and torsion) are identified, whereas the higher modes are hidden in the measurement noise.

2.1.1. WIND-INDUCED ACCELERATIONS IN STRUCTURAL DYNAMICS

Generally, tall structures are designed with rectangular shapes. Thus, along-winds generate the largest building accelerations. Tall structures are usually modelled by means of an SDoF system for dynamic analysis. The equation of motion for a structural system subject to a general load can be described as shown in Eq. 2.7.

$$\ddot{x}(t) + 2\xi\omega_0\dot{x}(t) + \omega_0^2 x(t) = \frac{F(t)}{M} \tag{2.7}$$

with,

$$\omega_0 = \sqrt{\frac{K}{M}} \qquad \text{and} \qquad \xi = \frac{C}{C_r} = \frac{C}{2\sqrt{KM}}, \tag{2.8}$$

where M is the mass, K is the stiffness, ξ is the damping ratio and $F(t)$ represents a generalized external load. For a system subject to wind loading, the external force, $F(t)$, can be formulated by means of the fluctuating part of the wind, as follows:

$$F(t) = \rho_{\text{air}} C_{\text{D}} A V \tilde{v}(t), \tag{2.9}$$

where $F(t)$ results from multiplying the fluctuating part of the wind-pressure equation (Eq. 2.1) by the building area, A, and introducing a drag coefficient, C_{D}. The spectral density $S_{\text{F}}(\omega)$ of the wind force is obtained by assessing the auto-correlation function $R_{\text{F}}(\tau)$ of the force, $F(t)$.

$$R_{\text{F}}(\tau) = \lim_{T \to \infty} \frac{1}{T} \int_{-T/2}^{T/2} F(t)F(t+\tau)d\tau = \rho_{\text{air}}^2 V^2 A^2 C_{\text{D}}^2 \tilde{v}(t)\tilde{v}(t+\tau) \tag{2.10}$$

By applying the Fourier transform to Eq. 2.10, the following expression can be written:

$$S_{\text{F}}(\omega) = \int_{-\infty}^{\infty} R_{\text{F}}(\tau)e^{-i\omega\tau}d\tau = \rho_{\text{air}}^2 V^2 A^2 C_{\text{D}}^2 S_{\text{u}}(\omega) \tag{2.11}$$

where $S_{\text{u}}(\omega)$ is the spectral density of the turbulent wind speed and ω is the circular frequency ($\omega = 2\pi f$). In practice, the aerodynamic admittance, χ^2, is used to account for the incomplete coherence of the wind loads in space and the disturbance of the wind by presence of the building [23]. In Eurocode EN 1991-1-4, this is expressed as:

$$\chi^2 = R_h R_b, \tag{2.12}$$

where

$$R_h = \frac{1}{\eta_h}\frac{1 - e^{-2\eta_h}}{2\eta_h^2}; \qquad R_b = \frac{1}{\eta_b}\frac{1 - e^{-2\eta_b}}{2\eta_b^2}; \tag{2.13}$$

and

$$\eta_h = \frac{4.6fh}{Vh_0}; \qquad \eta_b = \frac{4.6fb}{Vh_0}, \tag{2.14}$$

where h is the building height, and b is the building width. Alternatively, an empirical expression, for a flat plate, suggested by Vickery [24] is described in Eq. 2.15.

$$\chi = \frac{1}{1 + \left[\frac{2f\sqrt{A}}{V(z)}\right]^{4/3}} \tag{2.15}$$

Introducing the aerodynamic admittance, Eq. 2.16 can be rewritten as

$$S_{\mathrm{F}}(\omega) = \rho_{\mathrm{air}}^2 V^2 A^2 C_{\mathrm{D}}^2 \chi^2 S_{\mathrm{u}}(\omega). \tag{2.16}$$

Now, applying the Fourier transform to Eq. 2.7, the following expression can be derived:

$$\tilde{x}(\omega) = H(\omega)\tilde{F}(\omega), \tag{2.17}$$

where the modulus of the mechanical admittance, $H(\omega)$, often called the frequency response function (FRF) appears as follows:

$$|H(\omega)| = \frac{1}{K}\frac{1}{\sqrt{\left(1 - \Omega^2\right)^2 + (2\xi\Omega)^2}} \quad \text{where} \quad \Omega = \frac{\omega}{\omega_0}. \tag{2.18}$$

Using random vibration theory [25], the power spectrum response of a system subject to wind loading can be determined as

$$S(\omega) = |H(\omega)|^2 S_{\mathrm{F}}(\omega). \tag{2.19}$$

The square of the absolute value of the mechanical admittance, $|H(\omega)|^2$, is nearly zero for most of frequency range. However, it is large near the natural frequency, ω_0, when the damping, ξ, is small, as shown in Fig. 2.3.
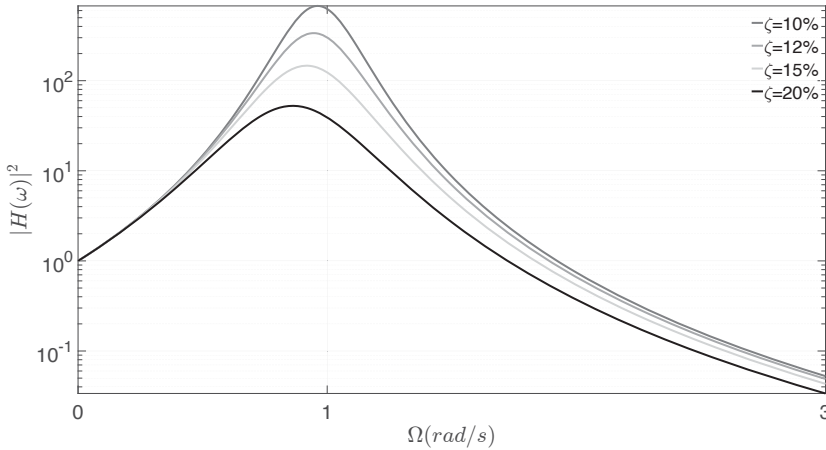
Figure 2.3: Square of the mechanical admittance amplitude of a SDoF system with various damping ratios.

Thus, the multiplication of mechanical admittance, $|H(\omega)|^2$, by the fluctuating part of the wind, $S_F(\omega)$, the response spectrum adopts the combined shape of both spectra, as shown in Fig. 2.4.
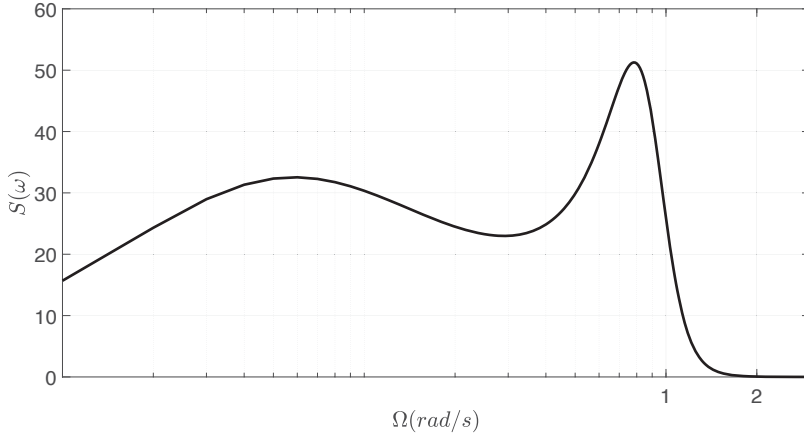
Figure 2.4: Response-spectrum amplitude resulting from multiplying the square of the mechanical admittance by the frequency-spectrum amplitude of the fluctuating part of the wind, based on the Solari spectrum.

The smallest hump at the lower frequency range shown in Fig. 2.4 corresponds to the higher- energy content of the wind spectrum, whereas the larger peak of the frequency-response spectrum corresponds to the resonance peak of the system.

2.2. DAMPING IDENTIFICATION TECHNIQUES

Standard identification techniques (e.g. HPBW, RDT) enable us to compute a damping ratio for each mode of the entire structure, if the modes are well-separated, because these techniques are based on a SDoF system and assume that a structural system is reduced to an equivalent mass, spring and dashpot system. More advance techniques based on multiple-degrees-of-freedom (MDoF) systems allow us to compute damping ratios for different parts of the structure. However, this is only possible if sufficient number of modes are included in the analysis. This is hardly applicable to tall structures subjected to wind, because higher frequency modes are not excited. Therefore, it is customary to use SDoF techniques for damping identification in tall buildings.

2.2.1. HPBW METHOD

The HPBW technique enables us to identify the natural frequency of a system based on the location of the spike in the frequency-response function. Computing the damping ratio of a SDoF system with viscous-damping is as follows. First, the equation of motion is formulated:

$$\ddot{x}(t) + 2\xi\omega_0\dot{x}(t) + \omega_0^2 x(t) = \frac{F(t)}{M} \qquad (2.20)$$

Applying the Fourier transform to Eq. 2.20 we obtain the following expression:

$$\left(-\omega^2 + \mathrm{i}2\xi\omega\omega_0 + \omega_0^2\right)\tilde{x}(\omega) = \frac{\tilde{F}(\omega)}{M} \tag{2.21}$$

where

$$\tilde{x}(\omega) = \int_{-\infty}^{\infty} x(t)e^{-\mathrm{i}\omega t}\mathrm{d}t \quad \text{and} \quad \tilde{F}(\omega) = \int_{-\infty}^{\infty} F(t)e^{-\mathrm{i}\omega t}\mathrm{d}t. \tag{2.22}$$

Solving Eq. 2.21 for ω_0^2 the following expression is obtained:

$$\tilde{x}(\omega) = \frac{\tilde{F}(\omega)}{K} \frac{1}{-\Omega^2 + \mathrm{i}2\xi\Omega + 1} \quad \text{where} \quad \Omega = \frac{\omega}{\omega_0}. \tag{2.23}$$

The PSD of a dynamic system is defined as

$$S(\omega) = \tilde{x}(\omega)\tilde{x}^*(\omega) = |\tilde{x}(\omega)|^2 = \left(\frac{|\tilde{F}(\omega)|}{K}\right)^2 \frac{1}{|\Omega^2 - 2\mathrm{i}\xi\Omega - 1|^2}. \tag{2.24}$$

The quality factor and the resonant frequency of a damped system are defined as

$$Q = \frac{\Delta\Omega_{\frac{1}{2}}}{\Omega_{\mathrm{res}}} = \frac{\Omega_{\frac{1}{2}}^+ - \Omega_{\frac{1}{2}}^-}{\Omega_{\mathrm{res}}}; \quad \Omega_{\mathrm{res}} = \sqrt{1 - 2\xi^2}, \tag{2.25}$$

where $\Omega_{\frac{1}{2}}^+$ and $\Omega_{\frac{1}{2}}^-$ correspond to the frequencies at which the PSD function is half of the maximum value. After some manipulations of Eqs. 2.24-2.25, a general expression for the damping ratio of a SDoF system can be obtained in terms of the quality factor.

$$\xi = \frac{1}{\sqrt{2}}\sqrt{\frac{\sqrt{-Q^4 + 4Q^2 + 4} - 2}{\sqrt{-Q^4 + 4Q^4 + 4}}} \tag{2.26}$$

Generally, for low-damped systems, it can be assumed that $Q << 1$. In these cases, the damping ratio can be approximated by the following expression:

$$\xi \approx \frac{1}{2}Q = \frac{\Delta\Omega_{\frac{1}{2}}}{2\Omega_{\mathrm{res}}}. \tag{2.27}$$

2.2.2. RDT

RDT was developed by Cole in the 1960s [26, 27]. It is based on the logarithmic decrement technique [28], which allows calculation of the equivalent viscous damping ratios of an SDoF system. An exponentially decaying response is achieved by allowing a system to vibrate freely. The logarithmic decrement technique is not directly applicable for damping identification in buildings subject to wind loads, because wind-loading does not produce exponential decay responses in buildings during vibration. However, by using the RDT, the exponential decay response can be recovered from a random system response.

Principle of RDT

The fundamental principle of RDT is based on the fact that the dynamic response of a linear system is composed by the sum of a free $x_h(t)$ and a forced $x_p(t)$ responses. The free response depends on initial conditions of the system (i.e. displacements and velocities) and the forced response depends on external loads applied to the dynamic system. Therefore, the dynamic response of a linear system can be described in the following form:

$$x(t) = x_h(t) + x_p(t) = x_h^{x_0}(t) + x_h^{v_0}(t) + x_p(t) \tag{2.28}$$

To apply RDT, a finite uniform time segment of duration τ is chosen and a level-crossing x_0 is selected. Those time moments at which the signal crosses a predefined level $x(t_r) = x_0$ are considered as initial time moments. The parts of the signal, starting at each initial time moment, t_r, enclosed in a segment $x(t_r + \tau)$ are averaged and overlapped. This results in a function $\delta(\tau)$ as shown in Fig. 2.5.
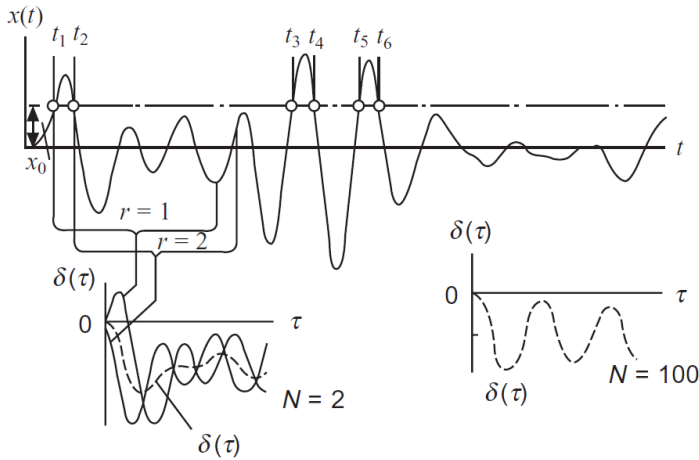
Figure 2.5: Time segments of a random response signal.

Thus, $\delta(\tau)$, can be defined as:

$$\delta(\tau) = \frac{1}{N} \sum_{r=1}^{N} x(t_r + \tau) \tag{2.29}$$

As the number of averages, N, increases, the part of the response corresponding to the initial velocity at $t = t_r$ as well as the part excited by the random external force vanish, such that:

$$\sum_{r=1}^{N} x_h(t_r + \tau)|_{v_0} \approx 0; \qquad \sum_{r=1}^{N} x_p(t_r + \tau)|_f \approx 0. \tag{2.30}$$

This behaviour is demonstrated in Fig. 2.6.
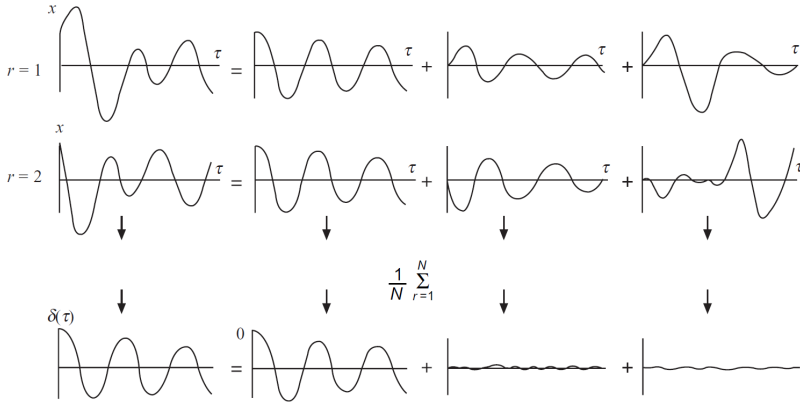
Figure 2.6: Averaged time segments of a random response signal.

Finally, the remaining part of the signal will be an exponentially decaying function, owing to its initial displacement, i.e:

$$x(t) \approx x_{\text{h}}^{x_0}(t) \approx \frac{1}{N} \sum_{r=1}^{N} x(t_r + \tau) \qquad (2.31)$$

An equivalent viscous damping ratio can be evaluated from the exponential decay function by means of the following expression:

$$\xi = \frac{1}{\sqrt{1 + \left(\frac{2\pi}{\ln(x_n/x_{n+1})} \right)^2}} \qquad (2.32)$$

where x_n and x_{n+1} represent the amplitude of two successive peaks. If the crossing points x_0 are set at different levels, an equivalent viscous damping ratio with respect to each initial displacement x_0 can be identified. Relating each initial displacement to the vibration amplitude of a system an equivalent viscous damping with respect to the vibration amplitude is said to be identifiable [29–32].

2.3. BUILDINGS DESCRIPTION

Prior to this work, several tall buildings located in The Netherlands were instrumented by TNO, The Netherlands Organisation for Applied Scientific Research, and measurements were performed under relatively strong wind conditions. The measurements were carried out to identify the natural frequencies of the structures and the damping ratio associated to each frequency. To this end, accelerometers were used. The disposition of the accelerometers at each of the instrumented buildings was chosen such that the lower modes could be identified.

2.3.1. THE CHURCHILL TOWER

The Churchill Tower is a 70 m office building with 24 storeys. The building was erected in the early 70s and renovated 30 years later. The Churchill Tower is a concrete building with a rectangular shape. The horizontal stability of the building is achieved by the main core. The floors span from the main core to the external columns. The vertical loads on the floors are transferred to the hidden beams, as shown in Fig. 2.7. The beams transfer the loads to the columns and the core. These elements transfer the loads directly to the foundation.
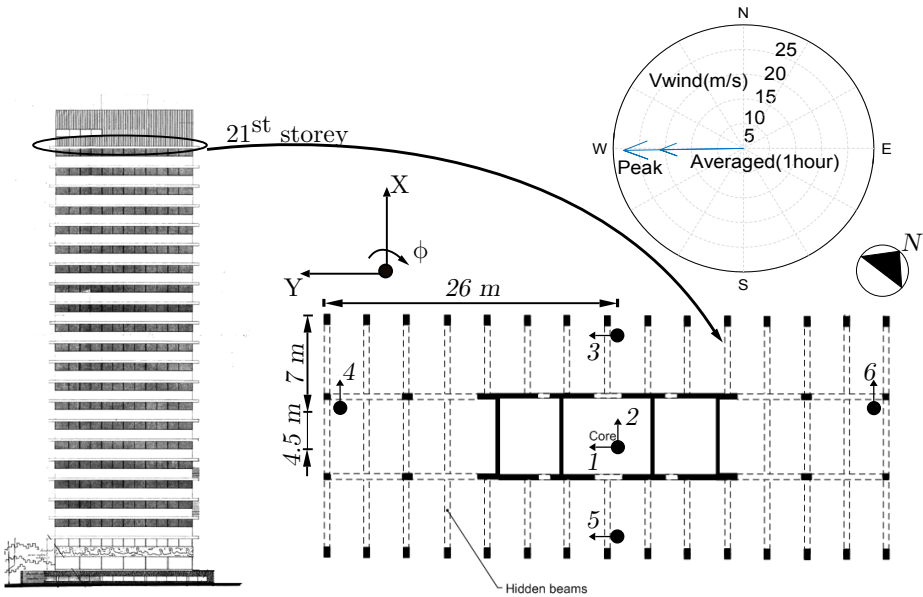
Figure 2.7: Churchill Tower layout, instrumentation set-up and measurement wind conditions.

The building was instrumented with six Sundstrand accelerometers at the highest possible location of the tower (storey 21st), as shown in Fig. 2.7. Accelerometers 1, 3 and 5 were placed along the short horizontal dimension measuring in the stiff direction. Accelerometers 1, 3 and 5 were placed along the short horizontal dimension in the stiff direction. Accelerometers 2, 4 and 6 were located along the long horizontal dimension measuring in the weak direction. Accelerometers 4 and 6 help identify the torsional vibration.

2.3.2. THE ERASMUS MEDICAL CENTER (E.M.C)

The new E.M.C is a building of an approximately 120 m high. The building has a rectangular shape. The horizontal stability of the building is accomplished by means of a concrete core and a tube, as shown in Fig. 2.8. The lower part of the concrete core is made in situ, whereas the larger part of the core, tube and floors are made with prefabricated concrete. The floors are connected to the core and the tube. The wind-induced

loads are transferred to the foundation via the tube principally, but also from the core.
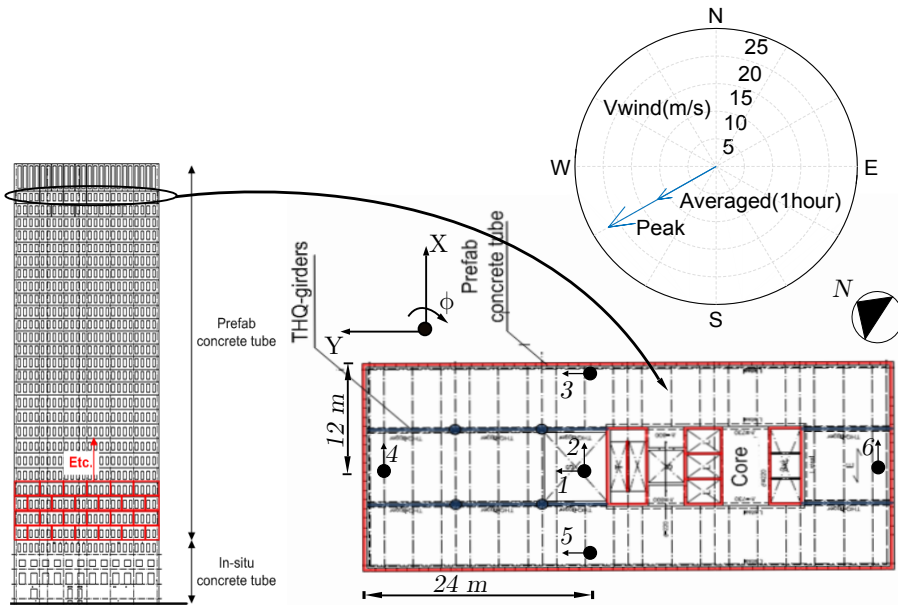
Figure 2.8: E.M.C. layout, instrumentation set-up and measurement wind conditions.

The building was instrumented with six Sundstrand accelerometers at the top storey, as shown in Fig. 2.8. Three accelerometers (1, 3, and 5) were placed along the short horizontal dimension measuring in the stiff direction. The other three accelerometers (2, 4, and 6) were located along the long horizontal dimension measuring in the weak direction.

2.3.3. THE MONTEVIDEO TOWER

The MonteVideo Tower is an approximately 150 m high multi-use building with 43 storeys. The tower of a rectangular shape was built using concrete and steel. The bottom part of the structure (up to the 2nd floor) is composed by a concrete core and a steel brace. In the middle part of the structure (from the 2nd to the 27th floor) horizontal stability is given by the concrete core. In the upper part of the structure (from the 27th floor to the top), the MLBS consists of a steel frame. Wind loads are transferred from the outside walls to the main concrete core through the concrete floors. The tower shares a foundation with an adjacent low-rise building separated by a small dilatation.

In this case study, the tower was instrumented at two levels using 11 Sundstrand accelerometers. Six were placed at the 27th floor, corresponding with the highest point of the concrete part of the structure. The other five were placed at the 42nd floor, corresponding to the highest accessible point of the building. In this case study, it becomes more difficult to intuitively identify the direction of vibration in the lower mode, owing to
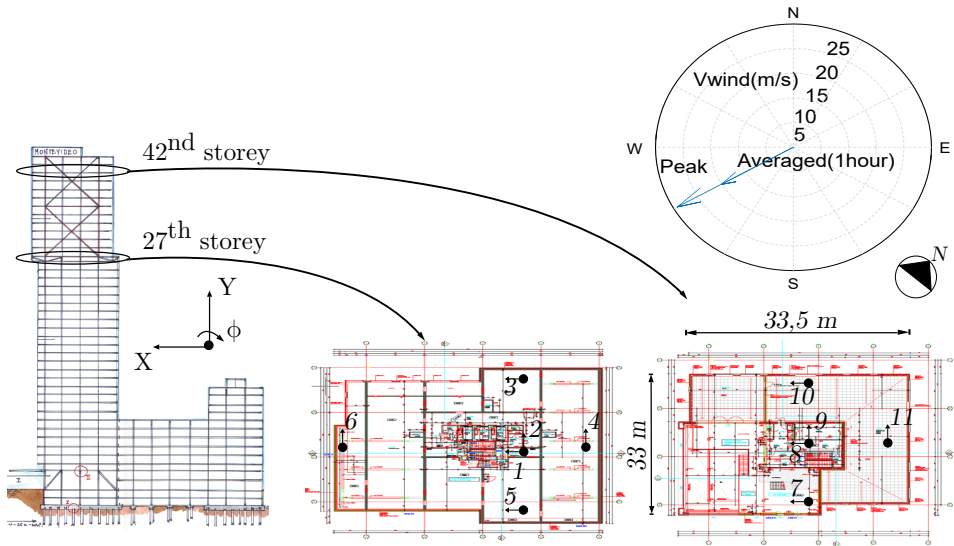
Figure 2.9: MonteVideo Tower layout, instrumentation set-up and measurement wind conditions.

the almost square shape of the building. However, the instrumentation strategy is similar to the previous case studies for identifying the lower modes. Accelerometers 7, 8 and 10 at the 42nd floor and accelerometers 1, 3 and 5 at the 27th floor were placed to measure the Y-direction, as shown in Fig. 2.9. Accelerometers 9 and 11 at the 42nd floor and accelerometers 2, 4 and 6 at the 27th floor were placed along the X-direction, as shown in Fig. 2.9.

2.3.4. The Oval Tower

The Oval Tower is a 25 storey office building 94 m high. It is named as such because of its oval shape. The MLBS consists of two concrete cores, and the floors span from the main core to the outside aluminium walls, as shown in Fig. 2.10.

The tower was instrumented making use of six Sundstrand accelerometers placed at the top storey. Despite the unusual shape of the building, the instrumentation strategy is similar to the ones used in previous case studies. Accelerometers 1, 3 and 6 were placed along the short horizontal dimension measuring in the stiff direction, and accelerometers 2, 5 and 6 were placed along the long horizontal dimension to measure accelerations in the weak direction.

2.3.5. The Hoftoren

The Hoftoren is a 142 m high office building with 31 storeys. The tower has an irregular shape and it is attached to a low-rise building 53 m high. The horizontal stability of the tower is provided by two concrete cores. The prefabricated concrete floors span from the concrete cores to the outside columns supporting the outside walls.

The tower was instrumented making use of six Sundstrand accelerometers at the rooftop.
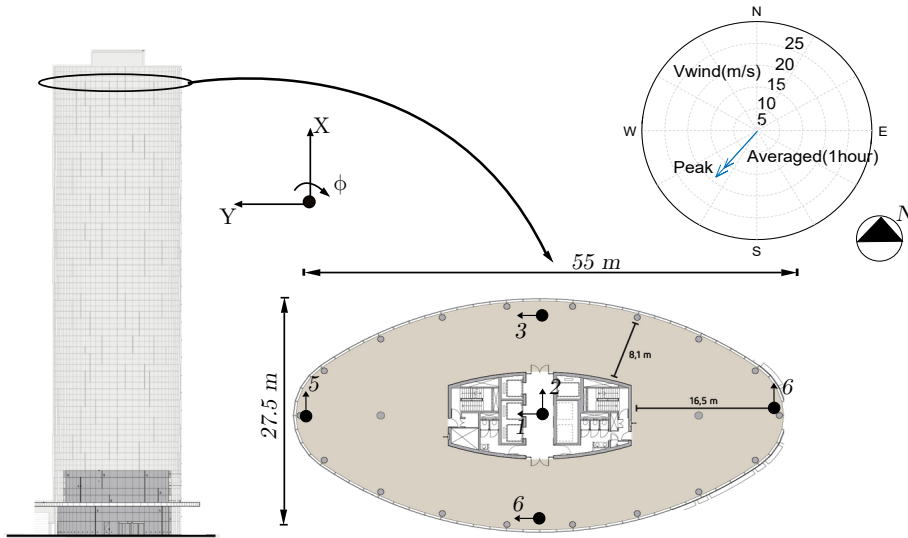
Figure 2.10: Oval Tower layout, instrumentation set-up and measurement wind conditions.

Accelerometers 2, 3, and 5 were placed along the long horizontal dimension to measure accelerations in the weak direction. Accelerometers 1, 4, and 6 were placed along the short dimension to measure accelerations in the stiff direction.

2.4. FIELD MEASUREMENTS

Acceleration measurements were carried out under strong wind conditions, as shown in Figs. 2.7-2.11. Specifications of the instrumentation are summarized in Table 2.1.

Acceleration data were recorded and stored in sub-samples of 10 min each. After some data processing, time traces of each sensor were transformed into the frequency domain for identification.

PSD functions of the measurements depicted in Fig. 2.12 show that the accelerometers recorded signals at all resonant frequencies. This means that the direction of the accelerometers did not correspond with the principal direction of the modal vibration. Therefore, modal analysis techniques based on SDoF could not be directly applied. To deal with this challenge, the accelerometers signatures were manipulated by means of rigid body kinematics, as described in Eq. 2.33.

$$\vec{v}_B = \vec{v}_A + \vec{\Omega} \times \vec{r}_A^B \tag{2.33}$$

Assuming the floors of the buildings behave as rigid bodies, the velocity at any point, $\vec{v}_B$, can be computed as the velocity at a certain point, $\vec{v}_A$, plus the angular velocity, $\vec{\Omega}$, times the distance from A to B ($\vec{r}_A^B$). This leads to the results shown in Fig. 2.13. Having separated the signals to a singular mode, SDoF-based techniques can be applied.

2
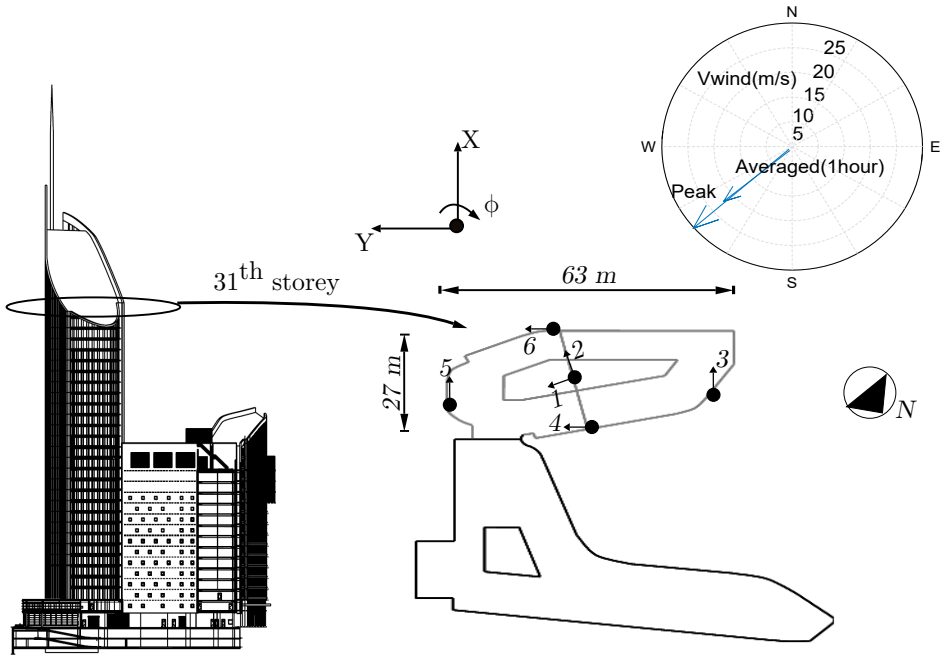
Figure 2.11: Hoftoren layout, instrumentation set-up and measurement wind conditions.
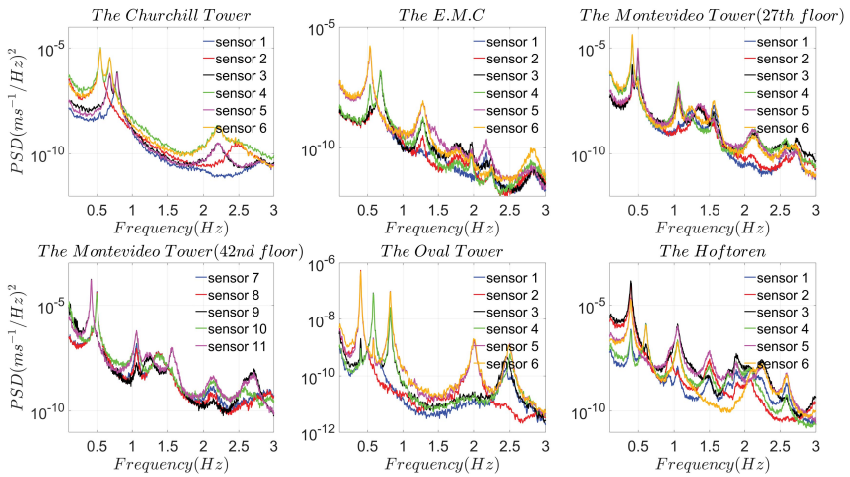
Figure 2.12: PSD function of the instrumented buildings.

	Sensors	Characteristics
The Churchill Tower	Accelerometers	Filtering 5Hz
Day: 25-11-2005		Sampling frequency 100 Hz
time: 10:00 - 12:00h am		Calibration range 19.62 V/m/s^2
		Voutput 9.81 V
The E.M.C	Accelerometers	Filtering 5Hz
Day: 6-9-2011		Sampling frequency 50 Hz
time: 18:00 to 20:00h pm		Calibration range 19.62 V/m/s^2
		Voutput 9.81 V
The Montevideo Tower	Accelerometers	Filtering 10Hz
Day: 18-11-2009		Sampling frequency 50 Hz
time: n.a		Calibration range 19.62 V/m/s^2
		Voutput 9.81 V
The Oval Tower	Accelerometers	Filtering 5Hz
Day: 4-1-2002		Sampling frequency 100 Hz
time: n.a		Calibration range 19.62 V/m/s^2
		Voutput 9.81 V
The Hoftoren	Accelerometers	Filtering 10Hz
Day: 31-1-2008		Sampling frequency 50 Hz
time: 14:00 to 17:00h pm		Calibration range 19.62 V/m/s^2
		Voutput 9.81 V

Table 2.1: Instrumentation description.
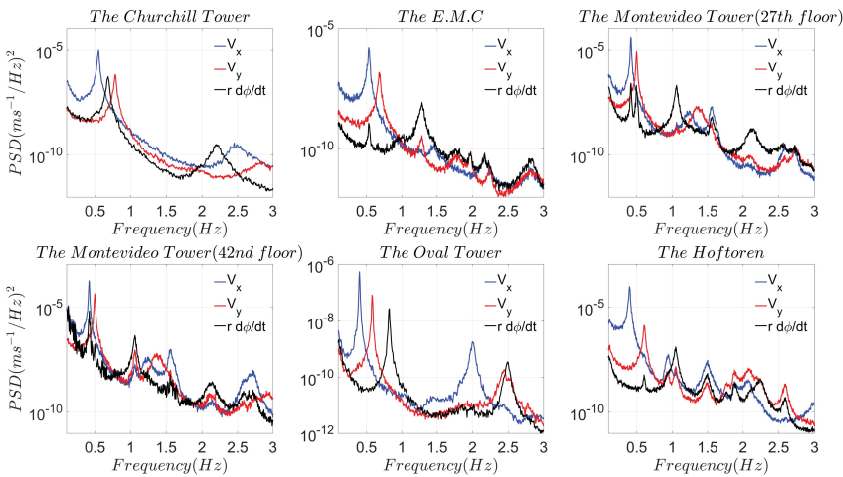
Figure 2.13: Single-mode PSD functions of the instrumented buildings.

The natural frequencies of the buildings can be straightforwardly identified by matching the spikes of the spectrum with the horizontal (frequency) axis. The equivalent viscous

damping ratio associated to each natural frequency is identified using Eq. 2.27. A summary of the identified damping ratios for each building is shown in Table 2.2.

	f_x[Hz]	f_y[Hz]	f_ϕ[Hz]	ξ_x%	ξ_y%	ξ_ϕ%
The Churchill Tower	0.54	0.79	0.68	1.9	1.6	2.5
The E.M.C	0.53	0.68	1.28	1.7	2.0	1.95
The Montevideo Tower	0.41	0.49	1.06	1.4	1.28	1.2
The Oval Tower	0.40	0.57	0.82	1.4	1.2	1.0
The Hoftoren	0.39	0.60	1.05	2.2	1.88	1.43

Table 2.2: Damping ratio of the lower modes of the studied buildings.

The subscripts x, y and ϕ , correspond to the X-direction, Y-direction and torsion, respectively. The RD technique enables us to identify the equivalent viscous damping ratios associated with each mode (natural frequency) with respect to the building acceleration. The identified damping ratios obtained by means of the HPBW and the RDT for the first mode (f_x) in the X-direction of the studied buildings are shown in Fig. 2.14.
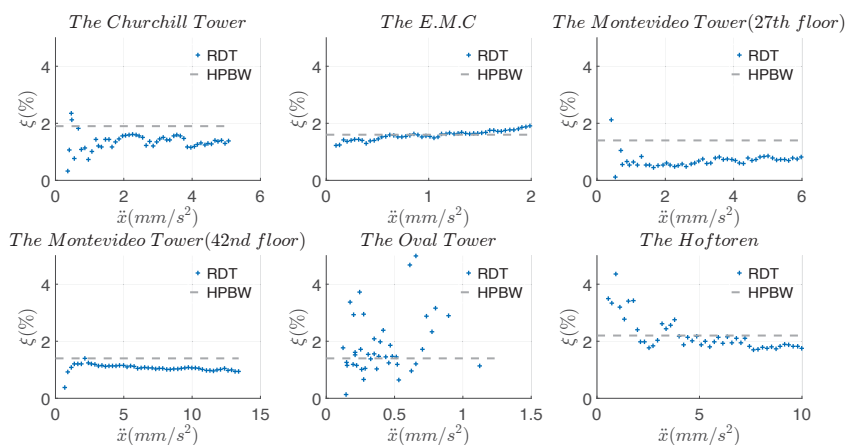
Figure 2.14: Damping identified in the first vibrational mode (f_x) of the instrumented buildings by means of the HPBW technique and the RD technique.

Figure 2.15 shows the identified damping ratios by means of HPBW and the RDT of the second vibration mode (f_y) in the Y-direction.
In Fig. 2.16, the damping ratios for the torsional vibration mode (f_ϕ), in the ϕ-direction, are identified.
In Figs. 2.14-2.16, the $\ddot{x}$, the $\ddot{y}$ and the $r\ddot{\phi}$ quantities of the horizontal axis represent the horizontal and torsional maximum accelerations at the measurement height in the X, Y and ϕ directions, corresponding to Figs. 2.7-2.11.The maximum accelerations in each direction were achieved, meeting the acceptable limiting factor demanded by the RDT for reliability of 100 averages over a time segment of the signal.
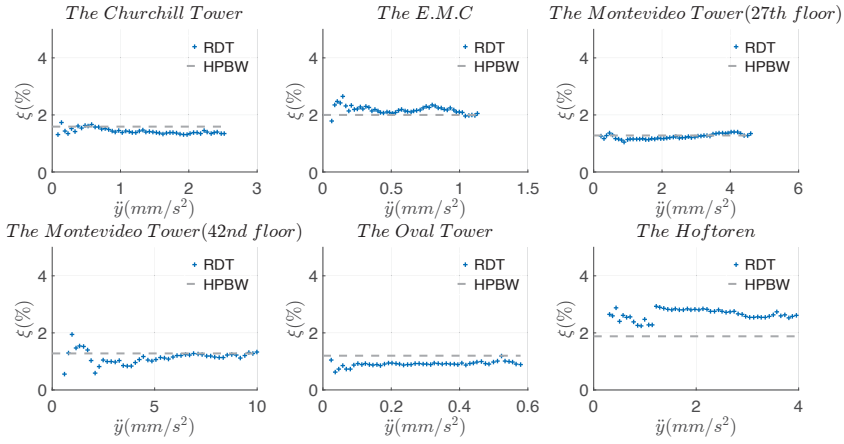
Figure 2.15: Damping identified in the second vibrational mode (f_y) of the instrumented buildings by means of the HPBW technique and the RD technique.
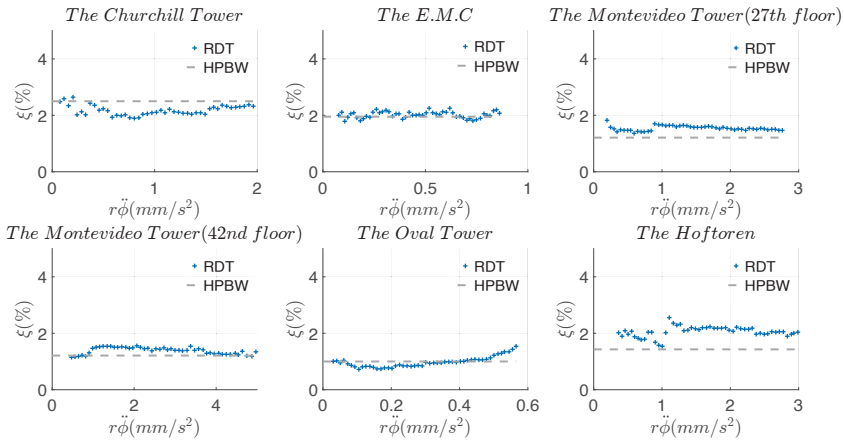
Figure 2.16: Damping identified in the third vibrational mode (f_ϕ) of the instrumented buildings by means of the HPBW and the RD techniques.

From Figs. 2.14-2.16, both identification techniques gave comparable results. Based on the RDT results, a constant damping ratio within the measured acceleration range is found. However, in the first mode of the E.M.C building, a slight damping increase with increasing acceleration was observed. In Fig. 2.14 the case of the Oval Tower shows a large scatter in the identified damping.

2.5. DAMPING PREDICTORS IN THE STUDIED BUILDINGS

Damping in high-rise buildings is a topic of great interest for structural engineers. This is because damping is the key parameter that limits the vibration amplitude in a building and helps to achieve the comfort level demanded by building occupants. However, making damping predictions during the design stage remains problematic, because damping has a very complex nature. In a tall structure, the overall damping is affected by several sources of damping. In this section the usability of several well-established damping predictors is tested in the instrumented high-rise buildings. Moreover, a damping predictor adjusted to the characteristics of the instrumented buildings and based on the existing predictors is proposed.

2.5.1. THE USE OF EXISTING DAMPING PREDICTORS

Damping in tall buildings has been studied extensively. Thus, several damping predictors have been developed. Principally, these predictors were developed for engineers to use during the design stage of a tall building. It seems straightforward to then compare the predicted damping of the studied buildings with that obtained by means of measurement. This comparison is performed using four damping predictors. The predictor developed by Lagomarsino [4] shown in Eq. 2.34 describes the Rayleigh-damping. It does not depend on the vibration amplitude.

$$\xi_{\text{Lago}} = \alpha f_n + \frac{\beta}{f_n} \tag{2.34}$$

where f_n is the fundamental frequency (Hz), and α and β are material-dependent constants. The Davenport's damping predictor [1] is described in Eq. 2.35.

$$\xi_{\text{Dav}} = A \left(\frac{\Delta}{H} \right)^n \tag{2.35}$$

where H is the building height, Δ is the design RMS horizontal vibration amplitude and A and n are material-dependent constants. Davenport and Lagomarsino damping predictors do not depend on vibration amplitude. Results of the damping prediction by means of the Lagomarsino and Davenport predictors are summarized in Table 2.3.

	$\xi_{\text{Dav}}\%$	$\xi_{\text{Lago}}\%$
The Churchill Tower	0.66	1.66
The E.M.C	0.55	2.12
The Montevideo Tower	0.7	2.5
The Oval Tower	0.55	1.8
The Hoftoren	0.68	2.39

Table 2.3: Damping ratio of the first mode calculated by means of the Davenport and Lagomarsino damping predictors for the studied buildings.

The other predictors used in this study are Jeary's and Tamura's damping predictors. Jeary developed his predictor based on two damping regimes: 0-amplitude (ξ_0), and the amplitude-dependent regime (ξ_I). The 0-amplitude regime might mislead the reader,

given that, at 0 amplitude, damping must be zero. This regime is actually for very low amplitudes of vibration. In this regime, damping is constant with respect to the amplitude of vibration. According to Jeary's theory, the overall damping in the structure is caused by the construction material, given that the material behaves elastically. The energy is dissipated because of the strain in the material and the large structural elements that move relative to each other. Several observations made by Jeary support the theory of the existence of damping associated with very-low vibration amplitudes. These observations also suggested that, at these amplitudes, damping correlates with the fundamental frequency. Therefore, the following expression is used for the Jeary damping predictor to compute the 0-amplitude damping:

$$\xi_0 = f_n = 0.01\frac{46}{H} \qquad (2.36)$$

where, f_n is the fundamental frequency of vibration that can be estimated by means of the empirical formula derived by Ellis [33]. However, according to Tamura's theory, the frequency-dependent damping term is related to radiation damping, owing to SSI, which dominates for lower-rise buildings with shorter frequency periods. The amplitude dependent regime is defined by Jeary as a non-linear region caused by the formation and rapid elongation of micro-cracks in the material. Elongated cracks create a sink for energy loss. Therefore, this involves friction damping. The amplitude-dependent damping term in Jeary's damping predictor can be computed as shown in Eq. 2.37.

$$\xi_I = 10^{\frac{\sqrt{D}}{2}}\frac{x}{H} \qquad (2.37)$$

The full damping predictors developed by Jeary and Tamura are described in Eqs. 2.38-2.40, respectively.

$$\xi_{Jeary} = \xi_0 + \xi_I = 0.01 f_n + 10^{\frac{\sqrt{D}}{2}}\frac{x}{H} \qquad (2.38)$$

and

$$\xi_{Tamura} = 0.014 f_n + 470\frac{x}{H} - 0.0018; \quad \text{for} \quad \text{RC buildings} \qquad (2.39)$$

$$\xi_{Tamura} = 0.013 f_n + 400\frac{x}{H} + 0.0029; \quad \text{for} \quad \text{steel buildings} \qquad (2.40)$$

where x represents the horizontal vibration amplitude, and D is the dimension of the foundation in the direction of motion. Besides frequency, building height and vibration amplitude, Jeary pointed out that the dimension of the periphery of the foundation of the building plays an important role in damping prediction. He included the dimension of the foundation in the direction of the motion of the mode of vibration. In the formula, the damping in the foundation could not be independently accounted for. Even so, it is included in the formula.

Tamura's damping predictor established a difference in predicting damping between steel and RC buildings. However, these predictors have some restrictions regarding the building height and the vibration amplitude. The predictor devoted to RC buildings

works in the range of 10m ≤ H ≤ 130m and x/H ≤ 2x10^{-5}. In the case of steel build-
ings, the predictor works in the same range of dimensionless amplitude, x/H, as for the
RC buildings. The height should be enclosed between 30m ≤ H ≤ 200m.
Figure 2.17 shows the damping identified by the RDT, Jeary's, Tamura's, Davenport's and
Lagomarsino's damping predictor for the studied buildings.

Figure 2.17: Damping ratio of the first mode calculated with Jeary's and Tamura's damping predictors com-
pared to the damping identified by means of RDT in the instrumented buildings.

To compute the equivalent damping ratio for the dimensionless horizontal vibration am-
plitude of the studied buildings represented by the + in Fig. 2.17, the signals are first
registered by the acceleration measurements in the X-direction. They are numerically
integrated to obtain displacements signals. Then, the RDT is applied, and the resultant
damping is plotted, making the horizontal amplitude of vibration dimensionless with
respect to the building height. The same dimensionless amplitude range was later used
to compute damping by means of Jeary's and Tarmura's predictor. With the geometrical
quantities of each building, a damping value at each dimensionless amplitude can be
computed by means of Eqs. 2.38-2.40, as shown in Fig. 2.17. The single damping value
obtained by Davenport's and Lagomarsino's predictor is plotted in Fig. 2.17 for com-
parision. Figure 2.17shows how the results obtained by means of Jeary's and Tamura's
damping predictors are comparable. However, when comparing them with the outcome
of the experimentally identified damping, it can be noted that the damping predictions
underestimate the overall measured damping, specifically the zero-amplitude regime.
This could mean that the influence of foundation damping is more dominant than ex-
pected in other locations for the 0-amplitude damping, ξ_0, according to Tamura's theory.
Examining the amplitude-dependent term, ξ_I, the slope generated by Tamura's predic-
tor at higher amplitudes seems to be larger than the slope obtained by the RDT, which
is nearly zero. However, the slope obtained by means of the amplitude-dependent term
of Jeary's predictor seems to be smaller, almost plain for most of the cases, especially
at very-low amplitudes. Therefore, it behaves more in accordance with the identified

damping. However, in the instrumented buildings, no significant crack formation was identified, given the small amplitudes of vibration.

The damping obtained by means of Lagomarsino's predictor is comparable with the identified damping for the buildings with higher fundamental frequencies: Churchill and E.M.C towers. It overestimates other buildings having a lower fundamental frequency. Lagomarsino's predictor behaves as Rayleigh damping. Therefore, it computes a minimum damping at a natural frequency, and then increases with increasing or decreasing natural frequency. However, the studied cases show that buildings with lower natural frequencies do not necessarily have higher damping. Therefore, it may be concluded that these damping predictors are not appropriate for direct use when predicting damping in the tall buildings located in The Netherlands, where soils are soft.

2.5.2. A PROPOSED DAMPING PREDICTOR

It was shown above that the existing damping predictors are not suitable for directly predicting damping for the studied buildings. However, it has also been shown that the damping increase of the amplitude-dependent term of Jeary's damping predictor seems to be in accordance with the damping increase identified by means of the RDT for the studied buildings. Moreover, the Lagomarsino's predictor reproduces with reasonable accuracy the 0-amplitude damping for the buildings of higher fundamental frequency. Thus, an attempt to develop a more suitable damping predictor for the studied buildings by making use of the existing knowledge in damping prediction is made in this section. The predictor is therefore a combination of a modified 0-amplitude term using Lagomarsino's Rayleigh-damping concept and the amplitude-dependent term developed by Jeary. Thus, the proposed damping predictor is shown in Eq. 2.41.

$$\xi = \xi_0 + \xi_\mathrm{I} = 0.0035 f_n + \frac{0.0075}{\left(f_n\right)^p} + 10^{\frac{\sqrt{D}}{2}} \frac{x}{H} \begin{cases} p = 1 & \text{for} \;\; H \leq 120\text{m} \\ p = 0.8 & \text{for} \;\; 120\text{m} \leq H \leq 150\text{m} \\ p = 0.3 & \text{for} \;\; 150\text{m} \leq H \end{cases} \quad (2.41)$$

The proposed predictor is divided into two terms: the 0-amplitude term (ξ_0) and the amplitude-dependent term (ξ_I) proposed by Jeary. The main difference with respect to the existing predictors is in the 0-amplitude term. The definition of this term is inspired by the Rayleigh-damping term described by Lagomarsino. However, his damping model contains a major drawback for the direct utilization on the studied buildings: the increasing damping with decreasing fundamental frequency. This damping behaviour is definitely unobserved in the instrumented buildings. It was shown by Ellis [33] that the fundamental frequency of a tall building correlates with building height. Therefore, with the proposed predictor, a correction factor, p, was introduced to compensate. The constant values of the 0-amplitude term was fitted to the identified data. The following figure shows the damping predictions obtained by means of the proposed damping predictor and the comparison with the identified damping.

Looking at Fig. 2.18 the damping predicted by Eq. 2.41gives comparable results to the identified damping, except for the Oval Tower, which is still slightly off. However, for this case, the damping identified is relatively low compared to the other study cases. Furthermore, by looking at the damping identified by means of the HPBW, the damping
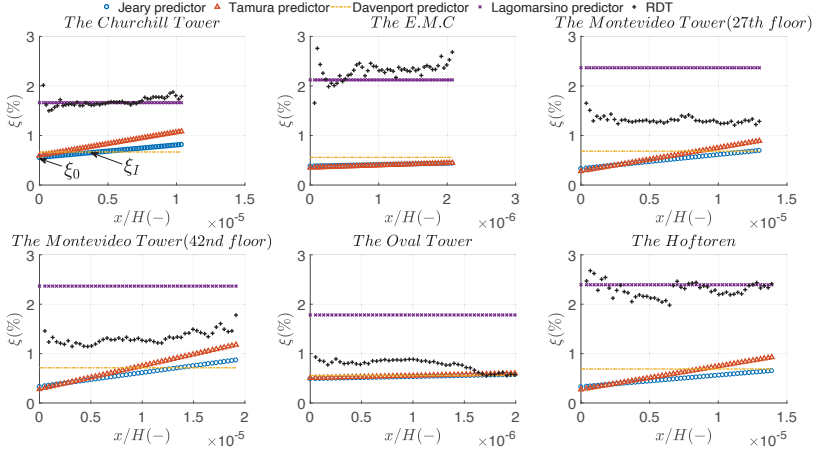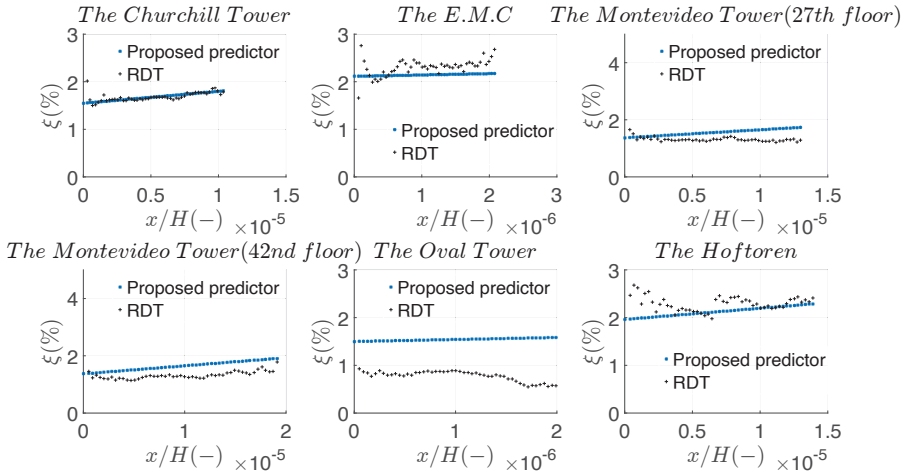
Figure 2.18: Damping ratio of the first mode calculated with the proposed damping predictor compared to the damping identified by means of the RDT in the instrumented buildings.

of the Oval Tower turns out to be comparable with the damping predicted by Eq. 2.41.

2.6. SERVICEABILITY LIMIT STATE IN WIND-INDUCED VIBRA-TIONS

The serviceability of a building can be associated with the comfort of the occupants, as with lighting and indoor air quality. The serviceability of the structure is related to building vibrations. The movement caused by external loads may influence the comfort of occupants, causing motion sickness. Historically, most research and codes were devoted to analysing building behaviour in the ULS, given that it may lead to structural damages and safety risks. However, owing to the development of new, stiffer and lighter building materials and an increase of height, buildings are more sensitive to wind-induced vibrations associated with SLS.

2.6.1. OCCUPANT REACTION TO BUILDING VIBRATIONS

During building vibrations, occupants are subject to this process, and it affects their well-being. Quite often, these sensations cause subjective feelings of insecurity. Research on human reaction to motions [34–36] has identified several factors that give rise to feeling of insecurity and, in some cases, sickness. These factors are listed below.

1. Type of motion

2. The frequency of vibration

3. Expectancy of motion

4. Personal Health

All these factors were identified via experiments. In practice, vibrations are identified by means of acceleration measurements. Therefore, it seems customary to relate human perception to vibrations in terms of motion displacement, velocity or acceleration. Some researchers have shown that human bodies adapt to constant acceleration. Therefore, jerk, which is the time derivative of the acceleration, seems to be the parameter responsible for the human perception of motion. Whereas jerk is the parameter responsible for motion, acceleration has become the accepted parameter to assess human perception of motion. In The Netherlands, limiting accelerations are described by different standards. For example, DIN 4150 Pt. 2 or the ISO 2631, is used, per H. van Koten in a TNO report [37]. These standards assess the limits of permissibility of acceleration within a frequency range. To assess the human perception of accelerations registered during the measurements in the case studies, the TNO standard drawn by H. van Koten is used. Figure 2.19 shows the accelerations registered in the X-direction of each instrumented building.
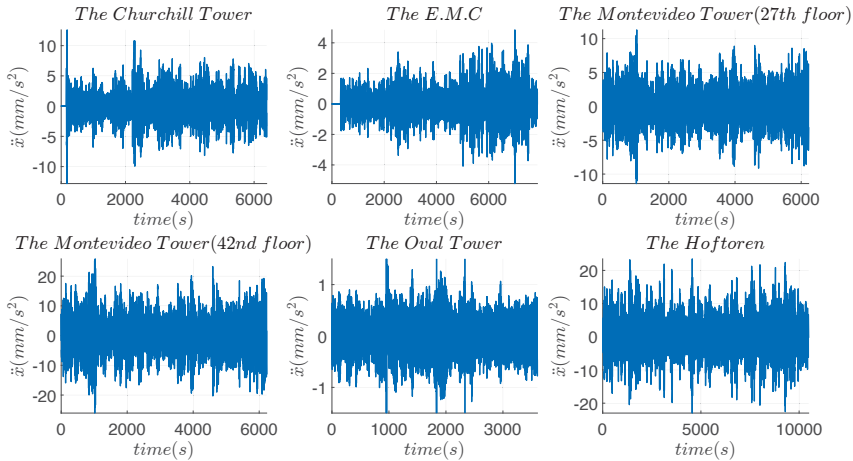
Figure 2.19: Acceleration registered in the weak X-direction of the instrumented buildings.

Figure 2.20 shows the horizontal accelerations in the Y-direction. In Fig. 2.21, the torsional accelerations of the instrumented buildings are presented. In table 2.4, a summary of the peak, RMS and effective acceleration is given for each case study.

The effective acceleration shown in Table 2.4 is the result of multiplying the peak acceleration by $\sqrt{2}/2$. Figure 2.22 shows the comfort limits established by H. van Koten. These thresholds define human perception, depending on the frequency of vibration and peak acceleration.

To determine whether the accelerations experienced by building occupants are harmful, based on the criteria drawn by H. van Koten (Fig. 2.22), the total peak acceleration is calculated by means of the following expression:
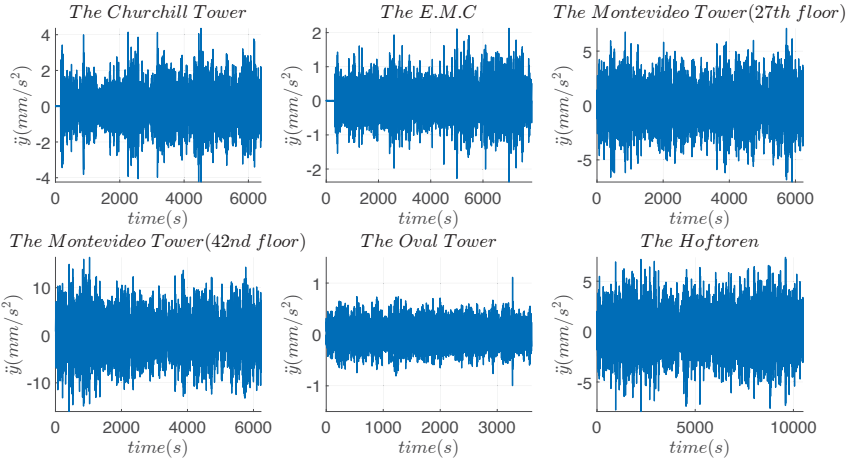
Figure 2.20: Acceleration registered in the stiff Y-direction of the instrumented buildings.
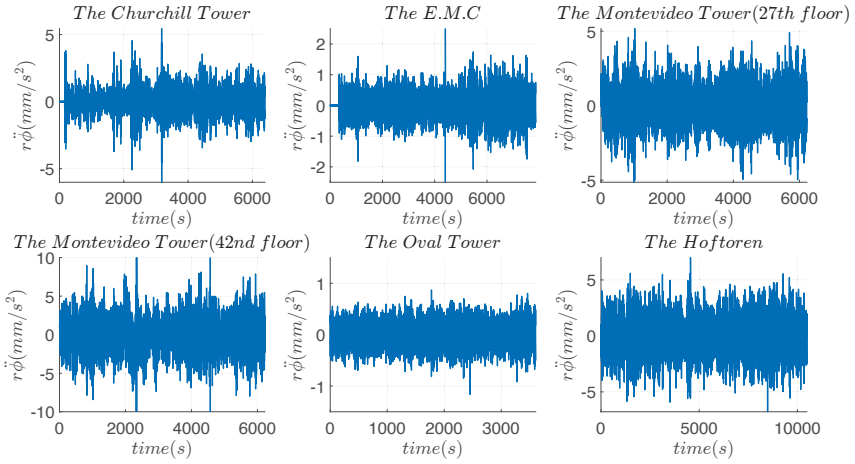
Figure 2.21: Acceleration registered in the torsional ϕ-direction of the instrumented buildings.

$$a_{\text{peak}_{\text{total}}} = \sqrt{a_{\text{peak}_{\text{bending}}}^2 + a_{\text{peak}_{\text{torsional}}}^2} \qquad (2.42)$$

The results show that, based on the H. van Koten criteria, no critical threshold for structural damage is overlooked.

Principally, at the measured accelerations, the occupants should not perceive any vibration. However, they can still complain and feel insecure in the interior of the building.

	Peak acc. [mm/s^2]	RMS acc. [mm/s^2]	Effective acc. [mm/s^2]
	12.8	1.99	9.05
The Churchill tower	4.35	0.82	3.07
	6.01	0.71	4.21
	5.22	0.76	3.69
The E.M.C	2.38	0.36	1.68
	5.42	0.26	3.83
	26.06	5.21	18.42
The Montevideo tower	16.4	3.35	11.59
	33.68	1.52	23.8
	11.28	0.31	7.31
The Oval tower	1.11	0.187	0.78
	1.16	0.182	0.82
	23.46	4.21	16.58
The Hoftoren	7.36	1.22	5.2
	6.49	0.88	4.93

Table 2.4: Peak, RMS, and effective accelerations in the weak, stiff and torsional direction of vibration of the studied buildings.
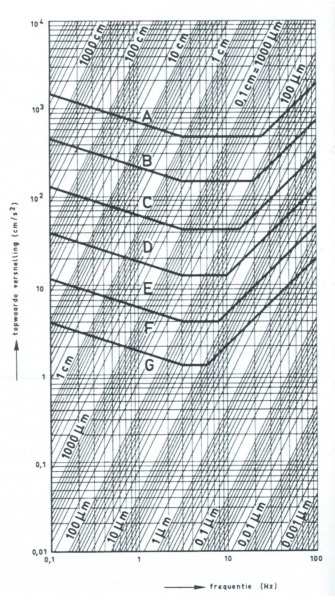
Figure 2.22: Human comfort limits based on [37].

2.7. SUMMARY

In this chapter, the equivalent viscous damping ratio associated to a buildings' natural frequencies in The Netherlands were identified by means of two identification tech-

	Description of the perceptibility	Admissibility of people in buildings	Rough judgement for the influence on the surface	Example
A	Intolerable	Inadmissible	Collapse	Emergency cases
B	Quickly tiring	Inadmissible	local damage	Sudden stopping of a motorcar
C	Heavily perceptible	Hardly admissible	Crack formation	Lift tramway
D	Good perceptible	At coarse manual labour	Beginning slight crack formation	Beginning of sickness
E	Perceptible	A short time in houses	No influence on normal buildings	
F	Hardly Perceptible	A long time in houses	No influence	
G	Not Perceptible		No influence	

Table 2.5: Criteria on the effect of accelerations in humans.

niques, showing comparable results.

The RDT enables us to identify the damping ratio with respect to the vibration amplitude at a specific mode (i.e. natural frequency). Presently, several damping predictors are available in literature. These have been used with the studied buildings to compare predicted and identified dampings. Based on observations of these results, a damping predictor, which combines two well-established damping predictors with some modifications, is proposed.

Finally, the SLS of the studied buildings in terms of occupants' well-being is studied using the criteria described in [37]. This shows that the accelerations experienced by the instrumented buildings during wind-induced vibrations do not exceed a certain threshold (i.e. level F), where no crack formation on the structure is detected. Thus, it seems reasonable to use linear elastic models for this study, which examine the influence of damping on high-rise structures subject to wind-induced vibrations.

3

BEAM MODELS FOR HIGH-RISE BUILDINGS AND THE ENERGY VARIATION LAW

The objective of this chapter is to describe equations of motion and energy variation laws for beams, which will be later used to model high-rise buildings and to identify energy dissipation. Thus, Lagrangian formalism and classical beam theory are used. First, the governing differential equations for beams in three dimensions are derived. Then, Euler–Bernoulli kinematic relations and classical constitutive equations are described. Making use of beam differential equations, the constitutive and kinematic relations, equations of motion and energy variation equations of beam elements are derived. In this work, these equations of motion and energy variation establish the groundwork for formulating the beam equations that represent the dynamic behaviour of tall buildings.

3.1. GENERAL DESCRIPTION OF BEAMS

The focus of this section is flexural deformation and coupling with axial deformations. Beam elements are widely used in the field of structural engineering to study the static and dynamic behaviour of structures. These elements help us simplify complex structural systems. A beam element can be defined as the volume generated by a plane cross-section moving along a plane curve, d, implying that any cross-section, S, is normal to d. Beams are 3-dimensional elements in which one dimension is larger than the other two. Therefore, beam elements are usually described as one-dimensional systems.

Additionally, a brief description of the Saint–Venant torsion theory [38] is given.
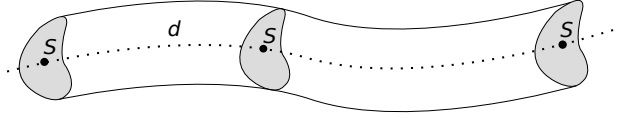
Figure 3.1: Representation of a Euler-Bernoulli beam.

3.2. DERIVATION OF THE GOVERNING DIFFERENTIAL EQUATIONS OF BEAMS IN THREE-DIMENSION

Given a straight elastic beam with an arbitrary cross-section constant along the x-axis of finite length, L, under free-loading conditions, is as shown in Fig. 3.2.
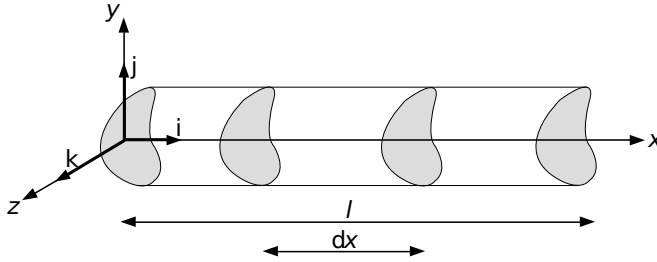
Figure 3.2: Beam element in an undeformed state.

Displacements and rotations of the beam are described by a chosen reference Cartesian coordinate system (x, y, z) with base unit vectors, **i, j, k**. The beam element can be loaded by a force-per-unit volume, $\boldsymbol{\rho b}$, and a force-per-unit surface, **t**, as shown in Fig. 3.3a, integrated over the area, as shown in (Eqs. 3.1-3.2):

$$\mathbf{q}(x,t) = \int_A \begin{pmatrix} \rho b_x \\ \rho b_y \\ \rho b_z \end{pmatrix} \mathrm{d}A + \int_{\delta A} \begin{pmatrix} t_x \\ t_y \\ t_z \end{pmatrix} \mathrm{d}(\delta A) \tag{3.1}$$

$$\mathbf{m}(x,t) = \int_A \begin{pmatrix} 0 & -z & y \\ z & 0 & 0 \\ y & 0 & 0 \end{pmatrix} \begin{pmatrix} \rho b_x \\ \rho b_y \\ \rho b_z \end{pmatrix} \mathrm{d}A + \int_{\delta A} \begin{pmatrix} 0 & -z & y \\ z & 0 & 0 \\ y & 0 & 0 \end{pmatrix} \begin{pmatrix} t_x \\ t_y \\ t_z \end{pmatrix} \mathrm{d}(\delta A) \tag{3.2}$$

These result in an equivalent force-per-unit-length vector, $\mathbf{q} = \mathbf{q}(x, t)$ and an equivalent moment-per-unit-length vector, $\mathbf{m} = \mathbf{m}(x, t)$ along the (x, y, z)-coordinates defined as

$$\mathbf{q} = \begin{bmatrix} q_x \\ q_y \\ q_z \end{bmatrix}, \quad \mathbf{m} = \begin{bmatrix} m_x \\ m_y \\ m_z \end{bmatrix} \tag{3.3}$$
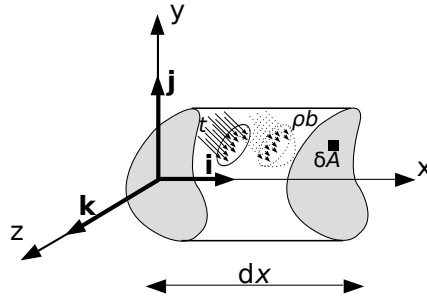
(a) Surface and body loads.
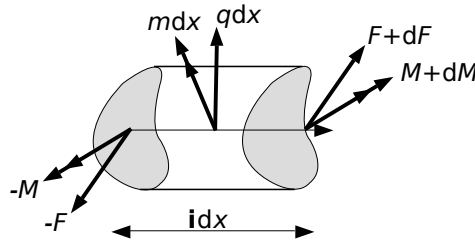
(b) Section force and moment.
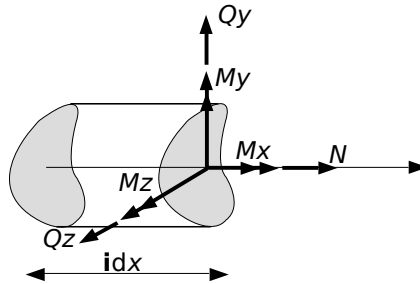
(c) Components of the load and moment vector.

Figure 3.3: Differential element of a beam in a loaded state.

External loads, $\mathbf{q}$, and moments, $\mathbf{m}$, are balanced with the internal forces and moments
represented by vectors $\mathbf{F}$ and $\mathbf{M}$, respectively. The internal force and moment vectors act
on the cross-section with the base-unit vector $\mathbf{i}$, of the x-axis in the outward direction
normal vector, as shown in Fig. 3.3b. The components of $\mathbf{F} = \mathbf{F}(x, t)$ and $\mathbf{M} = \mathbf{M}(x, t)$ in
the (x, y, z) coordinate system are

$$\mathbf{F} = \begin{bmatrix} N \\ Q_y \\ Q_z \end{bmatrix}, \qquad \mathbf{M} = \begin{bmatrix} Mx \\ M_y \\ M_z \end{bmatrix} \tag{3.4}$$

The component, $N = N(x, t)$, in the section force vector, is the axial force, $Q_y = Q_y(x, t)$ and $Q_z = Q_z(x, t)$ are the shear force components in the y- and z-directions. In the section-moment vector, $M_x = M_x(x, t)$, represents the torque, and the components $M_y = M_y(x, t)$ and $M_z = M_z(x, t)$ in the y and z directions represent the bending moments as shown in Fig. 3.3c.

At this point, it should be noted that external forces, $\mathbf{q}$, and moments, $\mathbf{m}$, also generate a deformation process described by a displacement vector, $\mathbf{w} = \mathbf{w}(x, t)$, and a rotation vector, $\boldsymbol{\theta} = \boldsymbol{\theta}(x, t)$. Therefore, the energy generated by any external load should to be balanced at any moment by the internal deformation energy and the kinetic energy of the body, as shown in Eq. 3.5.

$$\Delta E_{\text{kin}} = \mathscr{T}_{\text{int}} + \mathscr{T}_{\text{ext}} \tag{3.5}$$

The displacement vector, $\mathbf{w}$, and the rotation vector, $\boldsymbol{\theta}$, with the components in the (x, y, z) coordinate system are described in Eq. 3.6.

$$\mathbf{w} = \begin{bmatrix} w_x \\ w_y \\ w_z \end{bmatrix}, \qquad \boldsymbol{\theta} = \begin{bmatrix} \theta_x \\ \theta_y \\ \theta_z \end{bmatrix} \tag{3.6}$$

Next, using Newton's Second Law relating the internal forces and external loads to acceleration, the dynamic force and moment equilibrium equations of a differential element of a beam in three dimensions (Fig. 3.3b) can be formulated as follows.

$$-\mathbf{F} + \mathbf{F} + d\mathbf{F} + \mathbf{q}dx = \rho A dx \frac{d^2 \mathbf{w}}{dt^2}$$
$$\frac{d\mathbf{F}}{dx} + \mathbf{q} = \rho A \frac{d^2 \mathbf{w}}{dt^2} \tag{3.7}$$

$$-\mathbf{M} + \mathbf{M} + d\mathbf{M} + \mathbf{i}dx \times (\mathbf{F} + d\mathbf{F}) + \mathbf{q}\frac{dx^2}{2} + \mathbf{m}dx = \rho A \frac{dx^2}{2}\frac{d^2 \mathbf{w}}{dt^2} + \rho I dx \frac{d^2 \boldsymbol{\theta}}{dt^2}$$
$$\frac{d\mathbf{M}}{dx} + \mathbf{i} \times \mathbf{F} + \mathbf{m} = \rho I \frac{d^2 \boldsymbol{\theta}}{dt^2} \tag{3.8}$$

Equations 3.7-3.8 can be split into an equilibrium equation for each component in the (x, y, z) coordinate corresponding to Fig. 3.3c.

$$\frac{dN}{dx} + q_x = \rho A \frac{d^2 w_x}{dt^2} \qquad \frac{dQ_y}{dx} + q_y = \rho A \frac{d^2 w_y}{dt^2} \qquad \frac{dQ_z}{dx} + q_z = \rho A \frac{d^2 w_z}{dt^2} \tag{3.9}$$

$$\frac{dM_x}{dx} + m_x = \rho I \frac{d^2 \theta_x}{dt^2} \qquad \frac{dM_y}{dx} - Q_z + m_y = \rho I \frac{d^2 \theta_y}{dt^2} \qquad \frac{dM_z}{dx} + Q_y + m_z = \rho I \frac{d^2 \theta_z}{dt^2} \tag{3.10}$$

where

$$\mathbf{i} \times \mathbf{F} = \mathbf{i} \times \left(N\mathbf{i} + Q_y\mathbf{j} + Q_z\mathbf{k} \right) = 0\mathbf{i} - Q_z\mathbf{j} + Q_y\mathbf{k} \tag{3.11}$$

Therefore, the resultant vector of Eq. 3.11 has components $[0, -Qz, Qy]$. The normal force is non-zero only if the product described by Eq. 3.11 is calculated in the deformed state of the beam. This may lead to the coupled bending-torsional behaviour.

3.3. LINEAR KINEMATIC AND DISPLACEMENT RELATIONSHIPS

The kinematic relations used in this work are based on the Euler–Bernoulli assumptions. One of these assumptions implies that, in a beam, the cross-section remains straight and orthogonal to the x-axis at coordinate x during deformation. Thus, the deformation in the transverse direction (Poisson effects), owing to axial strains, are neglected. The deformed state of a cross-section of the beam is described by the displacement vector, $\mathbf{w}$, and rotation vector, $\boldsymbol{\theta}$. Assuming deformations correspond to the linear elastic range of the material, a small displacement field can be considered. Consequently, the following relation can be established:

$$\sin\boldsymbol{\theta} \approx \tan\boldsymbol{\theta} \approx \boldsymbol{\theta} \tag{3.12}$$

Next, a displacement vector of a material point on the cross-section of the beam with coordinates (x, y, z) in the undeformed state is described by the vector, $\mathbf{u} = \mathbf{u}(x, y, z, t)$, with the components in the (x, y, z) coordinate system.

$$\mathbf{u} = \begin{bmatrix} u_x \\ u_y \\ u_z \end{bmatrix} \tag{3.13}$$

The displacement vector, $\mathbf{u}$, describes the displacement of a material point, comprising the displacement, $\mathbf{w}$, and the rotation, $\boldsymbol{\theta}$, vectors. The components of the displacement vector, $\mathbf{u}$, using the Euler-Bernoulli kinematic assumptions, are described in Eq. 3.14.

$$\begin{aligned} u_x(x, y, z, t) &= w_x(x, t) + z\theta_y(x, t) - y\theta_z(x, t) \\ u_y(x, y, z, t) &= w_y(x, t) - z\theta_x(x, t) \\ u_z(x, y, z, t) &= w_z(x, t) + y\theta_x(x, t) \end{aligned} \tag{3.14}$$

Therefore, the kinematic constraint reduces the determination of any material point in a beam to the determination of the six deformation components, $w_x = w_x(x, t)$, $w_y = w_y(x, t)$, $w_z = w_z(x, t)$, $\theta_x = \theta_x(x, t)$, $\theta_y = \theta_y(x, t)$ and $\theta_z = \theta_z(x, t)$ along the x-axis of the continuous displacement field, $\mathbf{u} = \mathbf{u}(x, y, z, t)$. The kinematic equations give a relation between displacements and strains. Based on the displacement field described in Eq. 3.14 these relations are as follows:

$$\epsilon_{xx} = \frac{\partial u_x}{\partial x} = \frac{\mathrm{d}w_x}{\mathrm{d}x} + z\frac{\mathrm{d}\theta_y}{\mathrm{d}x} - y\frac{\mathrm{d}\theta_z}{\mathrm{d}x}$$

$$\gamma_{xy} = \frac{\partial u_x}{\partial y} + \frac{\partial u_y}{\partial x} = \frac{\mathrm{d}w_y}{\mathrm{d}x} - z\frac{\mathrm{d}\theta_x}{\mathrm{d}x} - \theta_z(x,t)$$

$$\gamma_{xz} = \frac{\partial u_x}{\partial z} + \frac{\partial u_z}{\partial x} = \frac{\mathrm{d}w_y}{\mathrm{d}x} + y\frac{\mathrm{d}\theta_x}{\mathrm{d}x} + \theta_y(x,t)$$

$$\epsilon_{yy} = \frac{\partial u_y}{\partial y} = 0; \quad \epsilon_{zz} = \frac{\partial u_z}{\partial z} = 0$$

$$(3.15)$$

The strain components can also be written in a matrix form as

$$\boldsymbol{\epsilon} = \begin{bmatrix} \epsilon_{xx} & \frac{1}{2}\gamma_{xy} \\ \frac{1}{2}\gamma_{yz} & \epsilon_{yy} \end{bmatrix} \tag{3.16}$$

The fact that $\epsilon_{yy} = \epsilon_{zz} = 0$ implies that the cross-section does not shrink after the deformation. This also implies that the shear deformations, γ_{xy} and γ_{xz}, are independent of the y and z directions.

The displacement field shown in Eq. 3.14 is only correct if the cross-section of the beam about the x-axis is symmetric. Otherwise, the torsional moment M_x will induce an additional displacement about the x-axis. Generally, this additional displacement can be written as $u_x(x,y,z) = \omega(y,z)\frac{d\theta_x}{dx}$, where $\omega(y,z)$ is the warping function in m^2. It should be noted that this function is dependent on y and z. Therefore, it allows for non-planar deformations. Introducing the warping effects into the displacement field (Eq. 3.14), the following expression for the displacement along the x-axis is derived.

$$u_x(x,y,z) = w_x(x) + z\theta_y(x) - y\theta_z(x) + \omega(y,z)\frac{d\theta_x}{dx} \tag{3.17}$$

Introducing the warping term into the kinematic equations, the strain components in Eq. 3.15 are modified as follows:

$$\epsilon_{xx} = \frac{\partial u_x}{\partial x} = \frac{\mathrm{d}w_x}{\mathrm{d}x} + z\frac{\mathrm{d}\theta_y}{\mathrm{d}x} - y\frac{\mathrm{d}\theta_z}{\mathrm{d}x} + \omega(y,z)\frac{d^2\theta_x}{dx^2}$$

$$\gamma_{xy} = \frac{\partial u_x}{\partial y} + \frac{\partial u_y}{\partial x} = \frac{\mathrm{d}w_y}{\mathrm{d}x} + \left(\frac{\partial\omega}{\partial y} - z\right)\frac{\mathrm{d}\theta_x}{\mathrm{d}x} - \theta_z(x)$$

$$\gamma_{xz} = \frac{\partial u_x}{\partial z} + \frac{\partial u_z}{\partial x} = \frac{\mathrm{d}w_y}{\mathrm{d}x} + \left(\frac{\partial\omega}{\partial z} + y\right)\frac{\mathrm{d}\theta_x}{\mathrm{d}x} + \theta_y(x)$$

$$\epsilon_{yy} = \frac{\partial u_y}{\partial y} = 0; \quad \epsilon_{zz} = \frac{\partial u_z}{\partial z} = 0$$

$$(3.18)$$

Euler-Bernoulli kinematics assumes that $\epsilon_{yy} = \epsilon_{zz} = 0$ and the shear strains, γ_{xy} and γ_{xz}, are negligible compared to the axial strain, ϵ_{xx}. Therefore, it can be established that

$$\epsilon_{yy} = \epsilon_{zz} = \gamma_{xy} = \gamma_{xz} = 0. \tag{3.19}$$

Moreover, Euler-Bernoulli theory assumes that the rotated cross-section is always orthogonal to the deformed beam axis. Consequently, the following additional kinematic constraints on the deformation of the cross-section can be established.

$$
\theta_y = -\frac{\mathrm{d}w_z}{\mathrm{d}x}
$$
$$
\theta_z = \frac{\mathrm{d}w_y}{\mathrm{d}x}
$$
(3.20)

The fact that Bernoulli-Euler assumes $\gamma_{xy} = \gamma_{xz} = 0$ immediately implies that the shear forces become $Q_y = Q_z = 0$. However, contradictory shear forces are indeed present in the bending of the beams. Therefore, it should be noted that shear forces in Euler–Bernoulli equations cannot be derived from the kinematic equations, but are derived from the force-equilibrium equation of the beam.

Furthermore, we look at the deformed shape of a differential element of a beam with the assumption of small displacements (see Fig. 3.4).
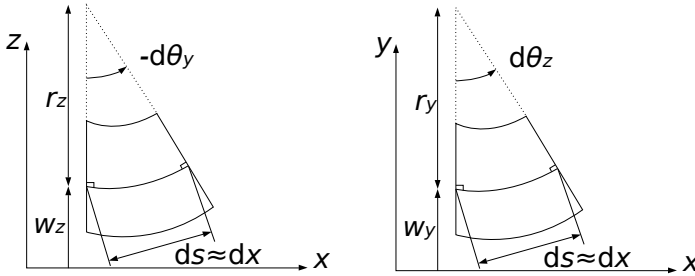
Figure 3.4: Definition of the curvature of a Euler-Bernoulli beam in its deformed state.

Thus, the radii of curvatures, r_y and r_z, are related to the rotations, $\mathrm{d}\theta_z$ and $-\mathrm{d}\theta_y$, as

$$
r_y \mathrm{d}\theta_z = \mathrm{d}x \qquad\qquad \kappa_y = \frac{-1}{r_z} = \frac{\mathrm{d}\theta_y}{\mathrm{d}x}
$$
$$
-r_z \mathrm{d}\theta_y = \mathrm{d}x \qquad\qquad \kappa_z = \frac{1}{r_y} = \frac{\mathrm{d}\theta_z}{\mathrm{d}x}
$$
(3.21)

where κ_y and κ_z are the components of the curvature vector, $\boldsymbol{\kappa}(x,t)=\boldsymbol{\kappa}$. Thus, using Euler-Bernoulli beam theory, the curvature components become

$$
\kappa_y = -\frac{\mathrm{d}^2 w_z}{\mathrm{d}x^2}
$$
$$
\kappa_z = \frac{\mathrm{d}^2 w_y}{\mathrm{d}x^2}.
$$
(3.22)

Introducing Eq. 3.22 into Eq. 3.18, it follows that the axial strain can be written as

$$\epsilon_{xx}(x, y, z, t) = \epsilon(x, t) + z\kappa_y - y\kappa_z + \omega(y, z, t)\frac{d^2\theta_x}{dx^2} \tag{3.23}$$

where $\epsilon(x, t) = \frac{dw_x}{dx}$ is the axial strain of the beam along the x-axis.

3.4. SAINT-VENANT TORSION THEORY

A widely-used torsion theory is the one described by Saint–Venant, where the underlying assumption is that $\phi = \frac{d\theta_x}{dx}$ is constant. This implies that, in the case of circular beam geometries, given the symmetry in the cross-section and the loads, the planar cross-sections perpendicular to the axis remain planar and do not deform in the plane. Thus, the displacement functions can be described as

$$\begin{aligned} u_x(x, y, z, t) &= \frac{d\theta_x}{dx}\omega(y, z) \\ u_y(x, y, z, t) &= -z\theta_x \\ u_z(x, y, z, t) &= y\theta_x \end{aligned} \tag{3.24}$$

Consequently, the kinematic equations described by Saint-Venant are

$$\begin{aligned} \epsilon_{xx} &= \epsilon_{yy} = \epsilon_{zz} = \epsilon_{yz} = 0 \\ \gamma_{xy} &= \frac{\partial u_x}{\partial y} + \frac{\partial u_y}{\partial x} = \left(\frac{\partial\omega}{\partial y} - z\right)\frac{d\theta_x}{dx} \\ \gamma_{xz} &= \frac{\partial u_x}{\partial z} + \frac{\partial u_z}{\partial x} = \left(\frac{\partial\omega}{\partial z} + y\right)\frac{d\theta_x}{dx}. \end{aligned} \tag{3.25}$$

Therefore, all components of the Cauchy stress tensor become equal to zero. However, the shear stresses σ_{xy} and σ_{xz}. In the case of an elastic material, these are defined as

$$\begin{aligned} \sigma_{xy} &= 2G\epsilon_{xy} = G\left(\frac{\partial\omega}{\partial y} - z\right)\frac{d\theta_x}{dx} \\ \sigma_{xz} &= 2G\epsilon_{xz} = G\left(\frac{\partial\omega}{\partial z} + y\right)\frac{d\theta_x}{dx} \end{aligned} \tag{3.26}$$

where G is the transverse elastic modulus. The Saint-Venant torsional problem is described by the following differential equation with Neumann boundary conditions:

$$\begin{aligned} \nabla^2\omega &= 0 \\ \frac{\partial\omega}{\partial n} &= zn_y - yn_z \quad \text{in} \quad \Gamma \end{aligned} \tag{3.27}$$

The torsion problem depends on the geometry and, generally, is difficult to solve. In the presence of warping effects, the axial strain is non-zero. $\frac{d\theta_x}{dx}$ is no longer constant along

the x-coordinate. This phenomenon was described for thin-walled beams for the first time by Vlasov (1961) [39]. Consequently, the non-homogeneous torsion is referred to as the Vlaslov torsion.

3.5. CONSTITUTIVE RELATIONS FOR AN ELASTIC BEAM

The constitutive equations relate strains with stresses. For a linear elastic material, the following relations can be derived:

$$
\begin{aligned}
\sigma_{xx} &= E\epsilon_{xx} = E\left(\frac{\mathrm{d}w_x}{\mathrm{d}x} + z\frac{\mathrm{d}\theta_y}{\mathrm{d}x} - y\frac{\mathrm{d}\theta_z}{\mathrm{d}x} + \omega(y,z)\frac{d^2\theta_x}{\mathrm{d}x^2}\right) \\
\sigma_{xy} &= G\gamma_{xy} = G\left(\frac{\mathrm{d}w_y}{\mathrm{d}x} + \left(\frac{\partial\omega}{\partial y} - z\right)\frac{\mathrm{d}\theta_x}{\mathrm{d}x} - \theta_z(x)\right) \\
\sigma_{xz} &= G\gamma_{xz} = G\left(\frac{\partial u_x}{\partial z} + \frac{\partial u_z}{\partial x} = \frac{\mathrm{d}w_y}{\mathrm{d}x} + \left(\frac{\partial\omega}{\partial z} + y\right)\frac{\mathrm{d}\theta_x}{\mathrm{d}x} + \theta_y(x)\right) \\
\sigma_{yy} &= E\epsilon_{yy} = 0
\end{aligned}
\tag{3.28}
$$

here, E and G are the elastic and the transverse elastic moduli, respectively. They are directly related to material behaviour. The normal stress, σ_{xx}, is directed normal to the cross-section of the beam, and the shear stresses, σ_{xy} and σ_{xz}, are acting in the plane of the cross-section of the beam, as shown in Fig. 3.5.
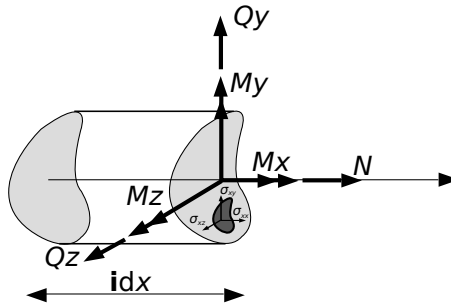
Figure 3.5: Stress state of differential element of a beam cross-section.

Normal and the shear stresses are related to the components of the force vector and the moment vector, as follows:

$$
\begin{aligned}
N &= \int_A \sigma_{xx}\mathrm{d}A & Q_y &= \int_A \sigma_{xy}\mathrm{d}A & Q_z &= \int_A \sigma_{xz}\mathrm{d}A \\
M_x &= \int_A \left(y\sigma_{xz} - z\sigma_{xy}\right)\mathrm{d}A & M_y &= \int_A z\sigma_{xx}\mathrm{d}A & M_z &= -\int_A y\sigma_{xx}\mathrm{d}A.
\end{aligned}
\tag{3.29}
$$

It should be noted that, assuming uni-axial strain does not imply uniaxial stress-state, the stress-state of an elastic body can be represented as shown in Fig. 3.6.
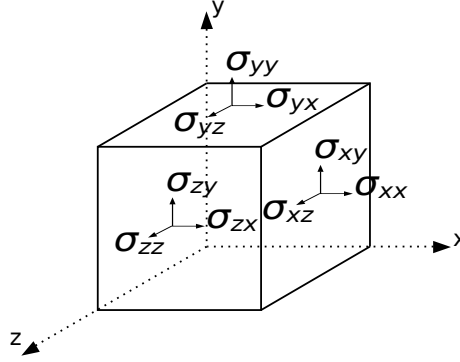
Figure 3.6: 3D elastic body.

The first index indicates the coordinate axis co-directional to the outward normal vector of the section, whereas the second index specifies the direction of action of the stress component. The stresses represented in Fig. 3.6 form the components of the stress tensor, $\boldsymbol{\sigma}$, in the (x, y, z) coordinate system and can be represented in its matrix form:

$$\boldsymbol{\sigma} = \begin{bmatrix} \sigma_{xx} & \sigma_{yx} & \sigma_{zx} \\ \sigma_{xy} & \sigma_{yy} & \sigma_{zy} \\ \sigma_{xz} & \sigma_{yz} & \sigma_{zz} \end{bmatrix} \tag{3.30}$$

Next, introducing Eq. 3.28 into Eq. 3.29, and integrating the cross-section of the prismatic beam gives the following expressions:

$$
\begin{aligned}
N &= E\left(A\frac{\mathrm{d}w_x}{\mathrm{d}x} + S_y\frac{\mathrm{d}\theta_y}{\mathrm{d}x} - S_z\frac{\mathrm{d}\theta_z}{\mathrm{d}x} + S_\omega\frac{d^2\theta_x}{\mathrm{d}x^2}\right) \\
Q_y &= G\left(A_y\left(\frac{\mathrm{d}w_y}{\mathrm{d}x} - \theta_z\right) + R_y\frac{\mathrm{d}\theta_x}{\mathrm{d}x}\right) \\
Q_z &= G\left(A_z\left(\frac{\mathrm{d}w_z}{\mathrm{d}x} + \theta_y\right) + R_z\frac{\mathrm{d}\theta_x}{\mathrm{d}x}\right) \\
M_x &= G\left(S_z\left(\frac{\mathrm{d}w_z}{\mathrm{d}x} + \theta_y\right) - S_y\left(\frac{\mathrm{d}w_y}{\mathrm{d}x} - \theta_z\right) + K\frac{\mathrm{d}\theta_x}{\mathrm{d}x}\right) \\
M_y &= E\left(S_y\frac{\mathrm{d}w_x}{\mathrm{d}x} + I_{yy}\frac{\mathrm{d}\theta_y}{\mathrm{d}x} - I_{yz}\frac{\mathrm{d}\theta_z}{\mathrm{d}x} + I_{\omega z}\frac{\mathrm{d}\theta_x}{\mathrm{d}x}\right) \\
M_z &= E\left(-S_z\frac{\mathrm{d}w_x}{\mathrm{d}x} + I_{zz}\frac{\mathrm{d}\theta_z}{\mathrm{d}x} - I_{yz}\frac{\mathrm{d}\theta_y}{\mathrm{d}x} - I_{\omega y}\frac{\mathrm{d}\theta_x}{\mathrm{d}x}\right).
\end{aligned}
\tag{3.31}
$$

The integrals of the cross-sectional constants are described in Appendix C.

3.6. DETERMINATION OF THE PRINCIPAL AXES OF A BEAM ELEMENT

While formulating the differential equations governing a beam element, the coordinate system is chosen arbitrarily. Thus, the deformations (i.e. axial and bending) for each direction, might be coupled. If an axial force is applied to the beam, axial deformation can occur, but deformations and rotations can also occur in the other directions. Consequently, if we substitute Eq. 3.31 into Eqs. 3.9-3.10, the result is a set of coupled differential equations. The coupling might have a significant impact on the structural behaviour or the stability of a beam element. For instance, if we take a Euler–Bernoulli bending beam, the maximum stress, σ_{xx}, for arbitrary axis can be defined as

$$\sigma_{xx} = \frac{N}{A} - \frac{M_z I_y + M_y I_{yz}}{I_y I_z + I_{xy}^2} y + \frac{M_y I_z + M_z I_{yz}}{I_y I_z + I_{xy}^2} z \tag{3.32}$$

In the case of the principal axis of inertia ($I_{yz} = 0$), the maximum stress, σ_{xx}, is defined as shown in Eq. 3.33.

$$\sigma_{xx} = \frac{N}{A} - \frac{M_z}{I_z} y + \frac{M_y}{I_y} z \tag{3.33}$$

For the principal bending axis, bending in each direction and axial deformation can be decoupled, so that

$$\sigma_{xx} = \frac{N}{A}; \qquad\qquad \sigma_{xx} = -\frac{M_z}{I_z} y; \qquad\qquad \sigma_{xx} = \frac{M_y}{I_y} z. \tag{3.34}$$

Choosing a specific reference system may change the method of computing the structural stresses. It is of importance then to identify the bending axis and the principal axis of a beam element to decouple the deformations in each direction if needed.

3.6.1. DETERMINING THE BENDING CENTRE AND PRINCIPAL DIRECTIONS
The bending centre of a beam element can be determined by means of a position vector, $\vec{r}_b(x, y, z)$, with the components, $[0, y_b, z_b]$, as

$$\mathbf{x}(x, y, z) = \overline{\mathbf{X}}(x', y', z') + \vec{r}_b(x, y, z) \tag{3.35}$$

where $\overline{\mathbf{X}}$ is a vector containing the components of a new reference system (x', y', z') in the yet unknown bending centre of the beam as shown in Fig. 3.7.
In the new coordinate system, the displacement along the x-axis can be written as

$$u_x'(x', y', z') = w_x' + z_b \theta_y' - y_b \theta_z'. \tag{3.36}$$

The axial strain of the new axis becomes

$$\epsilon_{xx}(x') = \frac{\partial u_x'}{\partial x'} = \epsilon' + z_b \kappa_y' - y_b \kappa_z'. \tag{3.37}$$

It should be noted that the components of the rotation, $\boldsymbol{\theta}'$, and the displacement, $\mathbf{w}'$, vectors in the new coordinate system are identical to the components of the rotation,
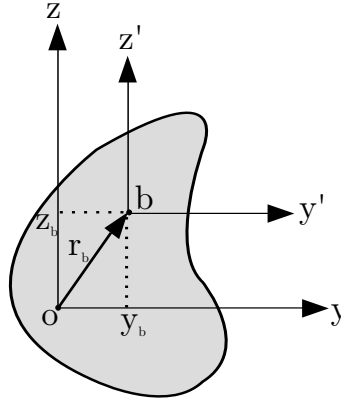
Figure 3.7: Determining the bending centre in a beam with an arbitrary cross-section.

$\boldsymbol{\theta}$, and the displacement, $\mathbf{w}$, vectors in reference coordinate system. This means that the section force, $\mathbf{F} = \mathbf{F}'$, in the new coordinate system and in the reference coordinate system, are equal to the section moment $\mathbf{M} = \mathbf{M}'$. Thus, the following relations can be established for the force vector components:

$$N' = N; \qquad Q'_y = Q_y; \qquad Q'_z = Q_z \tag{3.38}$$

and for the moment-vector components:

$$M'_x = M_x; \qquad M'_y = M_y - z_b N; \qquad M'_z = M_z + y_b N \tag{3.39}$$

Consequently, the following strain relation can be written as

$$\epsilon = \epsilon' - z_b \kappa_z + y_b \kappa_z = \epsilon' - z_b \kappa'_y + y_b \kappa'_z. \tag{3.40}$$

The relation between forces and moments with displacements and rotations of the new coordinate system with the reference axis can be condensed using matrix notation:

$$\boldsymbol{\sigma}' = \mathbf{A}^T \boldsymbol{\sigma}$$
$$\boldsymbol{\epsilon} = \mathbf{A}\boldsymbol{\epsilon}', \tag{3.41}$$

where

$$\boldsymbol{\sigma} = \begin{bmatrix} N \\ M_y \\ M_z \end{bmatrix}; \quad \boldsymbol{\sigma}' = \begin{bmatrix} N' \\ M'_y \\ M'_z \end{bmatrix}; \qquad \boldsymbol{\epsilon} = \begin{bmatrix} \epsilon \\ \kappa_y \\ \kappa_z \end{bmatrix}; \quad \boldsymbol{\epsilon} = \begin{bmatrix} \epsilon' \\ \kappa'_y \\ \kappa'_z \end{bmatrix} \tag{3.42}$$

and

$$\mathbf{A} = \begin{bmatrix} 1 & -z_b & y_b \\ 0 & 1 & 0 \\ 0 & 0 & 1 \end{bmatrix}. \tag{3.43}$$

The constitutive relation between $\boldsymbol{\sigma}$ and $\boldsymbol{\epsilon}$ can be written as

$$\boldsymbol{\sigma} = \mathbf{C}\boldsymbol{\epsilon} \tag{3.44}$$

where

$$\mathbf{C} = E \begin{bmatrix} A & S_y & -S_z \\ S_y & I_{yy} & -I_{yz} \\ -S_z & -I_{yz} & I_{zz} \end{bmatrix}. \tag{3.45}$$

Likewise, the constitutive relation in the (x', y', z') coordinate system reads,

$$\boldsymbol{\sigma}' = \mathbf{C}'\boldsymbol{\epsilon}', \tag{3.46}$$

where matrix $\mathbf{C}'$ has the following form:

$$\mathbf{C}' = E \begin{bmatrix} A & S_y' & -S_z' \\ S_y' & I_{yy}' & -I_{yz}' \\ -S_z & -I_{yz}' & I_{zz}' \end{bmatrix}. \tag{3.47}$$

Combining Eq. 3.41 with Eq. 3.44, it follows that

$$\boldsymbol{\sigma}' = \mathbf{A}^T\mathbf{C}\boldsymbol{\epsilon} = \mathbf{A}^T\mathbf{C}\mathbf{A}\boldsymbol{\epsilon} \tag{3.48}$$

where

$$\mathbf{C}' = \mathbf{A}^T\mathbf{C}\mathbf{A} = E \begin{bmatrix} 1 & 0 & 0 \\ -z_O & 1 & 0 \\ y_O & 0 & 1 \end{bmatrix} \begin{bmatrix} A & S_y & -S_z \\ S_y & I_{yy} & -I_{yz} \\ -S_z & -I_{yz} & I_{zz} \end{bmatrix} \begin{bmatrix} 1 & -z_b & y_b \\ 0 & 1 & 0 \\ 0 & 0 & 1 \end{bmatrix} \tag{3.49}$$

and finally,

$$\mathbf{C}' = \begin{bmatrix} A & S_y - z_b A & -(S_z - y_b A) \\ S_y - z_b A & I_{yy} - 2z_b S_y + z_b^2 A & -I_{yz} + y_b S_y + z_b(S_z - y_b A) \\ -(S_z - y_b A) & -I_{yz} + y_b S_y + z_b(S_z - y_b A) & I_{zz} - 2y_b S_z + y_b^2 A \end{bmatrix} \tag{3.50}$$

where the bending centres are defined as

$$y_b = \frac{S_z}{A} \qquad z_b = \frac{S_y}{A}. \tag{3.51}$$

y_b and z_b are components of vector $\vec{\mathbf{r}}_b$. The bending moments of inertia, I_{yy}', I_{zz}', and the centrifugal moment of inertia, I_{yz}', in the new coordinate system can be expressed in terms of the corresponding quantities in the reference coordinate system as follows:

$$
\begin{aligned}
I'_{yy} &= I_{yy} - 2z_b S_y + z_b^2 A = I_{yy} - z_b^2 A \\
I'_{zz} &= I_{zz} - 2y_b S_z + y_b^2 A = I_{zz} - y_b^2 A \\
I'_{yz} &= I_{yz} - y_b S_y - z_b S_z + y_b Z_b A = I_{yz} - z_b y_b A.
\end{aligned}
\tag{3.52}
$$

If the cross-section of the beam element is symmetric around one axis, and the y-axis is placed such that it coincides with this line of symmetry, then the static moment of inertia, S_y, vanishes, such that

$$
S_y = \int_A z \, \mathrm{d}A = 0.
\tag{3.53}
$$

Thus, the bending centre, b, will always be located on the line of symmetry in a single-symmetric cross-section. If the cross-section is doubly symmetric, then the position of b is found at the intersection of the two lines of symmetry.

Next, the origin of the (x, y, z) coordinate system is placed at the bending centre. Then, the constitutive matrix takes the form

$$
\mathbf{C} = \begin{bmatrix} A & 0 & 0 \\ 0 & I_{yy} & -I_{yz} \\ 0 & -I_{yz} & I_{zz} \end{bmatrix}.
\tag{3.54}
$$

Therefore, axial force N no longer induces deformations in the y- and z- directions, and the bending moments, M_y and M_z, do not induce axial displacements. However, the bending moment, M_y, still induces displacements in the y direction in addition to the expected displacements in the z direction. Similarly, the bending moment, M_z, induces displacements in both the y and z directions. To find the principal directions, the new (x', y', z') coordinate system can be rotated about the origin, b, as follows:

$$
\boldsymbol{\sigma} = \mathbf{B} \boldsymbol{\sigma}'
\tag{3.55}
$$

where $\mathbf{B}$ is a rotation matrix defined as

$$
\mathbf{B} = \begin{bmatrix} 1 & 0 & 0 \\ 0 & \cos(\phi) & -\sin(\phi) \\ 0 & \sin(\phi) & \cos(\phi) \end{bmatrix}.
\tag{3.56}
$$

Likewise, the strain vector in the principal direction is related to the strain vector of the rotation matrix as

$$
\boldsymbol{\epsilon} = \mathbf{B} \boldsymbol{\epsilon}'.
\tag{3.57}
$$

This allows us to use the following constitutive relation:

$$
\boldsymbol{\sigma}' = \mathbf{C}' \boldsymbol{\epsilon}' = \mathbf{B}^T \mathbf{C} \mathbf{B} \boldsymbol{\epsilon}'
\tag{3.58}
$$

so that

$$\mathbf{C}' = \mathbf{B}^T \mathbf{C} \mathbf{B} = E \begin{bmatrix} 1 & 0 & 0 \\ 0 & \cos(\phi) & \sin(\phi) \\ 0 & -\sin(\phi) & \cos(\phi) \end{bmatrix} \begin{bmatrix} A & 0 & 0 \\ 0 & I'_{yy} & -I'_{yz} \\ 0 & -I'_{yz} & I'_{zz} \end{bmatrix} \begin{bmatrix} 1 & 0 & 0 \\ 0 & \cos(\phi) & -\sin(\phi) \\ 0 & \sin(\phi) & \cos(\phi) \end{bmatrix}$$

(3.59)

Finally, the inertia in the principal directions can be found as shown in Eq. 3.60.

$$I'_{yy} = \frac{1}{2}(I_{yy} + I_{zz}) + \frac{1}{2}(I_{yy} - I_{zz})\cos(2\phi) - I_{yz}\sin(2\phi)$$

$$I'_{zz} = \frac{1}{2}(I_{yy} + I_{zz}) + \frac{1}{2}(I_{yy} - I_{zz})\cos(2\phi) + I_{yz}\sin(2\phi)$$

(3.60)

$$I'_{yz} = -\frac{1}{2}\sin(2\phi)(I_{yy} - I_{zz}) - \cos(2\phi) - I_{yz}$$

3.7. EQUATIONS OF MOTION FOR ELASTIC BEAMS

Beam elements are generally useful for solving structural problems. To solve a dynamic problem, a coordinate system should first be defined, and the DoF should be identified. Then, the governing equation of a boundary-value problem can be formulated, and with a set of initial conditions the problem can finally be solved. In relatively simple problems with reduced amounts of DoFs, the Newton's Second Law can be very convenient for formulating equations of motion. However, for more complex systems (e.g. coupled systems with several DoF's), this is sometimes difficult. Thus, formulating equations of motions by means of the Lagrange formalism is much more convenient. The Lagrange equations are deduced from the Hamilton principle:

$$\delta \int_{t_1}^{t_2} (\mathscr{L} + \mathscr{V}_{\text{ext}}) \, \mathrm{d}t = 0$$

(3.61)

where $\mathscr{L} = \mathscr{T} - \mathscr{V}_{\text{int}}$ is the Lagrangian. The kinetic energy, $\mathscr{T}$, and the potential elastic energy, $\mathscr{V}_{\text{int}}$, of a one-dimensional beam can be defined as

$$\mathscr{T} = \int_0^l T(x, t)\mathrm{d}x$$

$$\mathscr{V}_{\text{int}} = \int_0^l V_{\text{int}}(x, t)\mathrm{d}x.$$

(3.62)

The external energy, $\mathscr{V}_{\text{ext}}$, shown in Eq. 3.61, describes the energy generated by distributed loads and moments on Beam [1], and can be defined as

$$\mathscr{V}_{\text{ext}} = -\int_0^l V_{\text{ext}}(x, t)\mathrm{d}x$$

(3.63)

Next, let us consider **u** as the displacement field. The potential energy density is a function of the displacement **u**, and its first **u**$'$ and second derivative **u**$''$ with respect to the space variable.

---

[1]Concentrated loads and moments can be considered making use of the Dirac delta function.

$$\mathbf{V}_{\text{int}} = V_{\text{int}}\left(x, t, \mathbf{u}, \mathbf{u}', \mathbf{u}''\right) \tag{3.64}$$

The kinetic energy density is a function of velocity, $\dot{\mathbf{u}}$, the rotational velocity $\dot{\mathbf{u}}'$ and the displacement $\mathbf{u}$.

$$\mathbf{T} = T\left(x, t, \mathbf{u}, \dot{\mathbf{u}}, \dot{\mathbf{u}}'\right) \tag{3.65}$$

The external energy density introduced by external loads can be described as a function of the displacement, $\mathbf{u}$, and its first spatial derivative, $\mathbf{u}'$.

$$\mathbf{V}_{\text{ext}} = V_{\text{ext}}\left(x, t, \mathbf{u}, \mathbf{u}'\right) \tag{3.66}$$

Therefore, the Lagrangian density function can be expressed as

$$\lambda = T\left(x, t, \mathbf{u}, \dot{\mathbf{u}}, \dot{\mathbf{u}}'\right) - V_{\text{int}}\left(x, t, \mathbf{u}, \mathbf{u}', \mathbf{u}''\right) = \lambda\left(x, t, \mathbf{u}, \dot{\mathbf{u}}, \mathbf{u}', \dot{\mathbf{u}}', \mathbf{u}''\right). \tag{3.67}$$

Next, a general equation of motion can be derived from the variational expression, Eq. 3.61, of the Lagrangian density function λ, and the external energy density function, $\mathbf{V}_{\text{ext}}$ as

$$\delta \int_{t_1}^{t_2} \int_0^l (\lambda + \mathbf{V}_{\text{ext}}) \, \mathrm{d}x \mathrm{d}t = \int_{t_1}^{t_2} \left(\int_0^l \left(\frac{\partial \lambda}{\partial \mathbf{u}} \delta\mathbf{u} + \frac{\partial \lambda}{\partial \mathbf{u}'} \delta\mathbf{u}' + \frac{\partial \lambda}{\partial \mathbf{u}''} \delta\mathbf{u}'' + \frac{\partial \lambda}{\partial \dot{\mathbf{u}}'} \delta\dot{\mathbf{u}}' + \frac{\partial \lambda}{\partial \dot{\mathbf{u}}} \delta\dot{\mathbf{u}} \right) \mathrm{d}x \right.$$
$$\left. + \left(\int_0^l \delta(x) \mathbf{Q} \delta\mathbf{u} \mathrm{d}x + \int_0^l \delta'(x) \mathbf{M} \delta\mathbf{u}' \mathrm{d}x + \int_0^l \mathbf{q} \delta\mathbf{u} \mathrm{d}x + \int_0^l \mathbf{m} \delta\mathbf{u}' \mathrm{d}x \right) \right) \mathrm{d}t = 0 \tag{3.68}$$

where $\mathbf{Q}$ and $\mathbf{M}$ describe concentrated forces and moments respectively. Equation 3.68 can be evaluated via integration by parts, in order to express all the variations in terms of the virtual displacement, $\delta\mathbf{u}$, as follows:

$$\int_0^l \frac{\partial \lambda}{\partial \mathbf{u}'} \delta\mathbf{u}' \mathrm{d}x = \frac{\partial \lambda}{\partial \mathbf{u}'} \delta\mathbf{u} |_0^l - \int_0^l \frac{\partial}{\partial x} \frac{\partial \lambda}{\partial \mathbf{u}'} \delta\mathbf{u} \mathrm{d}x$$

$$\int_0^l \frac{\partial \lambda}{\partial \mathbf{u}''} \delta\mathbf{u}'' \mathrm{d}x = \left(\frac{\partial \lambda}{\partial \mathbf{u}''} \delta\mathbf{u}' - \frac{\partial}{\partial x} \frac{\partial \lambda}{\partial \mathbf{u}''} \delta\mathbf{u} \right) |_0^l + \int_0^l \frac{\partial^2}{\partial x^2} \frac{\partial \lambda}{\partial \mathbf{u}''} \delta\mathbf{u} \mathrm{d}x$$

$$\int_{t_1}^{t_2} \frac{\partial \lambda}{\partial \dot{\mathbf{u}}} \delta\dot{\mathbf{u}} \mathrm{d}t = \frac{\partial \lambda}{\partial \dot{\mathbf{u}}} \delta\mathbf{u} |_{t_1}^{t_2} - \int_{t_1}^{t_2} \frac{\partial}{\partial t} \frac{\partial \lambda}{\partial \dot{\mathbf{u}}} \delta\mathbf{u} \mathrm{d}x \tag{3.69}$$

$$\int_{t_1}^{t_2} \int_0^l \frac{\partial \lambda'}{\partial \ddot{\mathbf{u}}} \delta\dot{\mathbf{u}}' \mathrm{d}x \mathrm{d}t = \frac{\partial \lambda}{\partial \dot{\mathbf{u}}'} \delta\mathbf{u}' \mathrm{d}x |_{t_1}^{t_2} - \int_{t_1}^{t_2} \int_0^l \frac{\partial}{\partial t} \frac{\partial \lambda}{\partial \dot{\mathbf{u}}'} \delta\mathbf{u}' \mathrm{d}x \mathrm{d}t$$

$$\int_0^l \mathbf{m} \delta\mathbf{u}' \mathrm{d}x = \mathbf{m} \delta\mathbf{u} |_0^l - \int_0^l \frac{\partial \mathbf{m}}{\partial x} \delta\mathbf{u} \mathrm{d}x$$

Gathering all terms, introducing a dissipative function, $\mathscr{D}(\dot{\mathbf{u}})$, and applying the Hamilton principle described by Eq. 3.61, the following generalized equation of motion for one-dimensional continuous systems can be obtained:

$$\frac{\partial \lambda}{\partial \mathbf{u}} - \frac{\partial}{\partial x}\frac{\partial \lambda}{\partial \mathbf{u}'} + \frac{\partial^2}{\partial x^2}\frac{\partial \lambda}{\partial \mathbf{u}''} - \frac{\partial}{\partial t}\frac{\partial \lambda}{\partial \dot{\mathbf{u}}} + \frac{\partial}{\partial t}\left(\frac{\partial}{\partial x}\left(\frac{\partial \lambda}{\partial \dot{\mathbf{u}}'}\right)\right) + \frac{\partial \mathscr{D}}{\partial \dot{\mathbf{u}}} + \mathbf{q} - \frac{\partial \mathbf{m}}{\partial x} = 0 \tag{3.70}$$

with the natural boundary conditions,

$$\mathbf{m} + \frac{\partial \lambda}{\partial \mathbf{u}'} - \frac{\partial}{\partial x}\frac{\partial \lambda}{\partial \mathbf{u}''} - \frac{\partial}{\partial t}\frac{\partial \lambda}{\partial \dot{\mathbf{u}}'} = \overline{T} \qquad \text{at} \qquad x = 0, L \tag{3.71}$$

and

$$\frac{\partial \lambda}{\partial \mathbf{u}''} = \overline{M} \qquad \text{at} \qquad x = 0, L \tag{3.72}$$

Equations 3.70-3.72, supplemented by appropriate kinematic boundary conditions, govern the dynamics of a wide class of one-dimensional systems.

3.8. ENERGY VARIATION LAW

The Lagrangian formalism can also be used to formulate the energy balance equation, as follows:

$$\frac{\mathrm{d}\mathscr{H}(t)}{\mathrm{d}t} + S(x,t)|_0^l + W_{\text{diss}}(t) = W_{\text{ext}}(t) \tag{3.73}$$

In Eq. 3.73, $\mathscr{H}$ is the Hamiltonian, and it is defined as

$$\mathscr{H}(t) = \int_0^l e(x,t)\mathrm{d}x \tag{3.74}$$

where e is the Hamiltonian density, defined as

$$e = \left(\frac{\partial \mathbf{u}}{\partial t}, \frac{\partial \lambda}{\partial t}\right) + \left(\frac{\partial^2 \mathbf{u}}{\partial x \partial t}, \frac{\partial^2 \lambda}{\partial x \partial t}\right) - \lambda. \tag{3.75}$$

The energy flux, $\mathbf{S}$, shown in Eq. 3.73, is defined as

$$\mathbf{S} = \left(\frac{\partial \mathbf{u}}{\partial t}, \frac{\partial \lambda}{\partial \mathbf{u}'} - \frac{\partial}{\partial x}\frac{\partial \lambda}{\partial \mathbf{u}''} - \frac{\partial}{\partial t}\frac{\partial \lambda}{\partial \mathbf{u}'\partial \dot{\mathbf{u}}}\right) + \left(\frac{\partial^2 \mathbf{u}}{\partial x \partial t}, \frac{\partial \lambda}{\partial \mathbf{u}''}\right). \tag{3.76}$$

The energy dissipation, W_{diss}, is a velocity dependent function accounting for the dissipation energy per unit time in the system. Finally, the external energy, W_{ext}, introduced by the external loads, is defined as

$$W_{\text{ext}}(t) = \int_0^l \mathbf{q}(x,t)\frac{\partial \mathbf{u}}{\partial t}\mathrm{d}x. \tag{3.77}$$

where $\mathbf{q}$ is a generalized load. The energy variation law will be used in the following chapter as a tool for identification of energy dissipation in several structures.

4

DAMPING IDENTIFICATION IN STRUCTURAL ELEMENTS BY MEANS OF ENERGY-FLUX ANALYSIS

This chapter presents and applies a novel method to identify damping based on energy-flux analysis. The concept of energy flux is well-established in different fields [9–19]. However, to the best knowledge of the author, in the field of structural mechanics and for identification, it has never been used. The majority of damping identification methods are based on experimental modal analysis [40–42]. With these methods, an effective modal damping associated with all locations of a structure is identified. Sometimes, if enough modes are used, specific locations where energy is dissipated can be identified. However, this is an unexpected scenario in structures subjected to ambient conditions. Thus, the work presented in this chapter aims to develop an identification method that does not require a modal representation of the structure's motion.

To show the applicability of the energy-flux analysis for identification purposes, measurements from two lab-scale structures are used. First, in Section 4.1, the energy-flux analysis is applied to identify the damping of a steel beam. Second, in Section 4.2, the energy method is applied for damping identification for a five-storey lab-scale steel-frame building. The damping identified in each of the connections is later used for a global model to identify the overall structure damping. The resultant damping obtained by means of the energy-flux analysis shows good agreement with the experimentally verified damping for a wide frequency range in both cases.

4.1. DAMPING IDENTIFICATION IN A CANTILEVER BEAM BY MEANS OF ENERGY-FLUX ANALYSIS

In this section the energy dissipation of a cantilever steel beam, as shown in Fig.4.1, is identified by means of energy-flux analysis. Measurement data is used to validate the re-

sults. The goal of this section is to introduce the energy-flux analysis for damping identification using a simple mechanical system, such as the cantilever beam.

4.1.1. EXPERIMENTAL IDENTIFICATION OF THE CANTILEVER BEAM PROPERTIES

The lab-scale beam is instrumented using the three accelerometers located at the top, middle and bottom positions of the beam height, as shown in Fig. 4.1. The accelerometers are positioned so that only accelerations in the weak direction are registered.
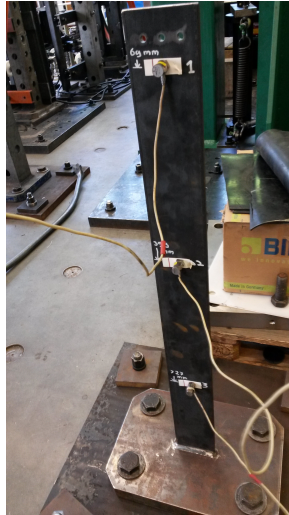
Figure 4.1: Lab-scale cantilever beam instrumented with accelerometers at the top, middle and bottom part of the beam height.

Physical and geometrical characteristics of the beam are described in Table 4.1.

Height[m]	Width[m]	Depth[m]	ρA[Kg/m]
1	0.01	0.001	7.85

Table 4.1: Characteristics of the beam.

During experimental identification, the lower modes and the damping ratio associated to each mode are identified using the accelerometers on the beam. Thus, a hammer impact test is conducted, knocking with a hammer atop the beam. Having deflected the beam in the weak inertial direction by the hammer impact, the beam vibrates freely. Consequently, a free-decay signal is produced by each accelerometer on the beam, as shown in Fig. 4.2.

It becomes clear, looking at Fig. 4.2 that the beam loses energy at each oscillation. However, the time-domain signal does not clearly show which modes participate in the vibration process. Therefore, a frequency domain analysis of the top accelerometer signal
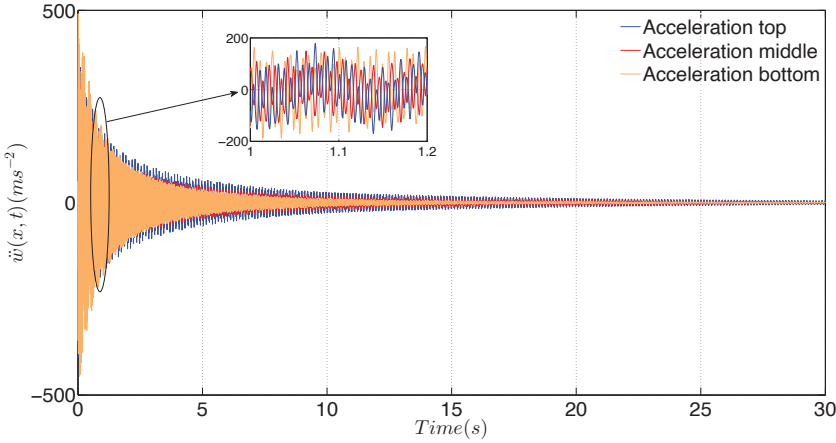
Figure 4.2: Measured response of the cantilever beam subjected to a hammer impact.

is conducted to visualize the modes participating in the vibration process. The result of applying FFT atop the accelerometer is shown in Fig. 4.3, showing how the four lower modes are excited by the hammer impact.
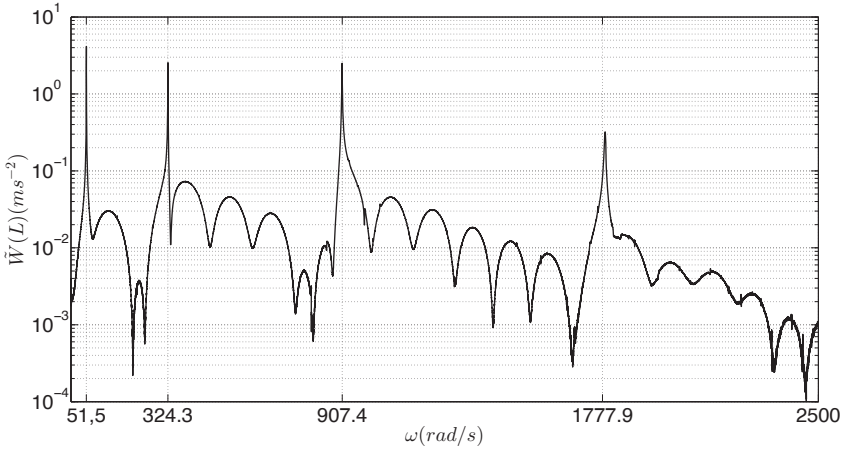
Figure 4.3: Frequency response function amplitude of the cantilever beam subjected ta a hammer impact.

Fig. 4.2 shows that the time domain response gives a marginal insight into the frequency content of the signal. However, frequency analysis reveals the frequency signal content as shown in Fig. 4.3. However, knowledge of the time content is lost. Therefore, to see into the time-frequency content of the signal, the short-time Fourier transform (STFT)

[43, 44] is applied to the recorded signal of the accelerometer, located atop the beam.
The integral representation of the STFT is as follows:

$$\text{STFT}(t,\omega) = \int_{-\infty}^{\infty} x(\tau)\, w(t-\tau)\, e^{-\mathrm{i}\omega\tau}\, d\tau \tag{4.1}$$

where $x(t)$ is the signal to be transformed, and $w(t-\tau)$ is the window function. The
main idea of the STFT is to analyse the frequency content of a signal, focusing on a spe-
cific time interval, neglecting the rest of the signal. In this experiment, the sampling
frequency is set to 2000 Hz. Therefore, to obtain the time-frequency representation of
the recorded signal, a discrete version of the STFT is computed as shown in Eq. 4.2.

$$\text{STFT}(k,l) = \sum_{n=1}^{N-1} x(k-n)\, w(n)\, e^{-\mathrm{i}\frac{2\pi}{N} ln} \tag{4.2}$$

where $n = 0, 1, 2.., \text{and} N-1$ are the number of discrete steps. k and l are the time-
frequency grid, and $w(n)$ is the window function. The improvement in time localiza-
tion comes at the expense of frequency resolution. This means that the shorter the time
sample, the better the time resolution and the worse the frequency resolution. The fre-
quency resolution is mainly compromised by the window function. STFT normally uses
a rectangular window function, given the simplest representation of a window function.
An improvement of the STFT is the Gabor transform [45], which uses the same STFT.
In this transform, a Gaussian window function, w_{Gaussian}, is used. The use of this win-
dow function improves the frequency resolution. Moreover, different window functions
have been implemented to show either improvement or worsen the frequency resolu-
tion. Several window functions are described in Eq. 4.3.

$$w_{\text{rect}}(n) = k$$
$$w_{\text{Gaussian}}(n) = e^{-1/2(\alpha\frac{n}{N/2})^2} \qquad \text{where} \qquad \frac{-N}{2} \le n \le \frac{N}{2}$$
$$w_{\text{Hann}}(n) = 0.5\left(1 - \cos\left(2\pi\frac{n}{N}\right)\right) \qquad \text{where} \qquad 0 \le n \le N \tag{4.3}$$
$$w_{\text{Hamming}}(n) = 0.54 - 0.46\cos\left(2\pi\frac{n}{N}\right) \qquad \text{where} \qquad 0 \le n \le N$$

Figure 4.4 shows the results of Eq. 4.2 with the different window functions.
It can be noted, looking at Fig. 4.4, that the time-frequency analysis making use of the
rectangular window function gives the worst frequency resolution, whereas the analysis
making use of the Gaussian and the Hann window give an improvement of frequency
resolution. Figure 4.4 also reveals that higher frequency modes vanish faster, allowing
the beam to vibrate at the fundamental frequency until all of the energy input into the
beam is dissipated.
Having identified the modes participating in the vibration process, the damping ratio
associated with each mode is identified via logarithmic decay analysis (Eq. 2.32) pro-
duced by the three accelerometers. To identify the damping associated with each mode,
a low-high bandpass filter is applied to the signal. Table 4.2 shows the damping ratios.
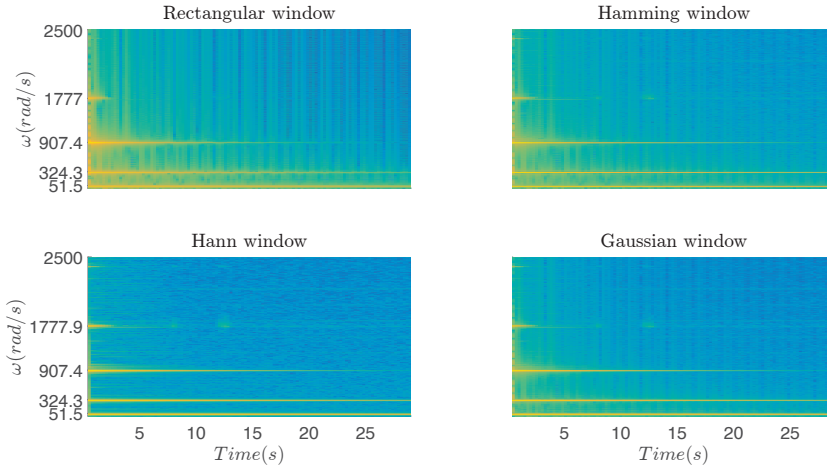
Figure 4.4: Time-frequency response function of the cantilever beam subjected to a hammer impact.

Mode	ω [rad/s]	ξ_1[%]	ξ_2[%]	ξ_3[%]
1	51.5	0.14%	0.14%	0.14%
2	324.3	0.3%	0.3%	0.3%
3	907.4	1.1%	1.1%	1.1%
4	1777.9	6.6%	6.6%	6.6%

Table 4.2: Characteristics of the beam.

In Table 4.2, ξ_1, ξ_2 and ξ_3 account for the damping identified by the data recorded by the accelerometer at the top, middle and bottom of the beam respectively. Table 4.2 shows that the modal damping ratio is larger for higher modes. This aligns with the outcome of the time-frequency analysis, which shows that higher modes vanish faster. Furthermore, the damping ratio is the same at different measurement locations for each mode.

4.1.2. IDENTIFICATION OF ENERGY DISSIPATION OF THE CANTILEVER BEAM BY MEANS OF ENERGY-FLUX ANALYSIS

In this section, the energy dissipation in the cantilever beam shown in Fig. 4.1 is identified by means of energy-flux analysis. To support the energy-flux analysis, a model of the cantilever beam is used. Therefore, the lab-scale beam is modelled with a bending-beam model, using internal material damping. The Lagrangian density function of a Euler-Bernoulli bending beam can be defined as

$$\lambda\left(x, t, \mathbf{u}, \dot{\mathbf{u}}, \mathbf{u}''\right) = \frac{1}{2}\rho A\left(\dot{w}_z(z,t)\right)^2 - \frac{1}{2}EI\left(w_z''(z,t)\right)^2 \tag{4.4}$$

where the independent coordinate is $\mathbf{u} = w(z,t)$. The dissipation in the material is described in the constitutive model as

$$\sigma = \left(E + E^* \frac{\partial}{\partial t} \right) \epsilon. \tag{4.5}$$

By introducing Eqs. 4.4-4.5 into Eqs. 3.70-3.72, the equation of motion and boundary conditions of a bending beam model can be written as follows:

$$\rho A \frac{\partial^2 w(z, t)}{\partial t^2} + \left(E^* \frac{\partial}{\partial t} + E \right) I \frac{\partial^4 w(z, t)}{\partial z^4} = \delta(z - L) F(t) \tag{4.6}$$

$$w(0, t) = \frac{\partial w(0, t)}{\partial z} = 0$$

$$\left(E^* \frac{\partial}{\partial t} + E \right) I \frac{\partial^2 w(L, t)}{\partial z^2} = \left(E^* \frac{\partial}{\partial t} + E \right) I \frac{\partial^3 w(L, t)}{\partial z^3} = 0 \tag{4.7}$$

Where $F(t)$ is the input force in this case given by the hammer, ρA is the mass per unit length and EI is the bending stiffness of the beam. The hammer force is approximated to the measured one by a piecewise function as shown in Fig. 4.5.
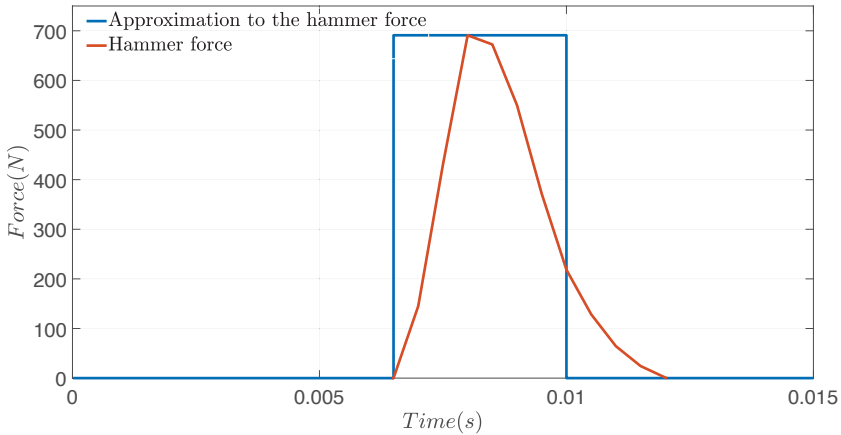
Figure 4.5: Measured hammer force applied to the beam and a square function approximation to the measured hammer force.

Neglecting material damping in the boundary conditions, the solution of Eq. 4.6 can be sought for, in the form of the superposition of the multiplication of a function of the co-ordinate (modal shapes) and a function of time as

$$w(z, t) = \sum_{n=1}^{N_{\text{modes}}} W_n(z) \psi_n(t). \tag{4.8}$$

Substituting the above solution into Eqs. 4.6- 4.7, the following expressions can be written:

$$\sum_{n=1}^{N_{\text{modes}}} \left(\ddot{\psi}_n(t) + \frac{E^* I}{\rho A} \dot{\psi}_n(t) + \omega_n^2 \psi_n(t) \right) W_n(z) = \frac{\delta(z-L)F(t)}{\rho A} \tag{4.9}$$

$$W_n(0) = \frac{\partial W_n(0)}{\partial z} = 0$$

$$EI \frac{\partial^2 W_n(L)}{\partial z^2} = EI \frac{\partial^3 W_n(L)}{\partial z^3} = 0 \tag{4.10}$$

where $\omega_n^2 = \beta_n^4 EI/\rho A$. Next, Eq. 4.9 is multiplied by the function, $W_m(z)$, and integrated over the length of the beam, as follows:

$$\int_0^L \left\{ \left(\ddot{\psi}_n(t) + \frac{E^* I}{\rho A} \dot{\psi}_n(t) + \omega_n^2 \psi_n(t) \right) W_n(z) \right\} W_m(z) \mathrm{d}z = \int_0^L \left\{ \frac{\delta(z-L)F(t)}{\rho A} \right\} W_m(z) \mathrm{d}z \tag{4.11}$$

The integral of the multiplication, $\int_0^L W_n(z) W_m(z) \mathrm{d}z$ is non-zero only if $m \neq n$. Then, the time-dependent part of the equation of motion reads

$$\ddot{\psi}_m(t) + \omega_m \zeta_m \dot{\psi}_m(t) + \omega_m^2 \psi_m(t) = \frac{F(t)}{\rho A} \Gamma_m = Q_m(t) \tag{4.12}$$

where

$$\Gamma_m = \frac{W_m(L)}{\int_0^L W_m(z) W_m(z) \mathrm{d}z}. \tag{4.13}$$

The time function, $\psi_m(t)$, can be sought for in the following form, assuming zero initial conditions.

$$\psi_m(t) = \begin{cases} 0 & t \leq t' \\ \frac{1}{\omega_m} \int_0^t Q_m(t') e^{-\zeta_m \omega_m(t-t')} \sin(\omega_{\mathrm{d}_m}(t-t')) \mathrm{d}t' & \text{otherwise} \end{cases} \tag{4.14}$$

where $\omega_{\mathrm{d}_m} = \omega_m \sqrt{1 - \zeta_m^2}$. The modal shapes and natural frequencies can be found, assuming the following general solution:

$$W_m(z) = C_1 \cosh(\beta_m z) + C_2 \sinh(\beta_m z) + C_3 \cos(\beta_m z) + C_4 \sin(\beta_m z) \tag{4.15}$$

where $C_i (i = 1..4)$ are constants to be determined. Substituting Eq. 4.15 into Eq. 4.10, a set of equations can be written in matrix notation.

$$\mathbf{A}c = 0, \tag{4.16}$$

where $\mathbf{A}$ is a $4x4$ matrix, and c is a $4x1$ vector containing the constants, $C_i (i = 1..4)$. Next, solving the determinant of matrix $\mathbf{A}$,

$$\det|\mathbf{A}(\beta_m)| = 0, \tag{4.17}$$

whose coefficients are described in Appendix A.1, the natural frequencies of the cantilever beam, neglecting damping can be calculated. Thereafter, the constants $C_i (i = 1..4)$ can be calculated. Thus, the total solution can be written as

$$w(z, t) = \sum_{m=1}^{N_{\text{Modes}}} W_m(z) \begin{cases} 0 & t \le t' \\ \frac{1}{\omega_m} \int_0^t Q_m(t') e^{-\zeta_m \omega_m (t-t')} \sin(\omega_{d_m} (t - t')) dt' & \text{otherwise} \end{cases} \tag{4.18}$$

The analytical expression given by Eq. 4.18 is used to compute the energy dissipation in the beam. In more complex mechanical systems, where analytical expressions cannot be easily found, measurement data is used to compute the energy dissipation.

To calculate the energy dissipation, the energy balance equation is formulated as

$$W_{\text{diss}}(t) = W_{\text{ext}}(t) - \frac{d\mathcal{H}(t)}{dt} - S(z, t)|_0^L \tag{4.19}$$

where $\mathcal{H}(t)$ is computed by means of Eqs. 3.74-3.75, leading to the following expression:

$$\mathcal{H}(t) = \int_0^L \left\{ \frac{1}{2}\rho A \left(\frac{\partial w(z, t)}{\partial t} \right)^2 + \frac{1}{2} EI \left(\frac{\partial^2 w(z, t)}{\partial z^2} \right)^2 \right\} dz \tag{4.20}$$

The energy flux is computed with Eq. 3.76, resulting in the following expression:

$$S(z, t) = EI \left(\frac{\partial^2 w(z, t)}{\partial z^2} \frac{\partial^2 w(z, t)}{\partial z \partial t} - \frac{\partial^3 w(z, t)}{\partial z^3} \frac{\partial w(z, t)}{\partial t} \right) = \left(M \frac{\partial^2 w(z, t)}{\partial z \partial t} - Q \frac{\partial w(x, t)}{\partial t} \right) \tag{4.21}$$

where M is the bending moment, and Q is the shear force (Appendix D). The external energy corresponds to the energy introduced to the beam by means of a hammer impact, computed from Eq. 3.77, as follows:

$$W_{\text{ext}}(t) = \int_0^L \delta(z - L) F_{\text{hammer}}(t) \frac{\partial w(z, t)}{\partial t} dz. \tag{4.22}$$

By substituting Eq. 4.18 into Eqs. 4.20-4.22, energy dissipation $W_{\text{diss}}(t)$ in the beam can be computed. On the other hand, the energy dissipation can be computed directly, using the assumed damping operator (the Kelvin-Voigt model in the example above):

$$W_{\text{diss}}(t) = E^* \int_0^L \frac{\partial^5 w(z, t)}{\partial z^4 \partial t} \frac{\partial w(z, t)}{\partial t} dz \tag{4.23}$$

The dissipated energy computed using Eq. 4.19 and Eq. 4.23 should be equivalent, which allows one to determining the damping constant. For the example considered in this section, the expression for E^* can be found as:

$$E^* = \frac{\int_t W_{\text{diss}}(t)\,\mathrm{d}t}{\int_t \int_0^L \frac{\partial^5 w(z,t)}{\partial z^4 \partial t} \frac{\partial w(z,t)}{\partial t}\,\mathrm{d}z\mathrm{d}t} \tag{4.24}$$

To validate the obtained damping constant, the response measured by means of the experimental test is compared to the response of the beam model, making use of the identified damping, E^*.
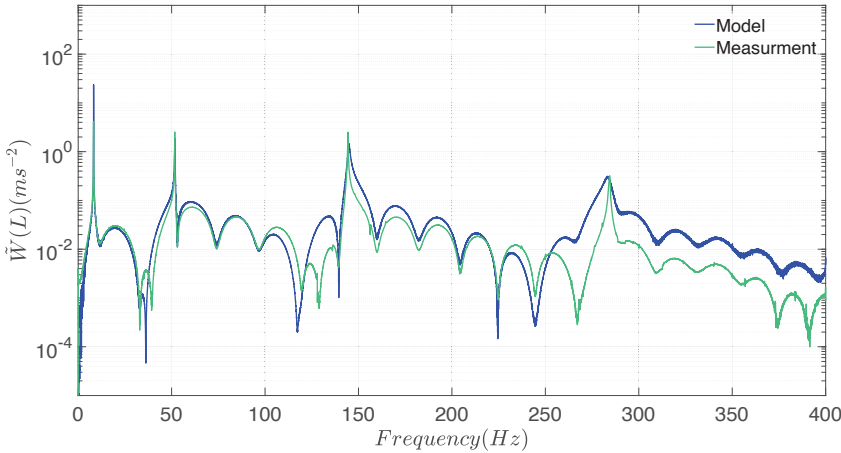
Figure 4.6: Comparison of the beam response using of the identified damping by means of the energy-flux analysis with the experimental response in the frequency domain.

Figure 4.6 shows good agreement between the model response and the experimental response especially for the three lower modes. The agreement for the fourth mode ($f = 279.9$Hz) is poorer, which means that the adopted model is, probably, insufficiently accurate at higher frequencies. In the following sections, the energy-flux analysis is used to identify local damping of more complex structures making use of experimental data.

4.2. IDENTIFICATION OF ENERGY DISSIPATION IN STRUCTURAL JOINTS BY MEANS OF ENERGY-FLUX ANALYSIS

In this section, energy-flux analysis is used to identify the local damping of a steel frame lab-scale building structure. The elements of the structure are bolt connected. It is therefore assumed that the main source of energy dissipation takes place in the bolted joints of the structure. Consequently, an energy balance equation around the connection areas is formulated, and energy dissipation is identified. The identified energy dissipation, by means of the energy flux analysis, is later compared to the experimental response of the lab-scale structure.

4.2.1. EXPERIMENTAL WORK

The experimental set-up shown in Fig. 4.7 was constructed and tested in the Materials and Structures Laboratory of Sapienza University, Rome. It consists of a steel frame structure with five concrete slabs distributed uniformly by height. The concrete slabs are supported by L-shape steel beams connected to the columns of the structure with bolts, as shown in Fig. 4.7. The structure is mounted on a shaking table, which provides the base excitation. The characteristics of the set-up are described in Table 4.3. The fundamental frequency, ω_1, and damping ratio, ξ_1, are identified by means of the exponentially decaying function of a free vibration test, making use of the shaking table.
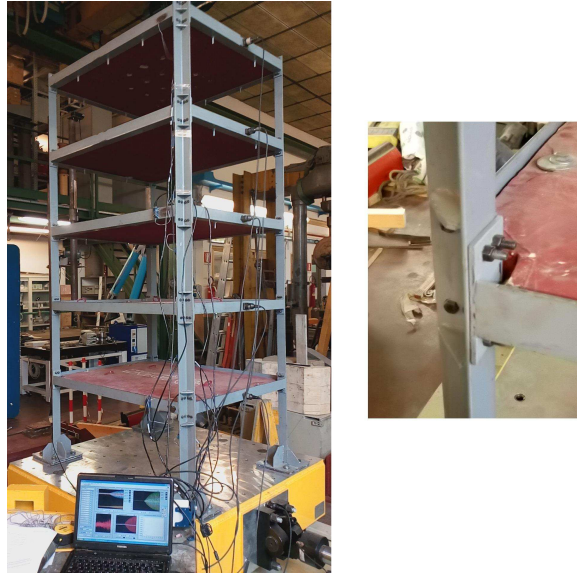
Figure 4.7: Experimental set-up: 5-storey steel-building model mounted on the Moog shaking table with the first instrumentation configuration and acquisition system.

Height[m]	Width[m]	Depth[m]	ω_1[rad/s]	ξ_1[%]
2.5	1.2	0.9	28.1	1.22

Table 4.3: Lab-scale structure characteristics.

The structure is instrumented with eight strain gauges, five accelerometers and two displacement sensors. Five strain gauges are glued to one column between each bolted connection, and three are mounted on an L-shape beam supporting the concrete slabs, near the connections with the first, third and fifth storey. In the first instrumentation configuration, accelerometers are placed on the L-shape steel beams supporting the concrete slabs at each floor (Fig. 4.7). The recorded data is used to identify the equivalent stiffness matrices of the lab-scale structure. Thereafter, in the second instrumentation configuration, to identify energy dissipation in the joints, accelerometers are repositioned near

the strain gauges to measure the accelerations and strains at the locations shown in Fig.
4.8.

Figure 4.8: Experimental set-up: Second instrumentation configuration for the energy-flux analysis.

A displacement sensor is located at the top floor, measuring the horizontal displacement
in the weak direction of the fifth storey, whereas the other is fixed to the shaking table.
A channel in the acquisition system is reserved for a force sensor placed at the tip of the
hammer used to excite the structure. The data recorded by the hammer-force sensor are
used for the stiffness identification and validation of the model.

STIFFNESS IDENTIFICATION

In this section, the procedure employed to identify the equivalent stiffness of the lab-
scale structure is described. The mass of the structure is measured directly and does
not need to be identified. A combination of the peak picking method [46] and modal
analysis is used to identify the equivalent stiffness matrix. Based on the results of a
hammer-impact test, the Fourier spectrum of vibrations of each floor is obtained and
the peak-picking method can be used to identify the eigenvectors of the model depicted
in Fig. 4.7 from the imaginary part of the spectrum. This methodology is applicable be-
cause the modes are well-separated, and the relative displacements of the structure are
marginally influenced by damping. Therefore, damping in the system can be neglected
during eigenvector identification. Thereafter, the remaining part of the modal analysis
can be carried out.

MODAL ANALYSIS

The accelerations measured via piezoelectric accelerometers (PCB Piezotronics, Inc.) in
an impact hammer test are shown in Fig. 4.9. The real and imaginary parts of the Fourier
spectrum of the corresponding displacements are shown in Fig. 4.10.
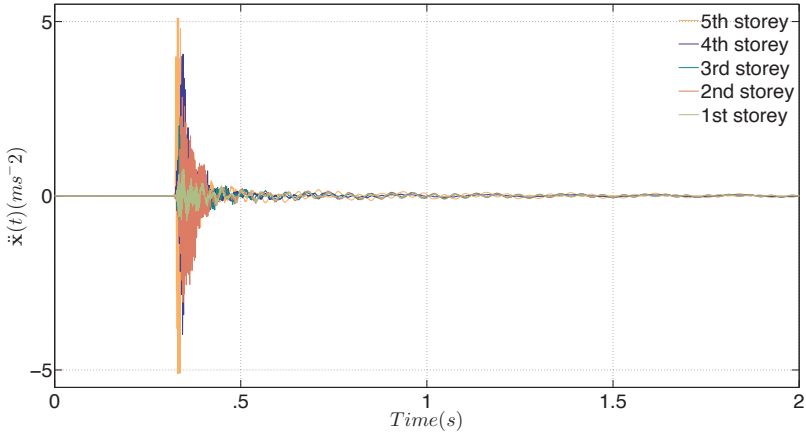
Figure 4.9: Time domain response of each storey of the structure to a hammer impact.

Based on this data, modal analysis is conducted. First the corresponding 5-DoF system is introduced under the assumption of negligible damping.

$$\mathbf{M}\ddot{\mathbf{x}}(t) + \mathbf{K}\mathbf{x}(t) = \mathbf{0} \tag{4.25}$$

where $\mathbf{M}$ and $\mathbf{K}$ are $5x5$ real-valued equivalent mass and equivalent stiffness matrices. Matrix $\mathbf{M}$ is diagonal containing the masses of the floors. Matrix $\mathbf{K}$ is subject to identification. To identify $\mathbf{K}$, the displacement vector, $\mathbf{x}(t)$, of the effective system, is assumed in the modal form.

$$\mathbf{x}(t) = \sum_{i=1}^{n} \hat{\mathbf{x}}_i u_i(t) = \boldsymbol{\phi}\mathbf{u(t)} \tag{4.26}$$

where $\boldsymbol{\phi}$ is the eigenmatrix, and $u_i(t) = A_i\sin(\omega_i t + \Phi_i)$ are the normal coordinates, in which ω_i are the natural frequencies and Φ_i are the phases. Both the natural frequencies and the eigenmatrix are identified, based on the impact hammer test, using a technique described in [46], based on the spectrum of the measured accelerations shown in Fig. 4.10.
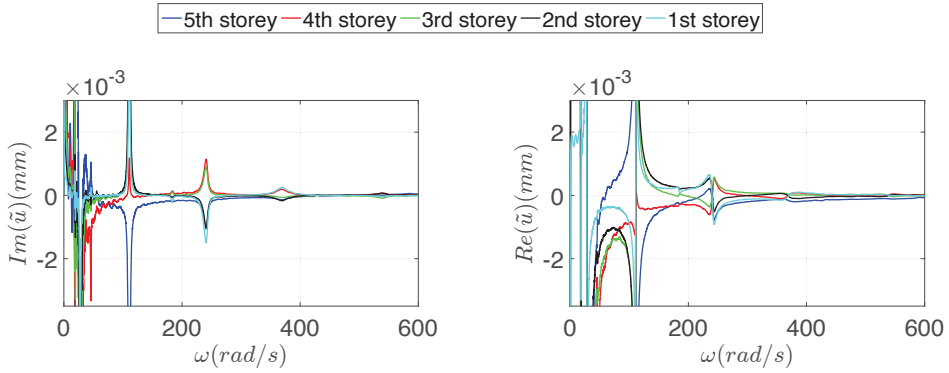
Figure 4.10: Frequency response: (a) imaginary part; (b) real part.

With ω_i and $\boldsymbol{\phi}$ identified, the modal stiffness matrix, $\mathbf{K}^* = \boldsymbol{\phi}^T \mathbf{K} \boldsymbol{\phi}$, can be calculated using the following equation:

$$\omega_i^2 \boldsymbol{\phi}^T \mathbf{M} \boldsymbol{\phi} \mathbf{u}(t) = \mathbf{K}^* \mathbf{u}(t) \tag{4.27}$$

The identified mode shapes, $\boldsymbol{\phi}$, and natural frequencies, ω_i, of the structure are shown in Fig. 4.11.
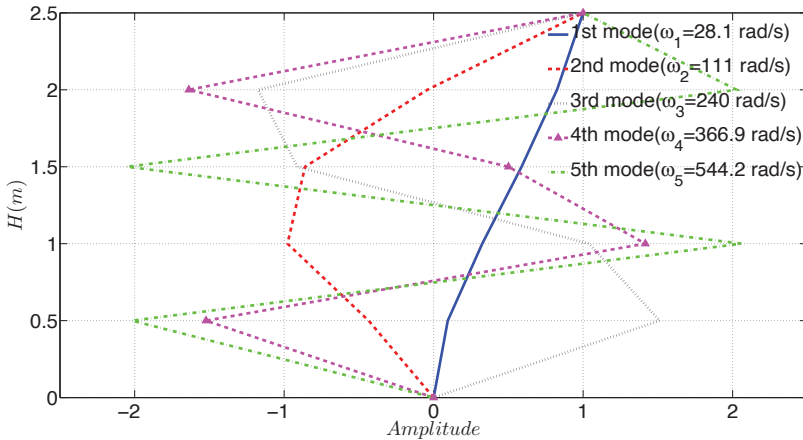
Figure 4.11: Experimentally identified mode shapes of the lab-scale structure.

4.2.2. Problem formulation and energy-flux analysis

Energy dissipation in rigid bolted connections is investigated by means of an energy method and validated using a the lab-scale structure, as shown in Fig. 4.7. It is assumed that energy is dissipated in the bolted connections only. Each bolted connection is described by springs and dashpots. The springs mimic the elastic resistance of the connection, and the dashpots are responsible for energy dissipation. As first step of the identification procedure, the spring stiffness representative of the connections should be parametrized. Next, the dashpots are parametrized by means of the energy method. The energy dissipated in the bolted connections is studied in each connection individually. The overall energy dissipation obtained with the proposed method is later validated using an effective 5-DoF-system. To this end, the equivalent stiffness, **K** and equivalent mass, **M**, representative of the lab-scale structure identified by means of a hammer impact test, are used.

Stiffness parametrization

The first step to identifying the energy dissipated in a given system is determining the distribution of the elastic and inertial properties of the system. The inertial properties can be identified straightforwardly, whereas the elastic parameters are more difficult to determine. To identify the latter, a model representative of the lab-scale structure is implemented, as shown in Fig. 4.12.
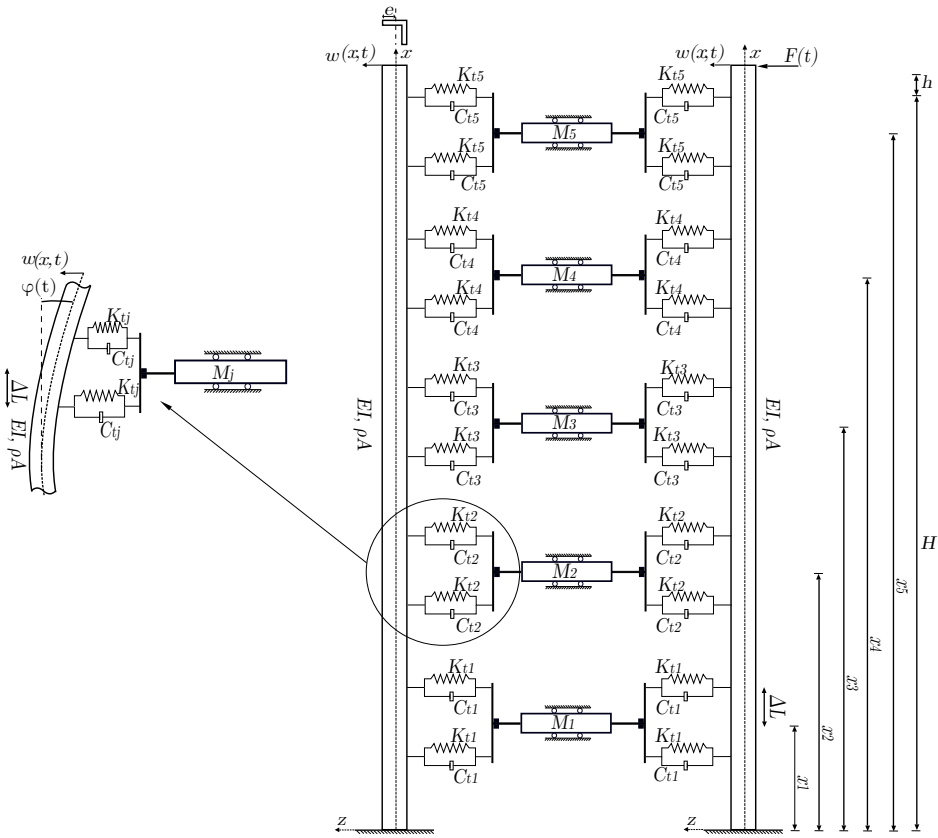
Figure 4.12: Euler-Bernoulli beams with discrete springs and masses, representing the lab-scale structure.

The model consists of two parallel Euler–Bernoulli beams with uniformly distributed masses, ρA, and bending rigidity, EI, along the height, $H + h$, five discrete masses, M_j, four translational springs, K_{t_j} and four dashpots, C_{t_j}, per floor. The stiffness, K_{t_j}, only accounts for the stiffness in the joints of the lab-scale structure, whereas, **K**, accounts for the total stiffness of the structure (e.g. joints, columns). The Euler-Bernoulli beams represent the columns of the lab-scale structure (see Fig. 4.12). While vibrating, beams experience in-plane (xz) deformation, while the masses representing the concrete horizontal slabs (floors) do not deform. However, they are slaved to the beams' displacements. The springs represent the elastic resistance of the structural joints and attach the slabs to the columns. The dashpots represent the dissipative elements of the joints. The springs and dashpots can deform, as shown in Fig. 4.12. The deformation of these elements is relative to the deformation of the beams, as $\Delta L\varphi = w(\Delta L + x_j) - w(x_j)$ for the upper spring and dashpot elements, and as $\Delta L\varphi = w(\Delta L - x_j) - w(x_j)$ for the lower spring and dashpot elements, respectively.

By applying the Euler-Bernoulli beam theory and assuming geometric linearity, it can be

stated that the beam cross-section is not deformable and that the transverse displacement is uniform. Therefore, the axial deformation results from the rotation of the cross section as follows:

$$\epsilon_{zz} = 0 \qquad \epsilon_{xx} = -e\frac{\partial^2 w(x,t)}{\partial x^2} \qquad \text{with} \qquad \frac{\partial w(x,t)}{\partial x} = \varphi(t). \qquad (4.28)$$

Where e is the distance from the neutral fibre to the edge of the cross-section of the beam, as shown in Fig 4.12. Subsequently, the equation of motion governing small vibrations of the system, assuming both beams are subjected to the same deflection, $w(x,t)$, can be formulated as follows:

$$2\rho A\frac{\partial^2 w(x,t)}{\partial t^2} + 2EI\frac{\partial^4 w(x,t)}{\partial x^4} + \sum_{j=1}^{N_{\text{storeys}}} 2\left(K_{t_j} + C_{t_j}\frac{\partial}{\partial t}\right)$$
$$\left[\delta\left(x - x_j - \Delta L\right)\left(w(x,t) - w(x_j,t)\right) + \delta\left(x - x_j + \Delta L\right)\left(w(x,t) - w(x_j,t)\right)\right] \qquad (4.29)$$
$$- \delta(x - x_j)M_j\frac{\partial^2 w(x,t)}{\partial t^2} = 0$$

with the following boundary conditions:

$$w(0,t) = \frac{\partial w(0,t)}{\partial x} = 0$$
$$EI\frac{\partial^2 w(H+h,t)}{\partial x^2} = 0 \qquad (4.30)$$
$$EI\frac{\partial^3 w(H+h,t)}{\partial x^3} = -F(H+h,t)$$

The force, $F(H+h,t)$, is an external force applied atop the lab-scale structure by means of an impact hammer. The stiffnesses, K_{t_j}, of the joints, are determined such that the lowest five natural frequencies of the model match the corresponding natural frequencies identified experimentally by the hammer-impact test. The frequency shift associated with damping, C_{t_j}, is neglected, because damping in the structure is quite low, as shown later.

ENERGY-FLUX ANALYSIS
The overall energy dissipation in the lab-scale structure is investigated by considering energy dissipation in each connection. Thus, the model shown in Fig. 4.13 and its data collected via the second instrumentation configuration are employed. The rotational deformation of each connection is represented via visco-elastic elements, as shown in Fig. 4.13.
Figure 4.13 also shows a short segment of the beams adjacent to the joint, the mass of the floor and a detailed view of the joint model. The joint is assumed to be rigid in the horizontal direction, such that a horizontal displacement of the beam element is the same as the mass. Simultaneously, the joint provides a visco-elastic resistance to the rotational motion of the beam.
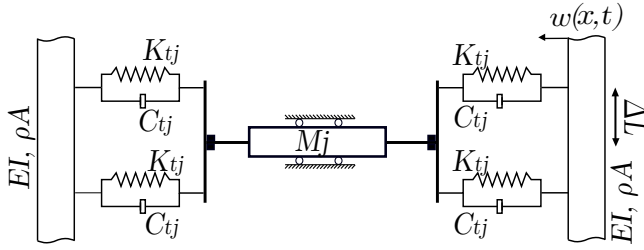
Figure 4.13: Euler-Bernoulli beams with springs and dashpots representing the connection of the first storey of the lab-scale building.

To formulate the energy variation equation for a single floor, as shown in Fig. 4.13, the equation of motion is multiplied by the velocity term, $\frac{\partial w(x,t)}{\partial t}$, and integrated between $x_j - \Delta L$, and $x_j + \Delta L$, as follows:

$$
\int_{x_j-\Delta L}^{x_j+\Delta L} \frac{\partial w(x,t)}{\partial t} \left\{ 2\rho A \frac{\partial^2 w(x,t)}{\partial t^2} + 2EI \frac{\partial^4 w(x,t)}{\partial x^4} + \sum_{j=1}^{N_{\text{storeys}}} 2\left(K_{t_j} + C_{t_j}\frac{\partial}{\partial t}\right) \right.
$$
$$
\left(\delta\left(x - x_j - \Delta L\right)\left(w(x,t) - w(x_j,t)\right) + \delta\left(x - x_j + \Delta L\right)\left(w(x,t) - w(x_j,t)\right)\right)
$$
$$
\left. -\delta(x - x_j)M_j \frac{\partial^2 w(x,t)}{\partial t^2}\right\} dx = 0.
$$
(4.31)

The above equation can be written in the form of the energy variation equation as

$$
\frac{dE_j(t)}{dt} + S(x,t)\big|_{x_j-\Delta L}^{x_j+\Delta L} = W_{\text{Diss}_j}(t)
$$
(4.32)

where,

$$
E_j(t) = \frac{1}{2}\left[M_j \left(\frac{\partial w(x_j,t)}{\partial t}\right)^2 + 4K_{t_j}\Delta L^2 \left(\frac{\partial w(x_j,t)}{\partial x}\right)^2 \right] + \mathscr{H}_{j_{\text{beam}}}(t)
$$
(4.33)

and the Hamiltonian energy of the bending beam, $\mathscr{H}_{j_{\text{beam}}}(t)$, can be expressed as

$$
\mathscr{H}_{j_{\text{beam}}}(t) = \int_{x_j-\Delta L}^{x_j+\Delta L} \frac{1}{2}\left[2\rho A \left(\frac{\partial w(x,t)}{\partial t}\right)^2 + 2EI \left(\frac{\partial^2 w(x,t)}{\partial x^2}\right)^2 \right] dx
$$
(4.34)

$E_j(t)$ is the energy of the considered segment of the system comprising the kinetic and the elastic energies stored in the beam segment and in the springs. $S(x,t)$ is the energy flux crossing the boundaries of this segment, located at $x = x_j \pm \Delta L$. It can be obtained by means of Eq. 3.76. This leads to

$$
S(x,t) = 2\left(M\frac{\partial \varphi(t)}{\partial t} - Q\frac{\partial w(x,t)}{\partial t}\right)
$$
(4.35)

where M is the bending moment, and Q is the shear force. Therefore, energy flux is computed as the bending moment multiplied by the time rate of the rotation and the shear force multiplied by the velocity. Consequently, W_{Diss_j} is the energy dissipated within the chosen segment of the system. Thus, Eq. 4.32 shows that the energy change in the system is balanced by the energy flux through the boundaries of the segment and the energy dissipated in the segment.

4.2.3. QUANTIFICATION OF THE ENERGY DISSIPATION

To quantify the energy dissipated in the segment j, W_{Diss_j}, the structure is excited by a base harmonic motion via the shaking table. The excitation pumps in energy at the fundamental natural frequency, lasting long enough to achieve the steady-state response. It is chosen to excite the system at its natural frequency, owing to the well-known fact that resonance vibrations are most sensitive to damping. As mentioned above, accelerometers and strain gauges are both positioned, as described in the second instrumentation configuration shown in Fig. 4.8, to enable the calculation of the energy flux and energy defined by Eqs. 4.32-4.35.

By using the accelerations and the strains measured in the vicinity of the joints, the total energy (left-hand side of Eq. 4.32) per storey can be computed and evaluated to give an expression for the dissipated energy.

Experimental observations suggest that the energy dissipation in the system shown in Fig. 4.7 is caused by the rotational deformation around the joints. Therefore, per this observation and Eq. 4.31, the dissipated energy is expressed as

$$
\begin{aligned}
W_{\text{Diss}_j}(t) = \int_{x_j-\Delta L}^{x_j+\Delta L} & 2C_{t_j} \frac{\partial w(x,t)}{\partial t} \left[\delta\left(x-x_j-\Delta L\right)\left(\frac{\partial w(x,t)}{\partial t} - \frac{\partial w(x_j)}{\partial t}\right) + \right. \\
& \left. \delta\left(x-x_j+\Delta L\right)\left(\frac{\partial w(x,t)}{\partial t} - \frac{\partial w(x_j)}{\partial t}\right) \right] dx = \\
& 2C_{t_j}\left[\dot{w}^2(x_j+\Delta L) - \dot{w}(x_j+\Delta L)\dot{w}(x_j) \right. \\
& \left. + \dot{w}^2(x_j-\Delta L) - \dot{w}(x_j-\Delta L)\dot{w}(x_j) \right].
\end{aligned}
\tag{4.36}
$$

To identify the effective damping coefficient, C_{t_j}, it is instrumental to compute a cumulative dissipated energy within a period, T. This can be done by integrating the energy variation of Eq. 4.32 over time.

$$
E_j(t)\big|_{t_0}^{t_0+T} + \int_{t_0}^{t_0+T} S(t,x)\big|_{\Delta x_j-\Delta L}^{\Delta x_j+\Delta L} dt = \int_{t_0}^{t_0+T} W_{\text{Diss}_j}(t)\,dt
\tag{4.37}
$$

where $E_j(t)$ is given by Eq. 4.33, $W_{\text{Diss}_j}(t)$ is given by Eq. 4.36 and $S(x,t)$ is given by Eq. 4.35. Therefore, from Eq. 4.36 and Eq. 4.37, C_{t_j} can be computed as

$$
C_{t_j} = \frac{E_j(t)\big|_{t_0}^{t_0+T} + \int_{t_0}^{t_0+T} S(t,x)\big|_{x_j-\Delta L}^{x_j+\Delta L}}{2\int_{t_0}^{t_0+T}\left(\dot{w}^2(x_j+\Delta L) - \dot{w}(x_j+\Delta L)\dot{w}(x_j) + \dot{w}^2(x_j-\Delta L) - \dot{w}(x_j-\Delta L)\dot{w}(x_j)\right)dt}
\tag{4.38}
$$

The numerator of Eq. 4.38 consists of the left-hand side of Eq. 4.32, computed by the measured strains and accelerations in the vicinity of the joints per storey, as shown in Fig. 4.8. The denominator of Eq. 4.38 is evaluated computing the velocities at specified locations of each storey. The damping coefficients, C_{tj}, so obtained are independent of the time period, T, if the latter is sufficiently large, as demonstrated in Fig. 4.14. The damping coefficient of the first floor, resulting from Eq. 4.38, is shown in Fig. 4.14.
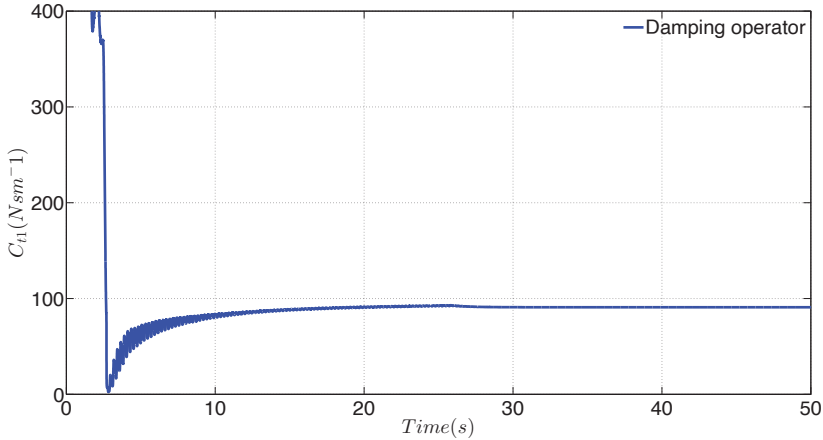
Figure 4.14: Viscous damping coefficient of the first storey of the setup.

Whereas the above procedure results in a stable prediction of the viscous damping coefficient, it does not prove that the viscous damping mechanism assumed in the evaluations is the true dissipation mechanism [47]. Therefore, it seems reasonable to refer to C_{tj} as effective viscous damping coefficients.

MODAL DAMPING MATRIX BASED ON IDENTIFIED DAMPING COEFFICIENTS

The procedure described above enables us to calculate the energy dissipated locally in the structural joints. The identified local damping can be formulated in terms of the modal damping matrix. To this end, the following procedure is used. First, the beam displacement is represented as a superposition of the modes of the undamped structure.

$$w(x, t) = \sum_{n=1}^{N} \phi_n(x)\psi_n(t) \tag{4.39}$$

Then, Eq. 4.39 is substituted in the equation of motion, given by Eq. 4.29. Multiplication of the resulting equation by the eigenvector, $\phi_m(x)$, followed by integration over the length of the beam, yields

$$\hat{\mathbf{L}}w(x,t) = -\sum_{j=1}^{N_{\text{storeys}}} 2C_{t_j} \int_0^{H+h} \phi_m(x) \left\{ \sum_{n=1}^{N} \delta\left(x - x_j - \Delta L\right) \right.$$
$$\left. \left(\phi_n(x) - \phi_n(x_j)\right) + \delta\left(x - x_j + \Delta L\right)\left(\phi_n(x) - \phi_n(x_j)\right)\right\} \dot{\psi}_n(t) dx =$$
$$-\sum_{j=1}^{N_{\text{storeys}}} 2C_{t_j} \left\{ \phi_m(x_j - \Delta L)(\phi_n(x_j - \Delta L) - \phi_n(\Delta x_j)) + \right.$$
$$\phi_m(x_j + \Delta L)(\phi_n(x_j + \Delta L) - \phi_n(x_j))\right\} \dot{\psi}_n(t) \tag{4.40}$$

where $\hat{\mathbf{L}}$ is an operator describing the elastic and inertial properties of the system. The inertial properties are represented by the mass matrix, $\mathbf{M}$, and the elastic properties are represented by the identified stiffness matrix, $\mathbf{K}$. Applying the Taylor expansion to the right-hand side of Eq. 4.40 and truncating the result to the first order, we obtain

$$\hat{\mathbf{L}}w(x,t) = -\sum_{j=1}^{N_{\text{storeys}}} 2C_{t_j} \Delta L^2 \phi_m'(x_j) \phi_n'(x_j) \dot{\psi}_n(t) \tag{4.41}$$

The equation above can be recast in the matrix form as

$$\mathbf{M}^* \ddot{\mathbf{u}}(t) + \mathbf{C}^* \dot{\mathbf{u}}(t) + \mathbf{K}^* \mathbf{u}(t) = \mathbf{0} \tag{4.42}$$

with, $\mathbf{M}^* = \boldsymbol{\phi}^T \mathbf{M} \boldsymbol{\phi}$, $\mathbf{K}^* = \boldsymbol{\phi}^T \mathbf{K} \boldsymbol{\phi}$, where,

$$\mathbf{C}^* = \sum_{j=1}^{N_{\text{storeys}}} 2C_{t_j} \Delta L^2 \phi_m'(x_j) \phi_n'(x_j) \tag{4.43}$$

The modal damping matrix, $\mathbf{C}^*$, is a fully populated, positive-definite $5x5$ matrix.

4.2.4. 5-DoF MODEL
To validate the damping obtained from the identification procedure described above, an effective 5-DoF system is used. Results are compared with measurements. Model predictions and measurements are compared, both in time and frequency domains, for an impact hammer test. The model is formulated as follows:

$$\mathbf{M}\ddot{\mathbf{x}}(t) + \mathbf{C}\dot{\mathbf{x}}(t) + \mathbf{K}\mathbf{x}(t) = \mathbf{F}(t) \tag{4.44}$$

By applying the modal decomposition, given by Eq. 4.26, we obtain the following equation:

$$\mathbf{M}^* \ddot{\mathbf{u}}(t) + \mathbf{C}^* \dot{\mathbf{u}}(t) + \mathbf{K}^* \mathbf{u}(t) = \mathbf{F}^*(t) \tag{4.45}$$

The left-hand side of this equation is the same as Eq. 4.42, whereas $\mathbf{F}^*(t) = \boldsymbol{\phi}^T \mathbf{F}(t)$.
To solve Eq. 4.45, it is customary to reformulate the equations of motion in the state-space form. This is done by introducing a new variable: modal velocity.

$$\dot{\mathbf{u}}(t) = \mathbf{v}(t) \tag{4.46}$$

By using Eq. 4.46, Eq. 4.45 takes the following form:

$$\dot{\mathbf{v}}(t) = \mathbf{M}^{*^{-1}} \left\{ \mathbf{F}^*(t) - \mathbf{C}^* \mathbf{v}(t) - \mathbf{K}^* \mathbf{v}(t) \right\} \tag{4.47}$$

where

$$\mathbf{v}(t) = \{\mathbf{u}(t); \dot{\mathbf{u}}(t)\} \tag{4.48}$$

which can be solved using a standard solver for a system of first-order ordinary differential equations.

4.2.5. RESULTS
In this section the proposed method for damping identification is validated. This was done by comparing the numerical results obtained by numerical integration of Eq. 4.47 with the data acquired using the first instrumentation configuration in the lab-scale structure, described in Fig. 4.7. The comparison was carried out both in time and frequency domains. The structure was excited by an external force, $\mathbf{F}(t)$, at the top floor, corresponding to the top mass of the 5-DoF model, using of an impact hammer. The resultant force of the impact measured at the tip of the hammer is shown in Fig. 4.15.
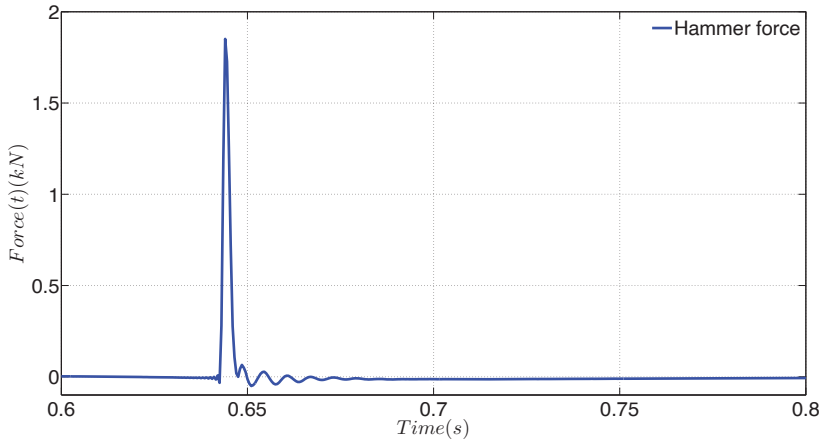
Figure 4.15: Hammer-impact force measured at the tip of the hammer as a function of time.

The first method validation is made by comparing the measured displacement of the structure at the top floor with the modelling output as shown in Fig. 4.16. To have a clearer view of the comparison a high-pass filter (100 Hz) is applied to the experimental data, because only the lowest five modes are included in the model. Therefore, high frequencies that can be captured by the measurement device cannot be predicted by the model.
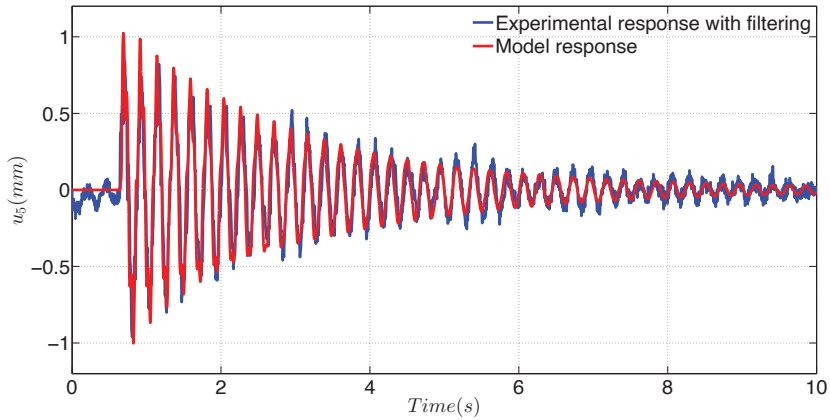
Figure 4.16: Filtered response to a hammer impact at the top storey of the setup and the model in time domain.

In Fig. 4.16, the experimentally observed response and the model are in good agreement up to 3 s. Then, a small deviation of the experimental data, compared to the simulation, is observed. This is the result of interference with another closely-spaced mode. Figure 4.17 presents the results of the experimental data and the model output, computed via FFT of the time signal, as shown in Fig. 4.16.
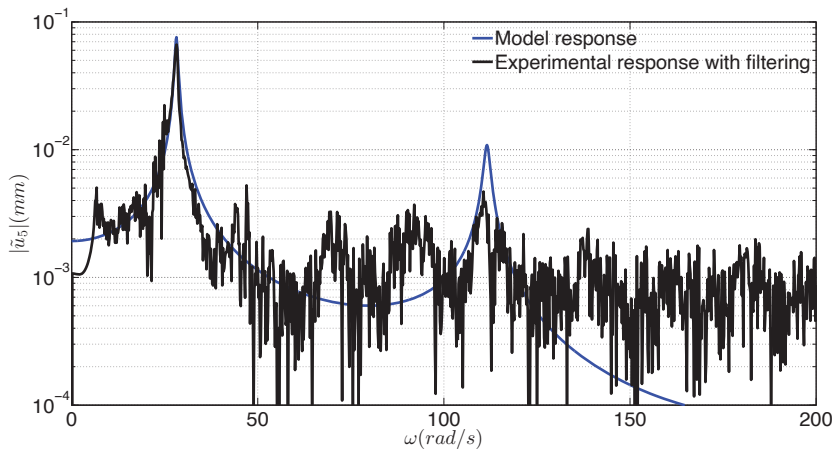
Figure 4.17: A absolute value of the displacement frequency response to a hammer impact at the top storey of the experimental setup and the numerical model.

Whereas the results are in good agreement up to about 50 rad/s, no correspondence is observed at higher frequencies. This is because that the displacement sensor captures

only the fundamental mode of the structure. To validate and study the accuracy of the presented method for higher frequencies, the acceleration measurements must be transformed to the frequency domain and compared with the modelling results. Figure 4.18 shows the spectra of the modelled and measured accelerations.
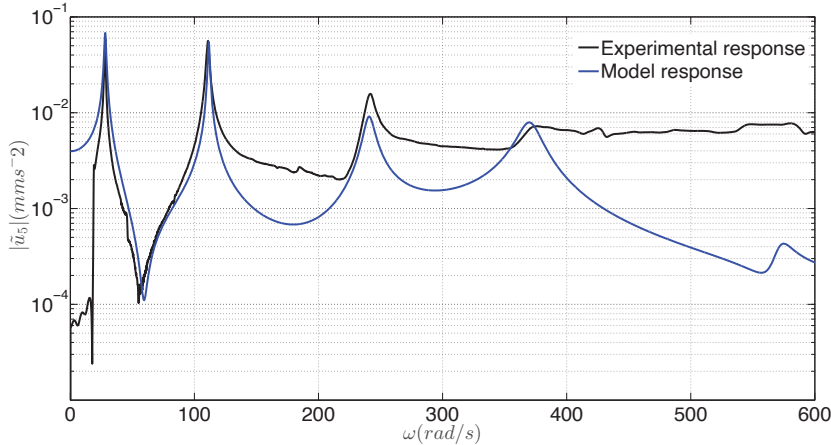
Figure 4.18: A absolute value of the acceleration frequency response to a hammer impact at the top storey of the experimental setup and the numerical model.

The model predictions are in excellent agreement with the measurements for the first and second modes. A good agreement is also observed for the third mode and a reasonable approximation is observed for the fourth mode. The higher modes contain very little energy in the experiments, leading to an expected worsening of the correspondence between measurements and predictions. The results presented in this section provide a satisfactory validation for the damping identification method.

4.3. CONCLUDING REMARKS

In this chapter, a method was proposed to identify the local energy dissipation in structures. The method was based on the analysis of the energy flux across the boundaries of the local area, in which the damping was identified. This method was applied to a lab-scale beam and a lab-scale steel frame structure, aiming to identifying damping in a localized area of the structure.

According to the energy variation equation, the total energy in a local area of the structure can change due to the energy flux through the boundaries and the energy dissipation.

For the lab-scale beam, the energy dissipation is computed for the beam, given that the system is uniform, and that there are no other structural elements connected to the beam that can be a source of energy dissipation.

In the lab-scale building structure, the energy method helped quantify the local energy dissipation near the joints of the 5-storey model by means of an equivalent vis-

cous damping element. This can be accounted for in a global damping matrix. Then, a modal damping matrix was formulated for the 5-storey structure, which was shown to fully-populate off-diagonal entries. This provided insight on the energy dissipation, owing to the interactions between modes. To validate this method, the experimentally measured responses to a hammer-impact test was compared to predictions. Their effective viscous damping was identified using the proposed method. The agreement of the time response signals and their spectra was found to be good, especially for the lower frequencies. Thus, the proposed method provides a solid framework for identification of local damping in complex structures.

4

5

ENERGY-FLUX ANALYSIS AS A TOOL FOR IDENTIFYING THE CONTRIBUTION OF SOIL-STRUCTURE INTERACTION TO DAMPING IN TALL BUILDINGS

The aim of this chapter is to independently identify the energy dissipation in the super-structure and the SSI of a tall building. To this end, the method based on energy-flux analysis that is described in the previous Chapter is used. Identifying the energy dissipation at selected areas of a building is important for improving the dynamic performance of tall buildings during the design stage. In this chapter, energy-flux analysis is used for damping identification in a high-rise building in The Netherlands (i.e. JuBi tower). First, an extensive experimental campaign was conducted. The collected data were used for standard experimental identification of the natural frequencies and equivalent damping values for comparison later. Then, the energy-flux analysis was carried out to ensure certain parts of the structure could be isolated, accounting for the energy exchanged with the adjacent parts of the building via the energy flux. Having computed the energy content of a specific part of a structure and the energy exchanged at the chosen boundaries, the energy dissipated within those boundaries could be computed. In this case, the energy dissipation in the superstructure and the foundation is identified separately. Damping operator constants are quantified and used for an analytical model to compare the experimentally identified damping values.

5. ENERGY-FLUX ANALYSIS AS A TOOL FOR IDENTIFYING THE CONTRIBUTION OF
SOIL-STRUCTURE INTERACTION TO DAMPING IN TALL BUILDINGS

78

5.1. FULL-SCALE MEASUREMENTS OF WIND-INDUCED VIBRA-TIONS

5.1.1. BUILDING DESCRIPTION: THE JUBI TOWER

The JuBi tower (Fig. 5.1) is a 146 m tall office building with 39 storeys, located in The Netherlands. The JuBi tower is a concrete tube-in-tube structure.

Figure 5.1: The JuBi tower

The horizontal stability of the building is provided by three internal concrete cores of a rectangular shape and the outside walls of an asymmetric shape. The storeys are separated by lightweight floors hinged to the outside walls and the internal cores. Therefore, the floors do not significantly contribute to the horizontal resistance of the building. Vertical loads on the floors are transferred to the cores and the outside walls, then directly to the foundation. The building is located on soft soil.

5.1.2. SOIL CONDITIONS

Prior to building construction, soil characteristics of the site were identified via cone penetration test (CPT) tests at several locations within the foundation boundaries [48].CPT employs a cone that penetrates the soil to measure resistance. Data recorded by means of the CPT test could not be directly used for calculations. However, shear-wave speed, which is a relevant parameter for computing soil resistance, could be calculated based on recorded data of the CPT test, making use of the most appropriate correlation [49–52]. The identification of the soil shear-wave speed helps us describe the characteristics of soil layers up to certain depth. This depth usually extends to at least the foundation pile length. Thus, the soil-foundation resistance can be identified.

At the location of the JuBi tower, several CPT tests were performed. The shear-wave speeds identified by means of Robertson's correlation [52] from these measurements are depicted in Fig. 5.2. Looking at Fig. 5.2 three distinct soil layers can be identified, and
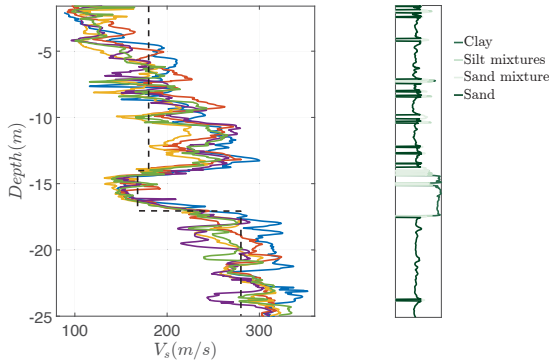
Figure 5.2: The soil shear-wave speed at the location of the JuBi tower

the mean shear-wave speed at each layer is plotted (black-dashed line). Moreover, the shear-wave speed is relatively low. This is rather common for soft-soil conditions found in The Netherlands.

5.1.3. INSTRUMENTATION AND FIELD MEASUREMENTS

Acceleration and strain measurements were conducted in the JuBi tower under strong wind conditions, as shown in Fig. 5.3. Accelerations at the 9th, 22nd and 37th floors and strains at the 9th floor were recorded during 2 hours. Figure 5.3 shows the measurement strategy used during the measurement campaign. This instrumentation strategy is chosen to collect the information needed for the energy-flux analysis.
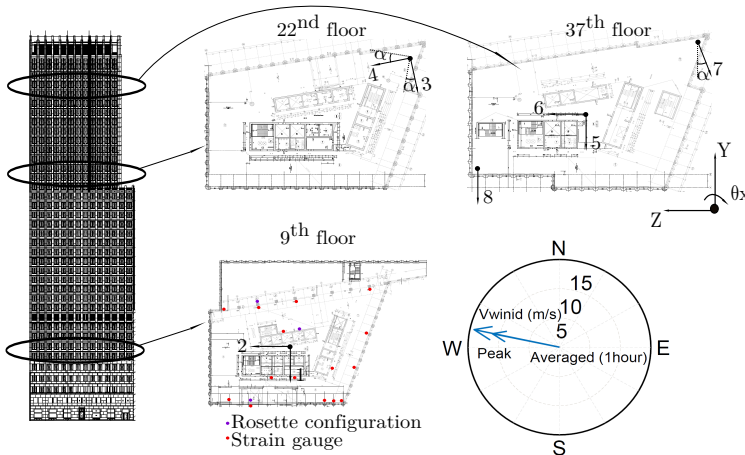
Figure 5.3: Instrumentation configuration at the 9th, 22nd and 37th floors

5. ENERGY-FLUX ANALYSIS AS A TOOL FOR IDENTIFYING THE CONTRIBUTION OF
SOIL-STRUCTURE INTERACTION TO DAMPING IN TALL BUILDINGS

80

The 37th floor is instrumented with four accelerometers. Accelerometers 5, 7 and 8 are placed such that accelerations in the weak direction (Y-direction) are registered. Accelerometer 6 is placed 90° with respect to accelerometer 5 to measure accelerations in the stiff direction (Z-direction). Making use of accelerometers 5 and 8, torsional motion can be measured. This instrumentation disposition also allows us to identify the global fundamental modes in the weak and stiff translational directions and the torsional direction of the building structure. At the 22nd floor, accelerometers 3 and 4 were placed perpendicular to each other to measure accelerations in the weak and stiff translational directions. At the 9th floor, strains and accelerations were measured. Accelerometers 1 and 2, shown in Fig. 5.3, are placed using the same strategy used to instrument the other floors. On the same floor, 24 strain gauges were mounted on various components (e.g. cores, piles, and outside walls) to map the strain distribution. Several strain gauges are installed on different components in a rosette shape. The data acquisition (DAQ) system and instrumentation used during the measurements are described in Table 5.1.

Equipment	Model	Software and Characteristics
DAQ 9th floor	HBM-MGCplus(MGC5)	Catman 4.0.3
DAQ 22nd floor 37th floor	Dewetron DEWE-50-USB-8	Dewesoft 7.1.1
Accelerometers	Sundstrand QA-700 (x8)	Sampling frequency 100 Hz Range $\pm 10mV/V$ and $20m/s$ Voutput=9.81 V Amplifier: DAQP STG Filter Butterworth: 10 Hz Sensitivity $30g/N$
Strain gauges	Tokyio Sokki PL-60-11 (x24)	Sampling frequency 100 Hz Range $2000mV/V$ Resistance $120 \pm 0.3\Omega$ Amplifier: ML801 Filter Butterworth: 10 Hz Half bridge Bridge factor 1 Gauge factor 2.13

Table 5.1: DAQ and instrumentation description

Acceleration and strain data were recorded in sub-samples of 10 min. After some data processing, time traces of each accelerometer were transformed to the frequency domain for identification purposes.

The PSD of the velocity is shown in Fig. 5.4. To obtain velocity signals, the acceleration is integrated numerically, and the mean value of the resulting dependence of the velocity on time is set to zero. The figure shows that all accelerometers recorded signals at all resonance frequencies. This means that the directional placement of accelerometers does not correspond to the principal directions of the modal vibrations. This is prohibitive
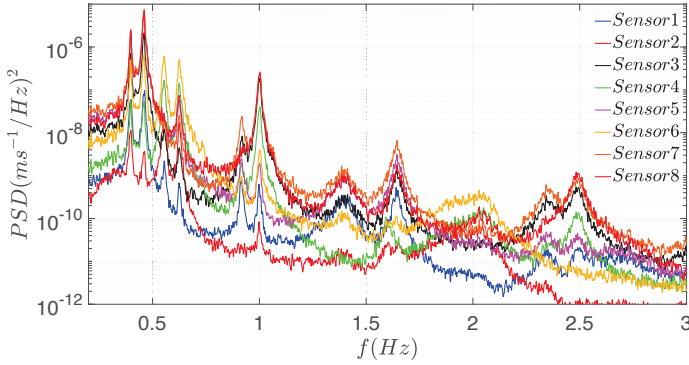
Figure 5.4: The PSD functions at the 9th, 22nd and 37th floors

for direct identification of the modal damping. To mitigate this, the acceleration signals were manipulated by making use of rigid-body kinematics, as described in Eq. 5.1:

$$\vec{v}_{\text{B}} = \vec{v}_{\text{A}} + \vec{\Omega} \times \vec{r}_{\text{A}}^{\text{B}} \tag{5.1}$$

Assuming that each floor behaves as a rigid body (See Section 5.5), the velocity at any point, $\vec{v}_{\text{B}}$, can be computed as the velocity at a certain point, $\vec{v}_{\text{A}}$, plus the angular velocity, $\vec{\Omega}$, times the distance between A and B. By means of Eq. 5.1, single-mode signals can be computed, as shown in Fig. 5.5.
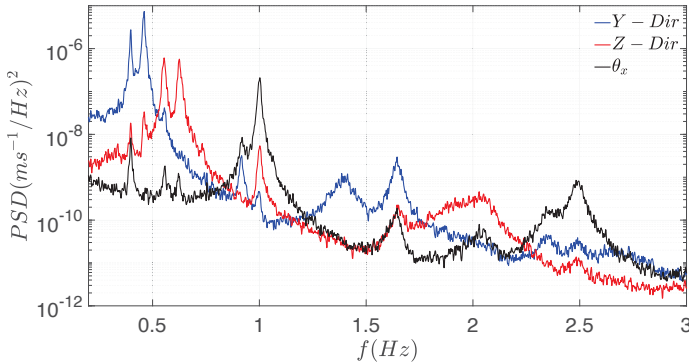
Figure 5.5: Power-spectral density functions of the shifted signals at the 37th floor

Once the modes are separated, SDoF-based identification techniques can be applied to the signals. Looking at Fig. 5.5, the spectral density functions of the translational signals (red and blue lines) show double peaks. It is tempting to conclude that these peaks correspond to two distinct global modes, which correspond to specific vibrational

shapes of the building. This is not the case, however. The true reason for these peaks is that the JuBi tower consists of three cores and outer walls, which have close natural frequencies, as deduced from the strain measurement data. The cores and walls are coupled by the floors, but only weakly. Therefore, the two closely spaced peaks shown in Fig. 5.5 correspond to the slightly modified natural frequencies of the cores and the walls.

In this work, HPBW [53] is applied to the data shown in Fig. 5.5 to identify the fundamental frequencies, f_n, and the corresponding equivalent viscous damping ratios, ξ_n, for the three fundamental modes of the building (i.e. two translational and one rotational around the vertical axis).

Because JuBi tower has two closely spaced resonant frequencies, using the HPBW method for damping identification is not straightforward. Therefore, given that these two resonant frequencies correspond to the components of a weakly coupled system, an equivalent viscous damping ratio at each peak was identified and averaged. For the torsional mode, no such behaviour is identified. Consequently, the HPBW method can be directly applied to the latter. It should be noted that the experimentally identified equivalent viscous damping ratios were not true damping values for the assumed real-valued modes, given the fact that these modes are coupled. However, in this work, the HPBW method is used to indicate the effective damping ratio, used for comparing the damping values identified by the energy-flux method. The averaged damping ratios identified with the HPBW method are presented in Table 5.3.
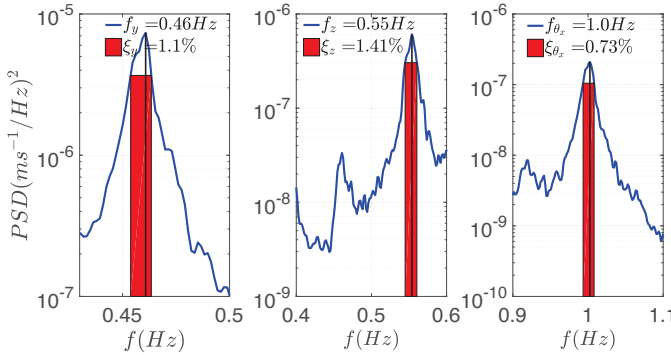
Figure 5.6: HPBW method applied to the shifted signals at the 37th floor

Figure 5.6 shows the damping identified by the HPBW method at one of the peaks of the two translational PSD functions and the torsional one. The equivalent viscous damping in each peak is computed by the following expression.

$$2\xi = \frac{\Delta f}{f_n}$$
(5.2)

Where f_n accounts for the fundamental frequency, and Δf accounts for the frequency distance at half of the height of the spike.

5.2. MODEL AND ENERGY-FLUX ANALYSIS

Energy-flux analysis is used in this work to identify the energy dissipated in a full-scale structure. During vibrations of a high-rise building, not only does the part of the structure above-ground (superstructure) move, the surrounding soil and the foundation also moves. This shows that energy is dissipated in the superstructure and the foundation, owing to the interaction with the soil [33]. The SSI is rather complex and uncertain [54–56]. Whereas the SSI is a process taking place beneath the ground, the superstructure can strongly influence the SSI effects and vice versa. Modelling the dynamic SSI for high-rise buildings is a challenge, owing to uncertainties in the characteristic of the soil and the complexity of the foundation. Especially challenging is predicting the dissipative properties of the building structure and the SSI-associated damping. Therefore, in this work, a novel method for damping identification, based on energy-flux analysis, is used to identify the dissipative properties of a full-scale high-rise building. Additionally, an attempt is made to identify the energy dissipated in the superstructure separately from that dissipated in the soil-foundation interaction.

5.2.1. BEAM MODEL AND ENERGY-FLUX ANALYSIS

To study the energy dissipated in the JuBi tower from wind loads via energy-flux analysis, a Euler–Bernoulli beam model is adopted. The tower is sketched in Fig. 5.7. Its stability is assured by three concrete cores and the outer walls, as shown in Fig. 5.7.

The structure has a complex and asymmetric shape. With the random load distribution from the wind gusts, it is reasonable to assume that, during vibration, the building performs both translational and torsional (coupled) vibrations. To account for these motions and their coupling in a relatively simple manner, an appropriate beam model is developed, as described below.

It is assumed that the cross-section perpendicular to the largest dimension of the beam (building) remains a plane after deformation. This means that the cross-section of the beam moves as a rigid body and is uniquely described by a position vector $\mathbf{w} = [w_x \ \ w_y \ \ w_z]$ and a rotation vector, $\theta = [\theta_x \ \ \theta_y \ \ \theta_z]$, where x, y and z are the components of the coordinate system. Furthermore, geometric linearity is assumed, implying the angles of rotation are small. Next, referencing a material point in the cross-section, a displacement vector, $\mathbf{u} = \mathbf{u}(x, y, z, t)$, with components u_x, u_y and u_z, is described as follows:

$$
\begin{aligned}
u_x(x, y, z, t) &= w_x(x, t) + z\theta_y(x, t) - y\theta_z(x, t) \\
u_y(x, y, z, t) &= w_y(x, t) - z\theta_x(x, t) \\
u_z(x, y, z, t) &= w_z(x, t) + y\theta_x(x, t).
\end{aligned}
\tag{5.3}
$$

The corresponding strain components read,

$$
\epsilon_{xx} = \frac{\partial u_x}{\partial x}; \qquad \gamma_{xy} = \frac{\partial u_x}{\partial y} + \frac{\partial u_y}{\partial x}; \qquad \gamma_{xz} = \frac{\partial u_x}{\partial z} + \frac{\partial u_z}{\partial x}.
\tag{5.4}
$$

The equations of motion are formulated employing Lagrangian formalism. In general, the Lagrangian of a conservative system reads,
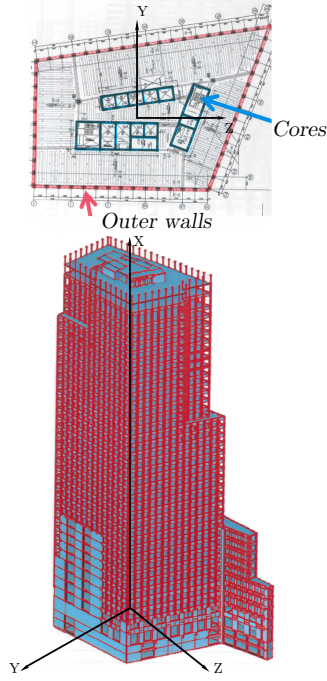
Figure 5.7: Layout of the stability cores and walls of the JuBi tower

$$\mathscr{L} = \mathscr{K} - \mathscr{V} \tag{5.5}$$

where $\mathscr{K} = \int_0^L K(\dot{u}, \dot{u}')\mathrm{d}x$ and $\mathscr{V} = \int_0^L V(u, u', u'')\mathrm{d}x$ are the kinetic and potential energies respectively. Therefore, the Lagrangian density function can be express in a general manner as $\lambda = \lambda(u, u', u'', \dot{u}, \dot{u}')$, where the Lagrangian reads as

$$\mathscr{L} = \int_0^L \lambda(x, t)\mathrm{d}x =$$
$$\int_0^L \left\{ \left(\frac{1}{2}\rho A \left(\left(\dot{w}_x(x, t) + z\dot{\theta}_y(x, t) - y\dot{\theta}_z(x, t) \right)^2 + \left(\dot{w}_y(x, t) - z\dot{\theta}_x(x, t) \right)^2 + \right. \right.$$
$$\left(\dot{w}_z(x, t) + y\dot{\theta}_x(x, t) \right)^2 \right) \right) - \left(-T(x)w_x'^2 + \frac{1}{2}E(x)\left(Aw_x''^2(x, t) \right. \right.$$
$$-2S_y w_x'(x, t)w_z''(x, t) - 2S_z w_x'(x, t)w_y''(x, t) + 2S_\omega w_x'(x, t)\theta_x''(x, t)$$
$$+I_{yy}w_z''^2(x, t) + 2I_{yz}w_z''(x, t)w_y''(x, t) - 2I_{z\omega}w_z''(x, t)\theta_x''(x, t)+$$
$$I_{zz}w_y''^2(x, t) - 2I_{y\omega}w_y''(x, t)\theta_x''(x, t) + I_\omega\theta_x''^2(x, t) \right) + \frac{1}{2}G(x)K\theta_x'^2(x, t) \right) \right\}\mathrm{d}x. \tag{5.6}$$

The Euler-Lagrange equation for one-dimensional systems can be described in its general form as follows:

$$\frac{\partial \lambda}{\partial u_i} - \frac{\partial}{\partial t}\frac{\partial \lambda}{\partial \dot{u}_i} + \frac{\partial}{\partial x}\frac{\partial \lambda}{\partial u_i'} + \frac{\partial^2}{\partial x^2}\frac{\partial \lambda}{\partial u_i''} + \frac{\partial^2}{\partial t \partial x}\frac{\partial \lambda}{\partial \dot{u}_i \partial u_i'} + \overline{Q} = 0. \tag{5.7}$$

Where u_i denotes the generalized coordinate at each direction: $i = x, y$ and z. Next, substituting the Lagrangian function described in Eq. 5.6 into the Euler-Lagrange equation, Eq. 5.7, equations of motion governing small vibrations of the coupled system represented in Fig. 5.7 are obtained as

$$\left(\sum_{j=1}^{N_{\text{floors}}} \frac{M_j}{L} + \sum_{k=1}^{N_{\text{cores}}} \rho_k A_k\right)\left(\ddot{w}_y(x,t) - z\ddot{\theta}_x(x,t)\right) +$$

$$\sum_{k=1}^{N_{\text{cores}}} T_k(x)w_y''(x,t) - ES_z^k w_x'''(x,t) + EI_{yz}^k w_z''''(x,t) + EI_{zz}^k w_y''''(x,t) = F_y(x,t) \tag{5.8}$$

$$\left(\sum_{j=1}^{N_{\text{floors}}} \frac{M_j}{L} + \sum_{k=1}^{N_{\text{cores}}} \rho_k A_k\right)\left(\ddot{w}_z(x,t) + y\ddot{\theta}_x(x,t)\right) +$$

$$\sum_{k=1}^{N_{\text{cores}}} T_k(x)w_z''(x,t) - ES_y^k w_x'''(x,t) + EI_{zy}^k w_y''''(x,t) + EI_{yy}^k w_z''''(x,t) = F_z(x,t) \tag{5.9}$$

$$\left(\sum_{j=1}^{N_{\text{floors}}} \frac{M_j}{L} + \sum_{k=1}^{N_{\text{cores}}} \rho_k I_p^k\right)\ddot{\theta}_x(x,t) + \sum_{k=1}^{N_{\text{cores}}} \rho_k A_k\left(y\ddot{w}_z(x,t) - z\ddot{w}_y(x,t)\right) + G_k K_k \theta_x''(x,t) = F_x(x,t) \tag{5.10}$$

where

$$T_k(x) = \rho A g x. \tag{5.11}$$

Equation 5.8 describes the equilibrium in the Y-direction (weak direction); Eq. 5.9 represents the equilibrium in Z-direction (stiff direction) and Eq. 5.10 describes the dynamic torque about the X-axis.

Lagrangian formalism can also be used to formulate the energy-balance equation, which has the following form:

$$\frac{\mathrm{d}}{\mathrm{d}t}E(t) + S(x,t)\big|_{L_{\text{initial}}}^{L_{\text{final}}} = W_{\text{ext}}(t) - W_{\text{diss}}(t) \tag{5.12}$$

where $E(t)$ is the energy change obtained by the summation of kinetic and potential energies, described in Eqs. 5.13-5.14,

$$\mathcal{K} = \frac{1}{2}\int_L \left\{\rho \int_A \left(\dot{u}_x^2 + \dot{u}_y^2 + \dot{u}_z^2\right)dA\right\}\mathrm{d}x \tag{5.13}$$

and,

$$\mathcal{V} = \frac{1}{2}\int_L \left\{ E\int_A \epsilon_{xx}^2 dA \right\} dx + \frac{1}{2}\int_L \left\{ G\int_A \left(\gamma_{xy}^2 + \gamma_{xz}^2 \right) dA \right\} dx \tag{5.14}$$

S is the energy flux at specific boundaries, L_{final} and L_{initial}. The energy flux is computed by means of Eq. 5.15.

$$S(x,t) = \left(\frac{\partial u_i}{\partial t}, \frac{\partial \lambda}{\partial u_i'} - \frac{\partial}{\partial x}\frac{\partial \lambda}{\partial u_i''} - \frac{\partial}{\partial t}\frac{\partial \lambda}{\partial u_i' \partial \dot{u}_i} \right) + \left(\frac{\partial^2 u_i}{\partial x \partial t}, \frac{\partial \lambda}{\partial u_i''} \right) \tag{5.15}$$

The W_{diss} is the rate of energy dissipated within the boundaries (L_{initial} to L_{final}), and W_{ext} is the rate of energy introduced to the system by external forces. Equation 5.12 shows that the energy change in the system is balanced by (i) the energy flux, S, through specific boundaries, (ii) the energy dissipated, W_{diss}, and (iii) the external effects, W_{ext}. Next, the Fourier transform pair is introduced as:

$$\tilde{F}_n(\omega) = \mathcal{F}(f_n(t)) = \int_{-\infty}^{\infty} f_n(t)e^{-i\omega t}dt \quad \text{and} \quad f_n(t) = \mathcal{F}^{-1}(\tilde{F}_n(\omega)) = \frac{1}{2\pi}\int_{-\infty}^{\infty} \tilde{F}_n(\omega)e^{i\omega t}d\omega. \tag{5.16}$$

The energy balance equation, Eq. 5.12, of a time interval $[t; t+T]$ is transformed into the frequency domain, as shown in Eq. 5.17.

$$\int_{-\infty}^{\infty} \left\{ E(\tilde{t})|_t^{t+T} + \int_t^{t+T} S(x,\tilde{t})|_{L_{\text{initial}}}^{L_{\text{final}}} d\tilde{t} \right\} e^{-i\omega t} dt =$$
$$\int_{-\infty}^{\infty} \left\{ \int_t^{t+T} W_{\text{ext}}(\tilde{t})d\tilde{t} - \int_t^{t+T} W_{\text{diss}}(\tilde{t})d\tilde{t} \right\} e^{-i\omega t} dt \tag{5.17}$$

Where the energy change, $E(\tilde{t})$, and the energy flux, $S(x,\tilde{t})$, are first numerically integrated over a time span, $[t; t+T]$ and are then transformed to the frequency domain using FFT.

5.2.2. Energy dissipation in the superstructure of the JuBi tower subject to wind

In this section, Eq. 5.17 and the data recorded during the measurement campaign are used to identify the energy dissipation in the structure. As described in Section 5.1, measurements were performed at three levels of the building. To compute the energy dissipated in the superstructure, data recorded at the top level, L_f (37th floor) and at the bottom level, L_l (9th floor) with the energy balance equation are used. The energy-change term in Eq. 5.17 is computed using the following formula:

$$E(\tilde{t})|_t^{t+T} = \frac{(L_f - L_l)}{2} \left(\tilde{e}_l(\tilde{t}) + \tilde{e}_f(\tilde{t}) \right)|_t^{t+T} \tag{5.18}$$

where $\tilde{e}_l(\tilde{t})$ is the energy density computed at the bottom of the superstructure, and $\tilde{e}_f(\tilde{t})$ is the energy density at the top measurement location. At the top level, the kinetic energy is computed per Eq. 5.13 and using the accelerometer data. It is assumed that the

elastic energy density and the energy flux atop the building are negligible compared to the kinetic energy. Thus, the top level is characterized solely by the kinetic energy. At the bottom, the kinetic and elastic energies are computed per Eq. 5.13 and Eq. 5.14 using the recorded strain and acceleration data. Several strain gauges were glued around each core and outer walls of the building. Thus, elastic energy is computed at each core and outer wall, and added together. The energy flux crossing the bottom level, L_l is also computed. This concludes the quantification of the left-hand side of Eq. 5.17.

To obtain the energy dissipated in the system, W_{diss}, from the energy balance, it remains to estimate the energy, W_{ext}, introduced to the building by the wind. During the measurement campaign, no wind sensors were installed on the building and, therefore, this data was not explicitly collected. However, the wind peak velocity and 1-hr average velocity (Fig. 5.3) could be obtained in The Netherlands via the KNMI database. Using this data with a well-established procedure, a realistic wind–energy spectrum could be computed, as described below.

First, the wind pressure, p_{wind}, caused by the wind velocity normal to the face, B, of the building, is computed. It is generally assumed that the wind velocity contains a mean component, $\overline{v}(x)$, and a fluctuating component, $\tilde{v}(x, t)$, both dependent on the height, x.

$$p_{\text{wind}}(x, t) = \frac{1}{2}\rho_w \left(\overline{v}(x) + \tilde{v}(x, t)\right)^2, \tag{5.19}$$

where ρ_w is the air density. The wind load-per-unit length of the building equals the wind pressure multiplied by the building width, B, and the shape factor, C_f.

$$q_{\text{wind}}(x, t) = \frac{1}{2}\rho_w B C_f \left(\overline{v}(x) + \tilde{v}(x, t)\right)^2 \tag{5.20}$$

Next, the rate of energy, $\Xi_{\text{ext}}(x, t)$, introduced to the unit length of the building by the wind, can be computed by multiplying the wind load, q_{wind}, by the velocity of the building. We assume that the wind blows in the weak direction (parallel to the y-axis) of the building. This results in the following expression for $\Xi_{\text{ext}}(x, t)$:

$$\Xi_{\text{ext}}(x, t) = \frac{1}{2}\rho_w C_f B \left(\overline{v}(x) + \tilde{v}(x, t)\right)^2 \dot{u}_y(x, t) \tag{5.21}$$

The fluctuating component of the wind velocity is significantly smaller than the mean velocity, and the velocity of the building is also much smaller than the mean wind velocity [20]. Therefore, we use the linearized version of Eq. 5.21:

$$\Xi_{\text{ext}}(x, t) = \frac{1}{2}\rho_w C_f B \overline{v}^2(x) \dot{u}_y(x, t) \tag{5.22}$$

The mean wind velocity is normally assumed to have a logarithmic variation along the building height. Therefore, according to Eurocode NEN-EN 1991-1-4, the mean wind velocity function can be described by the following expression:

$$\overline{v}(x) = 0.19 \left(\frac{x_0}{x_{0,II}}\right)^{0.07} \ln\left(\frac{x}{x_0}\right) v_{b,0}, \tag{5.23}$$

where $v_{b,0} = 27$ m/s is the mean wind speed; $x_{0,\text{II}} = 0.05$ is a parameter accounting for the location of the buildings, and $x_0 = 0.5$ accounts for the roughness of the terrain. To obtain the total rate of energy introduced by the wind, Eq. 5.22 is integrated over the length of the superstructure as follows:

$$W_{\text{ext}}(\tilde{t}) = \int_0^L \Xi_{\text{ext}}(x, t)\,dx = \frac{1}{2}\rho_{\text{w}}C_{\text{f}}B\int_0^L \dot{u}_y(x, t)\overline{v}^2(x)\,dx \qquad (5.24)$$

Given that the velocity of the building is known only at the measurement locations, a linear approximation of the building velocity is used: $\dot{u}_y(x, t) = \frac{\dot{u}_y(L_{\text{f}}, t) - \dot{u}_y(L_{\text{l}}, t)}{L_{\text{f}} - L_{\text{l}}}x + \dot{u}_y(L_{\text{l}}, t)$.

At this point, W_{diss}, which accounts for the rate of energy dissipated at the superstructure is the only unknown in the energy balance, equation, Eq. 5.12. Therefore, the energy dissipated, as a function of frequency, can be also computed in accordance with Eq. 5.17.

5.2.3. Energy dissipation in the soil-foundation interaction of the JuBi tower

To compute energy dissipation, owing to the SSI ($W_{\text{diss}}^{\text{SSI}}$), the recorded data at the bottom floor (9th floor) is used. Thus, the energy dissipation, $W_{\text{diss}}^{\text{SSI}}$, computed in this manner accounts for the dissipation in the soil-foundation and in the part of the superstructure between the foundation and the 9th floor. Ideally, to identify the energy dissipation solely in the foundation, measurements at ground level are desired. However, due to strict safety regulations, the 9th floor was the lowest level allowed for equipment installation. It is expected that, owing to the very high rigidity of the lower part of the building compared to soil stiffness, the energy dissipated between the 9th floor and the ground level is significantly smaller than the energy dissipated in the SSI and, therefore, the so-identified, $W_{\text{diss}}^{\text{SSI}}$, is representative for the dissipation in the soil-foundation interaction.

Given that there is only acceleration and strain data recorded at the 9th floor, some assumptions must be made to quantify the energy dissipation around the soil-foundation part. First, the lower part of the building, from the 9th floor to the ground, is assumed to move as a rigid body. Second, the complex interaction between the soil and the building foundation is simplified by means of springs, which represent the dynamic stiffness of the soil-foundation interaction for the different directions, as shown in Fig. 5.8.

(a) Sketch of the soil-foundation and lower part of the building

(b) Simplification of the soil foundation and lower part of the building by means of a beam model and springs
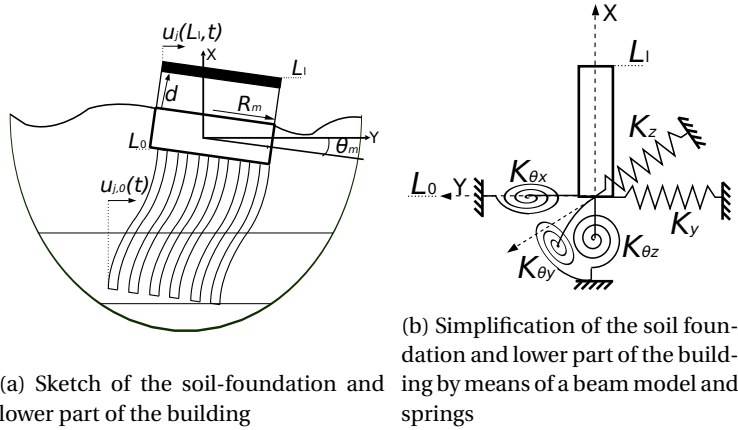
Figure 5.8: Description of the soil-foundation and lower part of the building

Considering the model sketched in Fig. 5.8b, the energy balance described in Eq. 5.12 can be used. $E(\tilde{t})|_t^{t+T}$ can be computed by means of the following equation:

$$E(\tilde{t})|_t^{t+T} = (L_l - L_0)\tilde{e}_l(\tilde{t})|_t^{t+T} \tag{5.25}$$

where $\tilde{e}_l(\tilde{t})$ was computed in the previous section. The energy flux, $S(L_1, \tilde{t})$, is computed by means of Eq. 5.15. $S(L_0, \tilde{t})$ is set to zero, given that the SSI is accounted for by the springs, as shown in Fig. 5.8b. The rate of elastic energy related to SSI can be computed as

$$W_{\text{ext}}(\tilde{t}) = K_y w_y(L_0, t)\dot{w}_y(L_0, t) + K_z w_z(L_0, t)\dot{w}_z(L_0, t)|_{L_0} +$$
$$K_{\theta_y}\theta_y(L_0, t)\dot{\theta}_y(L_0, t) + K_{\theta_z}\theta_z(L_0, t)\dot{\theta}_z(L_0, t) + K_{\theta_x}\theta_x(L_0, t)\dot{\theta}_x(L_0, t) \tag{5.26}$$

The stiffnesses K_y, K_z, K_{θ_y}, K_{θ_z} and K_{θ_x} are computed with the well-established software, Dynapile. Realistic stiffness values are computed by introducing the soil profile described in Fig. 5.2, the pile plan, and the pile characteristics.

Next, the energy balance equation, Eq. 5.17, contains only one unknown, the spectra of the energy dissipation: $\tilde{W}_{\text{diss}}(\omega) = \int_{-\infty}^{\infty}\int_t^{t+T} W_{\text{diss}}(\tilde{t})e^{-i\omega t} dt d\tilde{t}$, which can be computed.

5.3. QUANTIFICATION OF THE ENERGY DISSIPATION IN THE JUBI TOWER

Having computed all terms of Eq. 5.17, except the energy dissipation, $W_{\text{diss}}(\tilde{t})$, the spectra of the energy dissipation in the superstructure, $\tilde{W}_{\text{diss}}^{\text{structure}}(\omega)$, and in the SSI, $\tilde{W}_{\text{diss}}^{\text{SSI}}(\omega)$, can be calculated. The results of these calculations are plotted in Fig. 5.9.

Once the dissipated energy is identified, it is of interest to characterize the velocity dependence of the damping force that could cause the dissipation. Whereas a wide range of velocity-dependences can be derived, the three most widely used dependencies are
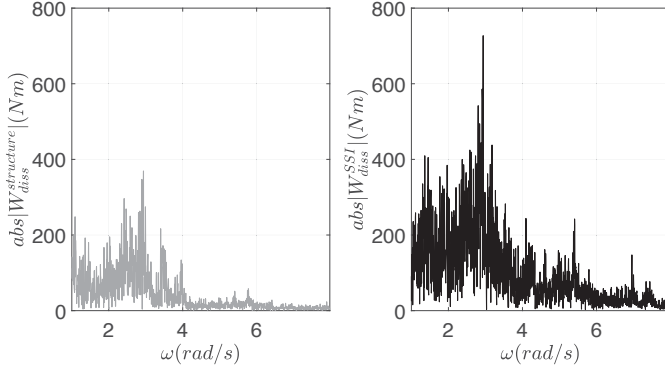
Figure 5.9: The amplitude spectra of the dissipated energy in the JuBi tower, subject to wind

considered (i.e. viscous type $\dot{u}(t)$, quadratic type $\dot{u}(t)|\dot{u}(t)|$ and hysteretic type $\frac{\dot{u}(t)}{|\dot{u}(t)|}$).
The damping mechanisms are described by the damping forces:

$$F_{D_1}(t,x) = \sum_{i=1}^{3} F_{D_1}^i(t,x) = \sum_{i=1}^{3} C_1^i \dot{u}_i(t,x) \tag{5.27}$$

$$F_{D_2}(t,x) = \sum_{i=1}^{3} F_{D_1}^i(t,x) + \sum_{i=1}^{3} F_{D_2}^i(t,x) = \sum_{i=1}^{3} C_1^i \dot{u}_i(t,x) + \sum_{i=1}^{3} C_2^i \dot{u}_i(t,x)|\dot{u}_i(t,x)| \tag{5.28}$$

$$F_{D_3}(t,x) = \sum_{i=1}^{3} F_{D_1}^i(t,x) + \sum_{i=1}^{3} F_{D_3}^i(t,x) = \sum_{i=1}^{3} C_1^i \dot{u}_i(t,x) + \sum_{i=1}^{3} C_3^i \frac{\dot{u}_i(t,x)}{|\dot{u}_i(t,x)|} \tag{5.29}$$

Where $F_{D_1}(t)$ is the linear damping force, $F_{D_2}(t)$ is the combination of the linear and
the quadratic damping forces and $F_{D_3}(t)$ is the combination of the linear and the hys-
teretic damping force. The rate of the dissipated energy associated with these damping
mechanisms can be written as

$$W_{\text{diss}_1}(t) = \sum_{i=1}^{3} \int_0^L F_{D_1}^i(t,x)\dot{u}_i(t,x)dx = \sum_{i=1}^{3} C_{1_i}^i \int_0^L \dot{u}_i^2(t,x)dx \tag{5.30}$$

$$W_{\text{diss}_2}(t) = \sum_{i=1}^{3} \int_0^L F_{D_1}^i(t,x)\dot{u}_i(t,x)dx + \sum_{i=1}^{3} \int_0^L F_{D_2}^i(t,x)\left(\dot{u}_i(t,x)|\dot{u}_i(t,x)|\right)dx =$$
$$\sum_{i=1}^{3} C_1^i \int_0^L \dot{u}_i^2(t,x)dx + \sum_{i=1}^{3} C_2^i \int_0^L \left(\dot{u}_i^2(t,x)|\dot{u}_i(t,x)|\right)dx \tag{5.31}$$

$$W_{\text{diss}_3}(t) = \sum_{i=1}^{3} \int_0^L F_{D_1}^i(t,x) \dot{u}_i(t,x) dx + \sum_{i=1}^{3} \int_0^L F_{D_3}^i(t,x) \left(\frac{\dot{u}_i(t,x)}{|\dot{u}_i(t,x)|} \right) dx =$$

$$\sum_{i=1}^{3} C_1^i \int_0^L \dot{u}_i^2(t,x) dx + \sum_{i=1}^{3} C_3^i \int_0^L \left(\frac{\dot{u}_i^2(t,x)}{|\dot{u}_i(t,x)|} \right) dx \qquad (5.32)$$

To obtain the velocity dependence associated with the rate of energy dissipation in the superstructure, the following linear relation between the velocities measured at the lowest and top measurement points is assumed: $\dot{u}_i(x,t) = \frac{\dot{u}_i(L_f,t) - \dot{u}_i(L_l,t)}{L_f - L_l} x + \dot{u}_i(L_l,t)$. Because there is no measurement data recorded at the foundation, it is assumed that the velocity over the lowest part of the structure is constant. The spectra of the dissipation energy, where $\mathscr{F}$ designates the integral Fourier transform as defined in Eq. 5.16, are

$$\mathscr{F}(W_{\text{diss}_1}(t)) = \sum_{i=1}^{3} C_1^i \mathscr{F} \left\{ \int_0^L \dot{u}_i^2(t,x) dx \right\} \qquad (5.33)$$

$$\mathscr{F}(W_{\text{diss}_2}(t)) = \sum_{i=1}^{3} C_1^i \mathscr{F} \left\{ \int_0^L \dot{u}_i^2(t,x) dx \right\} + \sum_{i=1}^{3} C_2^i \mathscr{F} \left\{ \int_0^L \dot{u}_i^2(t,x) |\dot{u}_i(t,x)| dx \right\} \qquad (5.34)$$

$$\mathscr{F}(W_{\text{diss}_3}(t)) = \sum_{i=1}^{3} C_1^i \mathscr{F} \left\{ \int_0^L \dot{u}_i^2(t,x) dx \right\} + \sum_{i=1}^{3} C_3^i \mathscr{F} \left\{ \int_0^L \frac{\dot{u}_i^2(t,x)}{|\dot{u}_i(t,x)|} dx \right\} \qquad (5.35)$$

The spectra of the dissipated energy defined in Eq. 5.17 are related to the spectra defined by Eqs. 5.33-5.35 as

$$\mathscr{F}\left(W_{\text{diss}_i}(t)\right) = A \tilde{W}_{\text{diss}}(\omega) \qquad (5.36)$$

where

$$A = \frac{2\pi\omega \mathrm{i}}{\left(e^{\mathrm{i}\omega T} - 1\right)}. \qquad (5.37)$$

is a frequency multiplier accounting for the finite duration, T, of the measurement. The damping operator constants, C_1^i, C_2^i and C_3^i for each vibrational direction can be estimated by means of minimization of the mismatch in Eq .5.36.

$$\min_{C_i} \sum_{\omega_n} \left| \tilde{W}_{\text{diss}}(\omega) - \mathscr{F}(W_{\text{diss}_i}(t)) \right| \qquad \text{where} \qquad \omega_n = \Delta\omega n \qquad (5.38)$$

Then, an estimate of the damping operator constant for the superstructure and the SSI associated to each vibration direction can be obtained. Using the damping constants obtained through the minimization procedure, the spectra of the dissipated energy corresponding to the three assumed dissipation forces can be obtained. These are shown in Figs. 5.10-5.15.

Figure 5.10: Comparison of linear damping to identify energy dissipation of the superstructure
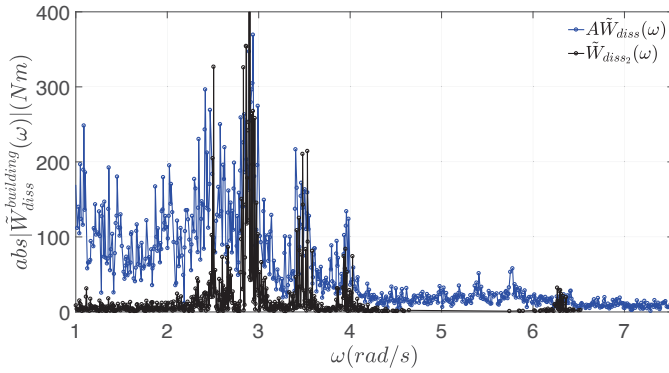
Figure 5.11: Comparison of quadratic damping to identify energy dissipation of the superstructure

Figures 5.10-5.15 show the local maxima of the spectra. The blue line represents the right-hand side of Eq. 5.36 and the black lines correspond to the energy dissipated predicted by the proposed damping mechanisms. Given the fact that C_1^i, C_2^i and C_3^i are assumed to be constant, the minimization procedure focuses on minimizing the error at the maxima of the spectra, corresponding to the natural frequencies of the building within the measured frequency band. The energy dissipation, $\tilde{W}_{\text{diss}1}$, which corresponds to the energy dissipated obtained from linear damping, gives a reasonable approximation at the modal frequencies of the building. The energy dissipation predicted by the quadratic damping, $\tilde{W}_{\text{diss}2}$, gives less-accurate agreement at the natural frequencies. In this case study, the non-linearity of the damping is not highly influential, given the velocities are not large. The hysteretic damping mechanism, $\tilde{W}_{\text{diss}3}$, is the most sensitive to changes in values of the constant. Therefore, the linear viscous damping force with the corresponding constants, identified by means of the minimization will be used in the
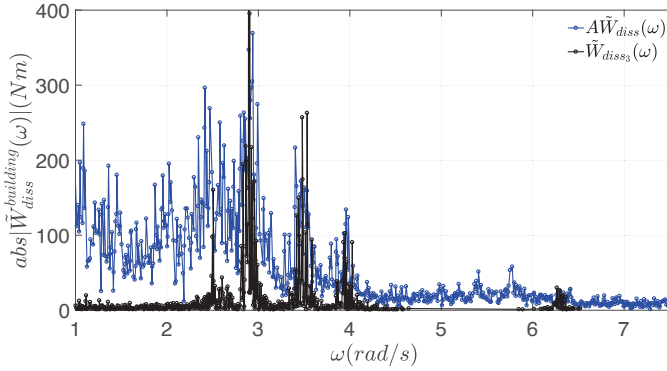
Figure 5.12: Comparison of hysteretic damping to identify energy dissipation of the superstructure
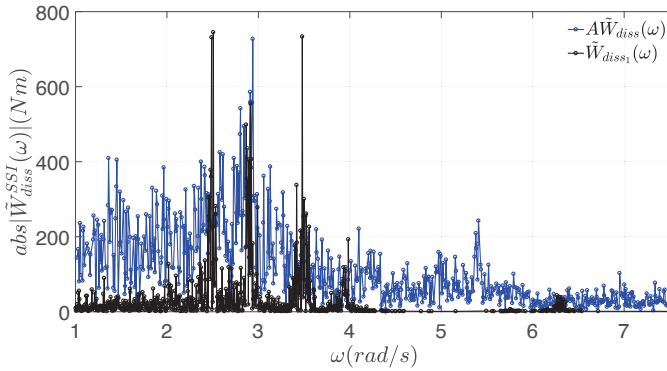
Figure 5.13: Comparison of linear damping to identify energy dissipation of the SSI

next section.

5.4. COMPARISON OF THE DAMPING IDENTIFIED BY MEANS OF THE ENERGY-FLUX ANALYSIS AND THE MEASURED MODAL DAMPING

To validate the proposed energy method for damping identification, the equivalent damping ratios, identified by HPBW, are compared to the computed modal damping ratios using the damping operators identified by the energy-flux analysis. To this end, the model depicted in Fig. 5.16 is used. Equations of motion are given by Eqs. 5.8-5.10, assuming the cross-coupling terms are negligible for simplification. The boundary conditions are adopted from the foundation simplification depicted in Fig. 5.8, and C_{θ_m}, C_{θ_x}, $C_{\theta_m}^{\mathrm{SSI}}$ and

94

5. Energy-flux analysis as a tool for identifying the contribution of soil-structure interaction to damping in tall buildings
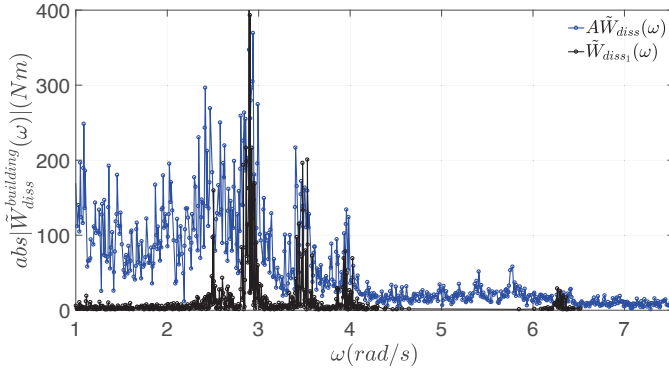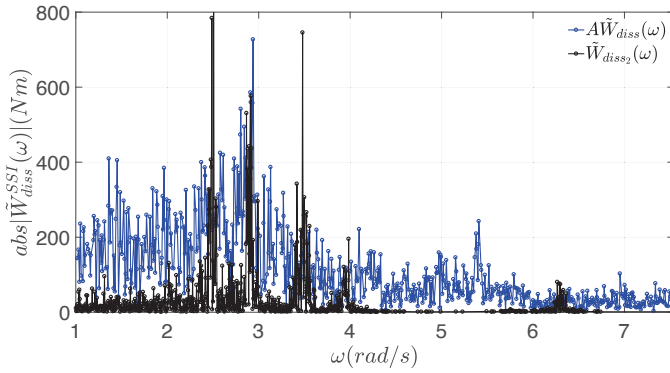
Figure 5.14: Comparison of quadratic damping to identify energy dissipation of the SSI

5
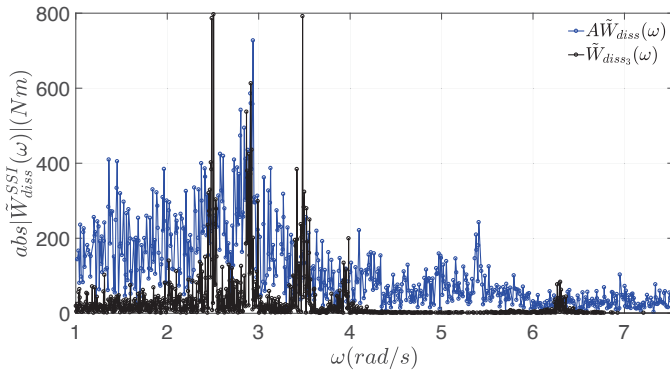
Figure 5.15: Comparison of hysteretic damping to identify energy dissipation of the SSI

$C^{\mathrm{SSI}}_{\theta_x}$ are the constants identified by means of the energy-flux analysis.
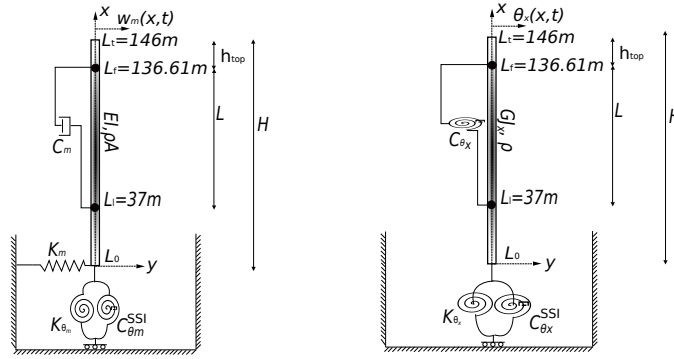
(a) Bending beam model   (b) Torsional beam model

Figure 5.16: One-dimensional continuous model representative for a tall building, including SSI effects

EoMs describing the small translational and torsional motions of the system in the Fourier
domain are

$$-\omega^2 \left(\sum_{k=1}^{N_{\text{cores}}} \rho_k A_k + \sum_{j=1}^{N_{\text{floors}}} \frac{M_j}{L} \right) \tilde{W}_m(x,\omega) + \sum_{k=1}^{N_{\text{cores}}} T_k \tilde{W}_m''(x,\omega) + \sum_{k=1}^{N_{\text{cores}}} EI_m^k \tilde{W}_m''''(x,\omega) = 0$$
(5.39)

where $m = y, z$, and

$$\omega^2 \left(\sum_{k=1}^{N_{\text{cores}}} \rho J_0^k + \sum_{j=1}^{N_{\text{floors}}} \frac{M_j}{L} \right) \tilde{\theta}_x(x,\omega) + \sum_{k=1}^{N_{\text{cores}}} GJ_x^k \tilde{\theta}_x''(x,\omega) = 0.$$
(5.40)

The boundary conditions at $x = L_0$ and $x = L_t$ are

$$\sum_{k=1}^{N_{\text{cores}}} EI_m^k \tilde{W}_{m,1}''(L_0,\omega) = \left(K_{\theta_m} + i\omega C_{\theta_m}^{\text{SSI}} \right) \tilde{W}_{m,1}'(L_0,\omega)$$

$$-\sum_{k=1}^{N_{\text{cores}}} EI_m^k \tilde{W}_{m,1}'''(L_0,\omega) = K_m \tilde{W}_{m,1}(L_0,\omega)$$

$$\sum_{k=1}^{N_{\text{cores}}} EI_m^k \tilde{W}_{m,3}''(L_t,\omega) = 0$$
(5.41)

$$\sum_{k=1}^{N_{\text{cores}}} EI_m^k \tilde{W}_{m,3}'''(L_t,\omega) = 0$$

$$\sum_{k=1}^{N_{\text{cores}}} GJ_x^k \theta_x'(L_0,\omega) = \left(K_{\theta_x} + i\omega C_{\theta_x}^{\text{SSI}} \right) \tilde{\theta}_x(L_0,\omega)$$

$$\sum_{k=1}^{N_{\text{cores}}} GJ_x^k \theta_x'(L_t,\omega) = 0$$
(5.42)

96

5. ENERGY-FLUX ANALYSIS AS A TOOL FOR IDENTIFYING THE CONTRIBUTION OF
SOIL-STRUCTURE INTERACTION TO DAMPING IN TALL BUILDINGS

and the interface conditions at $x = L_l$ and $x = L_f$ are

$$\sum_{k=1}^{N_{\text{cores}}} EI_m^k \left(\tilde{W}_{m,2}''(L_l, \omega) - \tilde{W}_{m,1}''(L_l, \omega) \right) = 0$$

$$-\sum_{k=1}^{N_{\text{cores}}} EI_m^k \left(\tilde{W}_{m,2}'''(L_l, \omega) - \tilde{W}_{m,1}'''(L_l, \omega) \right) = i\omega C_m \tilde{W}_{m,1}(L_l, \omega)$$

$$\tilde{W}_{m,2}(L_l, t) = \tilde{W}_{m,1}(L_l, \omega)$$

$$\tilde{W}_{m,2}'(L_l, \omega) = \tilde{W}_{m,1}'(L_l, \omega)$$

$$\sum_{k=1}^{N_{\text{cores}}} EI_m^k \left(\tilde{W}_{m,3}''(L_f, \omega) - \tilde{W}_{m,2}''(L_f, \omega) \right) = 0 \qquad (5.43)$$

$$-\sum_{k=1}^{N_{\text{cores}}} EI_m^k \left(\tilde{W}_{m,3}'''(L_f, \omega) - \tilde{W}_{m,2}'''(L_f, \omega) \right) = i\omega C_m \tilde{W}_{m,1}(L_f, \omega)$$

$$\tilde{W}_{m,3}(L_f, t) = \tilde{W}_{m,2}(L_f, \omega)$$

$$\tilde{W}_{m,3}'(L_f, \omega) = \tilde{W}_{m,2}'(L_f, \omega).$$

$$\sum_{k=1}^{N_{\text{cores}}} GJ_x^k \left(\tilde{\theta}_{x,2}'(L_l, \omega) - \tilde{\theta}_{x,1}'(L_l, \omega) \right) = i\omega C_{\theta_x}^{\text{SSI}} \tilde{\theta}_{x,1}(L_l, \omega)$$

$$\tilde{\theta}_{x,1}(L_l, \omega) = \tilde{\theta}_{x,2}(L_l, \omega) \qquad (5.44)$$

$$\sum_{k=1}^{N_{\text{cores}}} GJ_x^k \left(\tilde{\theta}_{x,3}'(L_f, \omega) - \tilde{\theta}_{x,2}'(L_f, \omega) \right) = i\omega C_{\theta_x}^{\text{SSI}} \tilde{\theta}_{x,2}(L_f, \omega).$$

The equations of motion, Eq. 5.39-5.40, boundary and interface conditions, Eqs. 5.41-5.44, are used to compute the following frequency equations, Eqs. 5.45-5.46, whose roots are complex-valued natural frequencies of the system.

$$\det|\mathbf{A}(\omega_n)| = 0 \qquad (5.45)$$

$$\det|\mathbf{B}(\omega_n)| = 0 \qquad (5.46)$$

$\mathbf{A}(\omega_n)$ is a 12x12 matrix, whose components are described in Appendix A.2. The complex-valued roots of Eq. 5.45 correspond to the translational modes of the structure and $\mathbf{B}(\omega_n)$ is a 6x6 matrix, whose components are described in Appendix A.3, defines the torsional modes. Complex-valued natural frequencies are used to compute the equivalent modal damping ratio, assuming SDoF dynamics, using the following expression:

$$\xi_n = \frac{\Im(\omega_n)}{\sqrt{\Re(\omega_n)^2 + \Im(\omega_n)^2}} \qquad (5.47)$$

The parameters described in the model depicted in Fig. 5.16 are quantified using the values given in Table. 5.2.

		$m = y$	$m = z$
H(m)	146		
$\sum_{k=1}^{N_{\text{cores}}} EI_m^k (Nm^2)$		$4.2e+14$	$8.5e+14$
$\sum_{k=1}^{N_{\text{cores}}} \rho_k A_k + \sum_{j=1}^{N_{\text{floors}}} \frac{M_j}{L}$ (Kg/m)	$4.0e+05$		
K_m(N/m)		$1.1e+10$	$1.0e+10$
K_{θ_z}(Nm/rad)			$5.25e+12$
K_{θ_y}(Nm/rad)		$7.95e+12$	
$C_{\theta_z}^{\text{SSI}}$(Nms/rad)			$3.5e+10$
$C_{\theta_y}^{\text{SSI}}$(Nms/rad)		$6.0e+10$	
C_m(Ns/m)		$5.0e+05$	$1.6e+06$
$\sum_{k=1}^{N_{\text{cores}}} GJ_m^k (Nm^2)$	$4.5e+14$		
C_{θ_x}(Nms/rad)	$2.0e+07$		
K_{θ_x}(Nms/rad)	$3.9e+12$		
$C_{\theta_x}^{\text{SSI}}$(Nms/rad)	$2.1e+10$		

Table 5.2: Identified parameters for the JuBi tower

5

The stiffnesses K_y, K_z, K_{θ_y}, K_{θ_z} and K_{θ_x}, shown in Table 5.2, are computed by means of the software Dynapile, making use of the pile plan of the building and the soil profile. The bending stiffness, EI_m, and the torsional stiffness, GJ_x are computed making use of the Young's modulus, E, and the shear modulus, G, corresponding to the building material and the technical information needed to calculate the moments of inertia I_m and J_x. The mass per unit length, ρA, of the building is calculated using the density of the reinforced concrete material and the area of the cores and outer walls, obtained via technical information provided in the drawings. The mass of the floors, M_j, is quantified using the technical information of the floors. Finally, the damping constant C_m, C_{θ_x}, $C_{\theta_z}^{\text{SSI}}$,$C_{\theta_y}^{\text{SSI}}$ and $C_{\theta_x}^{\text{SSI}}$ are obtained by means of the energy-flux analysis.

The resultant damping ratio associated with the translational and torsional modes are compared to the identified damping in Table 5.3.

	Identified (Averaged)	Energy method
ξ_y	1.0%	1.1%
ξ_z	1.2%	2.0%
ξ_{θ_x}	0.73%	1.2%

Table 5.3: Comparison of identified damping and energy-flux analysis

Table 5.3 shows that the identified equivalent viscous damping values are slightly lower than those obtained via energy-flux analysis. However, this discrepancy is acceptable, given the complexity of the structure. It is important to notice that the damping ratios shown in the right column (energy method) in Table 5.3 are the true modal damping ratios, whereas the experimentally identified damping ratios are indicative of the presence of the closely spaced modes shown in Fig. 5.6. However, for low-damped systems

like JuBi tower, these damping ratios are close enough to the modal damping values. Moreover, the process of damping identification via the energy-flux analysis contains some assumptions because of the complexity of the full-scale building system and environment. Therefore, damping identification leads to inaccuracies. Nevertheless, the energy-flux analysis establishes a consistent framework for damping identification.

5.5. ASSUMPTIONS AND CONCLUDING REMARKS

The assumptions used in this chapter to compute the energy dissipation in the superstructure and in the SSI are listed and discussed below.

- The assumption in Eq. 5.1 in Section 5.1.3 was made to accommodate the frequency range of building vibrations caused by wind loading (0-3Hz). Only global modes of the building were excited. Therefore, in-plane deformation of floors was not expected.

- In Section 5.2.1, a Euler–Bernoulli beam model was used to interpret the energy-flux analysis. Coupling effects considered by this model are shown in Eq. 5.3.

- To compute the energy change described in Eqs. 5.18-5.25 a few assumptions were made. First, the energy flux and the potential energy at the top were assumed to be negligible compared to the kinetic energy, because the potential energy of the building decreased with the distance from the foundation, like a cantilever beam. At the top level, this energy, owing to a very low bending and shear, was much smaller than the kinetic energy. The latter was maximal at the top in the fundamental mode of vibration, the basis for neglecting the potential energy. Regarding energy flux, one can justify as follows. The energy flux through the roof is zero. Therefore, the energy flux must be a continuous function of the coordinate, and it must be small and in close vicinity of the roof. Thus, the energy flux through the top level is neglected. Finally, Eqs. 5.18-5.25 are computed as an averaged value over the height of the building, given that data are collected at two heights of the structure.

- The assumption of using a constant velocity over the low part of the building (9th floor to ground level) is taken, because the lower part of the building is attached to a low-rise structure that is very stiff in the horizontal directions (Y and Z). It is much stiffer than the soil. Therefore, it is reasonable to assume that the lower part of the building will move horizontally as a rigid body, thereby having a constant horizontal velocity over its height.

In this work, the energy-flux analysis was applied to two parts of the building: to the superstructure and the soil-foundation system. Thus, the energy dissipated in the superstructure and in the soil-foundation system was identified independently. Therefore, the relative contribution of damping in each part of the structure to the overall damping was studied.
A quantification of damping in selected parts of a building is important in view of potential design improvements to allow for reduced accelerations subject to dynamic loads.

This method also enables identification of a damping mechanism that mimics the energy dissipated by the building. The damping constants associated with the dissipation in the superstructure and in the soil-foundation system identified by the energy-flux analysis were compared using a model that considers SSIs.

5

6

BASIC MODELS OF TALL BUILDINGS FOR DAMPING ASSESSMENT DURING THE DESIGN STAGE

In this chapter, damping of several tall buildings located in The Netherlands is studied using basic mechanical models. It has already been shown that, in high-rise buildings, there are several sources of energy dissipation. These can be represented by one or more damping mechanisms. Having a better understanding of the behaviour of the different damping mechanisms, building vibrations can be better controlled in the design stage to reduce vibrations that may cause nuisance to the building occupants. It is therefore the aim of this chapter to use basic mechanical models to study the contributions of the different damping sources to the total damping of several tall buildings located in The Netherlands. Results show that aerodynamic damping can be neglected for the studied buildings and that foundation damping might play an important role in the overall building damping certain soil characteristics typically found in The Netherlands.

6.1. MODELLING APPROACH

Several researchers developed damping predictors for high-rise buildings based on experimental data [1, 3–5]. Some studies attempted to identify damping in high-rise buildings experimentally or by developing complex, uncertain and time-consuming finite element method (FEM) models. The complexity and uncertainty in modelling a high-rise building with a FEM package rests on the fact there are many interconnected variables. There are several constraints that are extremely difficult to describe, except by fitting through experimental data. With the effort required to study just one building, it was decided to develop a simplified analytical model that can be used to study the dynamics of several high-rise buildings by changing only the parameters.

6.2. MODEL DESCRIPTION

Figure 6.1 shows a schematic representation of a high-rise building (Fig. 6.1a), and a model of a high-rise building (Fig. 6.1b). In the model, the superstructure (the part above ground) is mimicked making use of a Euler–Bernoulli beam. In principle, structures such as tall buildings are relatively flexible owing to their heights. Therefore, it seems reasonable to use Euler–Bernoulli beam theory to model the behaviour of the superstructure. It is evident that building structures are attached to the ground, restricting movement. Therefore, spring elements that mimic the ground resistance are attached to the bottom end of the beam. The spring elements that represent the ground resistance are shear and rotational. These types of springs were used because, during horizontal building vibration caused by wind loading, the horizontal and rotational ground resistance play a major role.

(a) Sketch of a high-rise building.   (b) Beam model of a high-rise building.
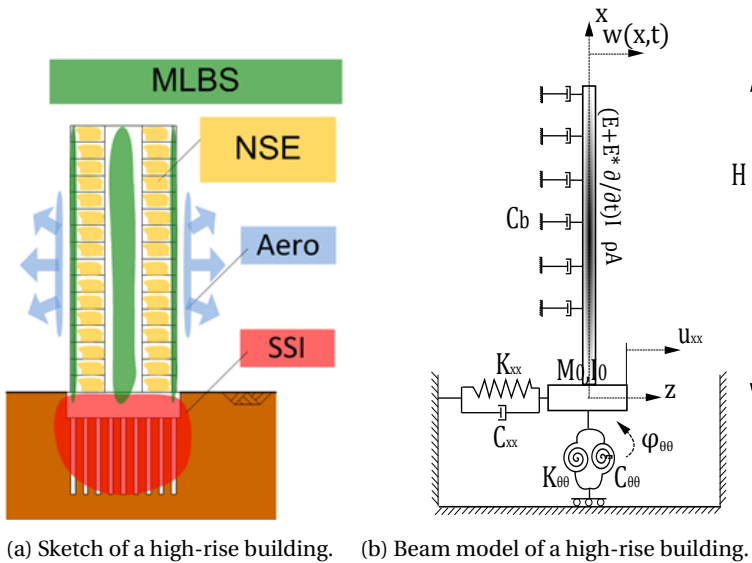
Figure 6.1: Modelling interpretation of a high-rise building with different sources of energy dissipation.

Tall buildings dissipate energy through several physical mechanisms, as explained in Chapter 1. A dashpot can be used to represent the energy dissipation in the field of small vibrations. The energy is dissipated proportionally to the velocity of the system (i.e. building). Another way of dissipating energy is described by the Kelvin–Voigt model [57]. Using this model energy dissipation can be computed as a function of beam rotation. Therefore, it mimics the energy dissipation in the material and the elements caused by deformations during building motions. A relation between the parameters of the model and the resistance and dissipation sources of a building can be established. Therefore, in the model EI describes the bending stiffness of the superstructure, K_{xx} and $K_{\theta\theta}$ are the horizontal and rotational soil-foundation stiffnesses respectively. The distributed dashpots attached to the beam mimic the aerodynamic energy dissipation (C_b) induced by the wind, and the Kelvin-Voigt model (E^*) describes the energy dissipation

caused by the material deformation of the MLBS and NSE and the energy dissipation in the connections of the superstructure. The ground has the capacity to dissipate energy in the form of wave radiation and via the material itself. These features are described in the model of the dashpot elements, C_{xx} and $C_{\theta\theta}$. Finally, the mass of the building is represented in the model as an uniformly distributed mass, ρA, along the beam. The mass of the building foundation, M_0, is locally concentrated at the bottom end in the beam model.

6.3. GOVERNING EQUATIONS

Experimental measurements in Chapter 2 showed that the three lower modes in each longitudinal and torsional direction are coupled. However, for simplicity and because damping (subject of this study) is not highly influenced by the coupling, it is assumed that vibrations occur only in one vibrational direction at a time. Thus, the displacement field can be described as follows:

$$u_x(x, z, t) = z\theta_y(x, t)$$
$$u_y(x, z, t) = u_z(x, z, t) = 0.$$

(6.1)

By the assumption of geometric linearity, the following strain expression can be written:

$$\epsilon_{xx} = \frac{\partial u_x}{\partial x} = z\frac{\mathrm{d}\theta_y}{\mathrm{d}x}$$
$$\gamma_{xz} = \frac{\partial u_x}{\partial z} + \frac{\partial u_z}{\partial x} = 0$$
$$\epsilon_{zz} = \frac{\partial u_z}{\partial z} = 0$$

(6.2)

By using the relations described in Eqs. 3.20-3.22, the Lagrangian density function of a Euler-Bernoulli bending beam can be defined as

$$\lambda\left(x, t, \mathbf{u}, \dot{\mathbf{u}}, \mathbf{u}''\right) = \frac{1}{2}\rho A(\dot{w}_z(x, t))^2 - \frac{1}{2}EI\left(w_z''(x, t)\right)^2$$

(6.3)

The dissipative energy function per unit length produced by the dashpots elements described in Fig. 6.1b is defined as

$$\mathscr{D}(\dot{\mathbf{u}}) = \frac{1}{2}C_b(\dot{w}_z(x, t))^2$$

(6.4)

The dissipation in the material is described in the constitutive model as

$$\sigma = \left(E + E^*\frac{\partial}{\partial t}\right)\epsilon.$$

(6.5)

Next, by introducing Eqs. 6.3-6.5 into Eqs. 3.70-3.72, equations of motion and boundary conditions (Fig. 6.1b) can be written.

6

$$\rho A \frac{\partial^2 w(x,t)}{\partial t^2} + C_b \frac{\partial w(x,t)}{\partial t} + \left(E + E^* \frac{\partial}{\partial t}\right) I \frac{\partial^4 w(x,t)}{\partial x^4} = F(x,t) \tag{6.6}$$

If $w(0,t) = u(t)$ and $\frac{\partial w}{\partial x}(0,t) = \varphi_{\theta\theta}(t)$, the boundary conditions can be written as

$$\left(E + E^* \frac{\partial}{\partial t}\right) \frac{\partial^2 w(0,t)}{\partial x^2} = K_{\theta\theta} \varphi_{\theta\theta}(t) + C_{\theta\theta} \frac{\partial \varphi_{\theta\theta}(t)}{\partial t} + I_0 \frac{\partial^2 \varphi_{\theta\theta}(t)}{\partial t^2}$$

$$-\left(E + E^* \frac{\partial}{\partial t}\right) I \frac{\partial^3 w(0,t)}{\partial x^3} = K_{xx} u(t) + C_{xx} \frac{\partial u(t)}{\partial t} + M_0 \frac{\partial^2 u(t)}{\partial t^2} \tag{6.7}$$

$$\left(E + E^* \frac{\partial}{\partial t}\right) I \frac{\partial^2 w(H,t)}{\partial x^2} = \left(E + E^* \frac{\partial}{\partial t}\right) I \frac{\partial^3 w(H,t)}{\partial x^3} = 0 \tag{6.8}$$

Having formulated the equation of motion and the boundary conditions of the model depicted in Fig. 6.1b, but prior to solving Eq. 6.6, parameter values of the model representing high-rise buildings should be derived. However, this is not a straightforward task. The models used to describe the physical behaviour of different parts of the building are explained in the following sections.

6.4. SOIL MODEL

The subject of soil-structure interaction has been a matter of study for many years [54]. These studies have resulted in the development of several tools for computing equivalent stiffnesses and damping values for SSI. These tools range from analytical solutions of rigid disks resting on a half-space or a layered half-space [58-64] to numerical tools such as FEMs [65] and boundary elements (BE) methods [66]. Both have the capacity to account for the geometry of the foundation. To solve the system of equations described by the model depicted in Fig. 6.1b, the resistance and the dissipation capacities of the ground should be quantified. This means that expressions for the springs, K_{xx} and $K_{\theta\theta}$, as well as the dashpots, C_{xx} and $C_{\theta\theta}$, should be described by the SSI model. Thus, the springs and the dashpots can be quantified for given soil characteristics. These values can be computed via analytical expressions or with numerical software. Here, several SSI models could have been used. However, it seemed convenient for this study to implement the well-established cone model [67, 68]. The results given by this model are compared to solutions given by a numerical software package in the next section.

6.4.1. THE CONCEPT OF THE CONE MODEL
A soil area having uniform properties can be modelled as an unbounded semi-infinite elastic body (i.e. a half-space) with certain properties (e.g. mass density ρ, constraint elastic modulus E_c, shear modulus G and Poisson's ratio v). When working with cone models, it is convenient to formulate the soil properties in terms of wave speeds, $c_p = \sqrt{E_c/\rho}$ and $c_s = \sqrt{G/\rho}$, combining the aforementioned soil properties. Many other relations between the different soil parameters were developed by Wolf [67].

A rigid massless disk resting on a half-space (Fig. 6.2a) is next introduced, representing the interaction between the foundation of a structure and the soil. The half-space below
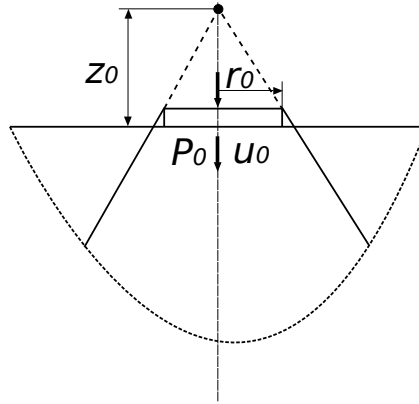
(a) Disk on surface of a half-space with cone model.
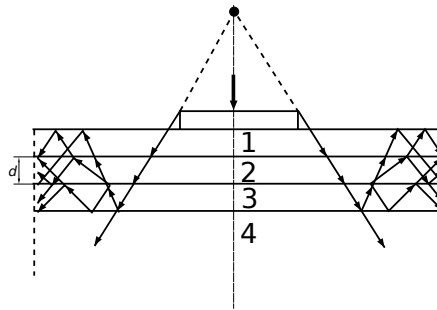
(b) Wave propagation in cone segments for surface disk on layered half-space.

Figure 6.2: Cone model for surface foundations description.

the disk is modelled as a semi-infinite cone with certain properties for each DoF. The opening angle of the cone is determined by the aspect ratio, z_0/r_0, which can be computed by equating the static stiffness of the cone formulated from the elastic equilibrium within the cone area and the closed-form solution of a rigid disk on a half-space based on exact elastic theory. Therefore, per the opening angle of the cone, the static-stiffness of the foundation can be computed. The dynamic stiffness is computed through the relationship between the displacements of the disk and the dynamic load acting on the disk, based on wave propagation. This relation is described by Green's functions. Figure 6.2b shows a wave propagation pattern in the soil generated by a vertical dynamic load on a rigid disk resting on a layered half-space.

6.4.2. COMPARISON OF THE CONE MODEL WITH A BEM MODEL IN A CASE STUDY

To study the reliability of the cone model (see Appendix B) for this work, a case study is used. The results of an equivalent spring stiffness and dashpot damping of the cone model are compared to the solutions obtained from the commercial software package, Dynapile, which includes the stiffness of the piles of the foundation.

To proceed with the comparison a building is selected. The selected building has a rectangular shape (E.M.C building) with the dimensions described in Fig. 2.8. The foundation contains 378 piles and supports a building 120 m high.

Soil parameters are identified using CPT at several locations within the foundation area prior to construction. In a CPT, the cone penetrates the soil to certain depth (25 m), measuring the resistance that the soil exerts against the cone sleeve. During penetration, a signal is registered every few centimetres, obtaining a full description of the soil characteristics as a function of depth. Using these data and certain correlations [52], the shear-wave speed as a function of depth can be identified, as shown in Fig. 6.3.
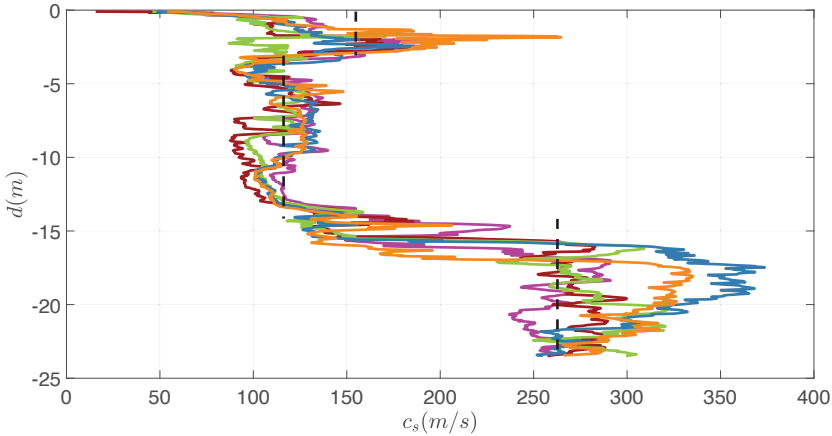
Figure 6.3: Soil shear-wave speed as a function of the soil depth at several spots of the E.M.C building location.

Figure 6.3 describes the shear-wave speed as a function of depth at the location of the foundation obtained using Robertson's correlation. Looking at the figure, three soil layers can be distinguished, and it can be said that the foundation rests on a soft soil.

Once the soil characteristics are identified and the foundation size is determined, a simulation using the cone model for this specific foundation can be performed. In the case of the numerical model the piles attached to the foundation are modelled. The characteristics of the piles are obtained from the technical information described in Table 6.1.

A sketch of the pile foundation modelled with the software package is shown in Fig. 6.4. The results are compared in terms of stiffness and damping of the transverse and rotation degree of freedom, since these are degrees of freedom of interest for the study.

E[KN/m^2]	ρ [Kg/m^3]	ξ[%]	r[m]	L[m]
$3e+07$	2300	0.5	0.25	20

Table 6.1: Pile characteristics.
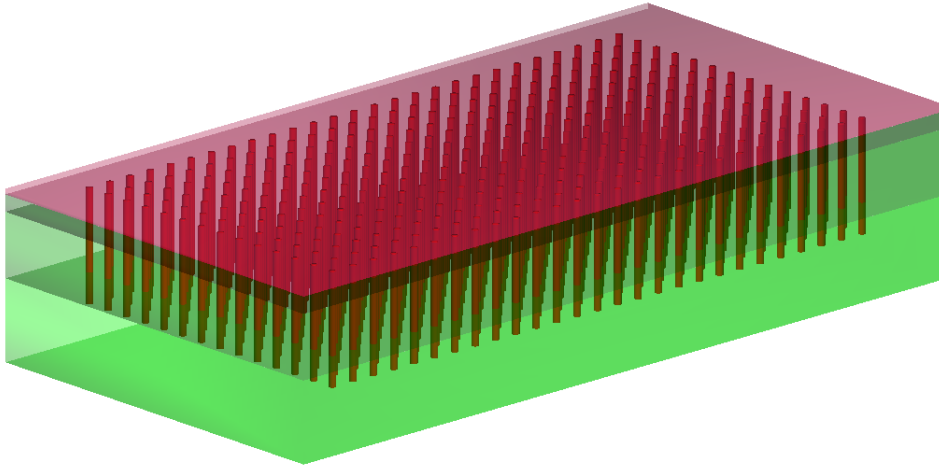
Figure 6.4: Pile foundation plan of the E.M.C building.
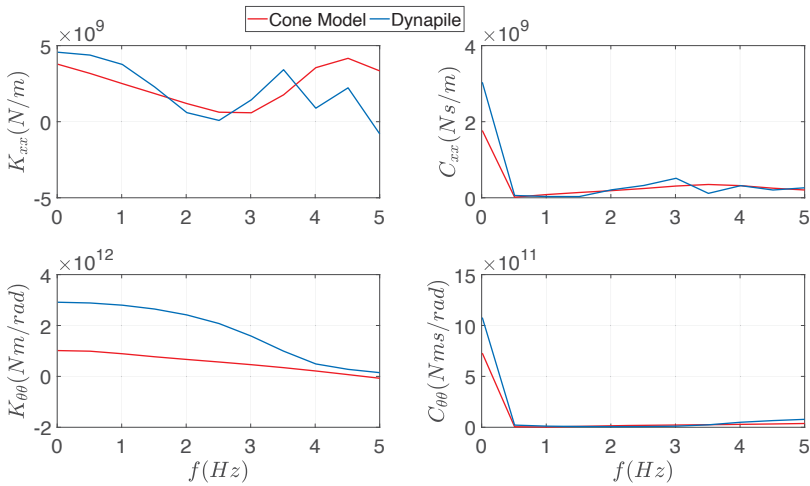
Figure 6.5: Soil stiffness and damping of the horizontal and rocking DoFs as a function of frequency.

Looking at the stiffnesses, K_{xx} and $K_{\theta\theta}$, it can be seen that the transverse stiffness obtained by the cone model is comparable to the Dynapile model. In the case of rotational stiffness, the cone model gives slightly lower stiffness values compared to Dy-

napile. These differences can be deduced from the fact that, in the cone model, pile resistance is not included. The horizontal resistance effect of the piles is nearly negligible. However, in the case of the rotational motion, the piles contribute more significantly to the overall stiffness. To overcome these differences, given that it is not feasible to reliably model many piles in the cone model, a correction factor is used.

In the case of damping, both models show highly comparable results. Thus, the overall damping is governed by the damping in the soil. Therefore, the contribution of the damping in the piles to the total soil damping is negligible.

6.5. AERODYNAMIC DAMPING

Another source of damping in a high-rise building is aerodynamic damping. The aerodynamic damping is generated by the aerodynamic interaction of wind with building. A constant wind stream falling on the structure makes the building vibrate. To study the effect of the aerodynamic damping in a high-rise building, a simplified 3-DoF model, shown in 6.6, is used.
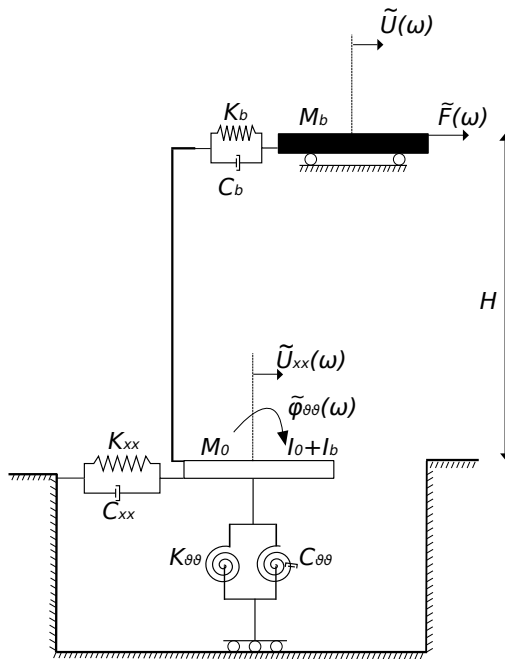
Figure 6.6: 3-DoF representative for a building to study the influence of the aerodynamic damping.

Equations of motion of the 3-DoF model are written in the frequency domain as follows:

$$-\omega^2 M_{\mathrm{b}} \tilde{U}(\omega) + (K_{\mathrm{b}} + \mathrm{i}\omega C_{\mathrm{b}})\, \tilde{U}_{\mathrm{b}}(\omega) = -\mathrm{i}\omega \frac{1}{2} \rho_{\mathrm{air}} \overline{V}_{\mathrm{wind}} BHC_\alpha \tilde{U}_{\mathrm{b}}(\omega)$$

$$-\omega^2 M_0 \tilde{U}_{\mathrm{xx}}(\omega) - (K_{\mathrm{b}} + \mathrm{i}\omega C_{\mathrm{b}})\, \tilde{U}_{\mathrm{b}}(\omega) + \left(\tilde{K}_{\mathrm{xx}} + \mathrm{i}\omega \tilde{C}_{\mathrm{xx}}\right) \tilde{U}_{\mathrm{xx}}(\omega) = 0 \tag{6.9}$$

$$-\omega^2 \left(I_0 + I_{\mathrm{b}}\right) \tilde{\varphi}(\omega) - (K_{\mathrm{b}} + \mathrm{i}\omega C_{\mathrm{b}})\, H\tilde{U}_{\mathrm{b}}(\omega) + \left(\tilde{K}_{\theta\theta} + \mathrm{i}\omega \tilde{C}_{\theta\theta}\right) \tilde{\varphi}(\omega) = 0$$

In a condensed matrix form, Eq. 6.9 can be rewritten as

$$\left\{ -\omega^2 \begin{bmatrix} M_{\mathrm{b}} & 0 & 0 \\ 0 & M_0 & 0 \\ 0 & 0 & (I_0 + I_b) \end{bmatrix} + \begin{bmatrix} K_b + \mathrm{i}\omega C_{\mathrm{eff}} & -(K_b + \mathrm{i}\omega C_{\mathrm{eff}}) & -(K_b + \mathrm{i}\omega C_{\mathrm{eff}})\, H \\ -S_{\mathrm{b}} & S_{\mathrm{b}} + S_{\mathrm{xx}} & S_{\mathrm{b}} H \\ -S_{\mathrm{b}} H & S_{\mathrm{b}} H & S_{\mathrm{b}} H^2 + S_{\theta\theta} \end{bmatrix} \right\}$$

$$\begin{bmatrix} \tilde{U}(\omega) \\ \tilde{U}_{xx}(\omega) \\ \tilde{\varphi}_{\theta\theta}(\omega) \end{bmatrix} = 0. \tag{6.10}$$

where $\tilde{U}_{\mathrm{b}}(\omega) = \tilde{U}(\omega) - \tilde{U}_{xx}(\omega) - H\tilde{\varphi}(\omega)$, $C_{\mathrm{eff}} = C_{\mathrm{b}} + 1/2\rho_{\mathrm{air}} \overline{V}_{\mathrm{wind}} BHC_\alpha$, $S_{\mathrm{b}} = K_{\mathrm{b}} + \mathrm{i}\omega C_{\mathrm{b}}$ and $S_{\mathrm{xx}} = K_{\mathrm{xx}} + \mathrm{i}\omega C_{\mathrm{xx}}$ and $S_{\theta\theta} = K_{\theta\theta} + \mathrm{i}\omega C_{\theta\theta}$. It is then clear from the system above, that the matrix is non-symmetric for values $C_\alpha \neq 0$. However, when the damping coefficient, C_{b}, is sufficiently large, whereas $C_\alpha \neq 0$, it can be assumed that C_α is negligible. Thus, the system can be considered symmetric. Therefore, the same amount of energy coming into the system goes out.

Group 1 of buildings described in Table 6.2 are used to study the influence of the aerodynamic damping in high-rise buildings. To do so, the system of equations shown in Eq. 6.10 using matrix form ($\mathbf{Ac} = 0$) can be solved as follows:

$$\det|\mathbf{A}(\omega_n)| = 0. \tag{6.11}$$

The solution of Eq. 6.11 consists of complex-valued natural frequencies, ω_n, where the overall damping can be extracted as:

$$\xi_{\mathrm{aero}}^n = \frac{\Im(\omega_n)}{\sqrt{\Re(\omega_n)^2 + \Im(\omega_n)^2}}. \tag{6.12}$$

Results of the study show that the aerodynamic damping can be considered negligible, meaning that in all cases $\xi_{\mathrm{aero}} \leq 0.2\%$. Another comparison has been made making use of the aerodynamic damping predictor developed by Davenport [1].

$$\xi_{\mathrm{aero}} = \frac{C_{\mathrm{Drag}}}{4\pi} \frac{\rho_{\mathrm{air}}}{\rho_{\mathrm{build}}} \frac{\overline{V}}{f_0 D} \tag{6.13}$$

The resultant damping values obtained by applying Eq. 6.13 also lead to the conclusion that aerodynamic damping is negligible. Therefore, no more effort is given to identify the most adequate aerodynamic damping mechanism. However, if a building is sufficiently light and tall, the aerodynamic damping could play an important role in the overall damping.

6.6. STUDY OF THE FOUNDATION DAMPING CONTRIBUTION TO THE TOTAL DAMPING OF SEVERAL BUILDINGS LOCATED IN THE NETHERLANDS

Given that all the described sources of energy dissipation in a tall building are now defined, the damping of several high-rise buildings located in The Netherlands can now be studied. To this end, the model represented in Fig. 6.1b is used. The EoM and boundary conditions are formulated in the frequency domain as follows:

$$-\omega^2 \rho A \tilde{W}(x,\omega) + i\omega C_{\mathrm{b}} \tilde{W}(x,\omega) + \left(E + i\omega E^*\right) I \tilde{W}''''(x,\omega) = \tilde{F}(x,\omega) \qquad (6.14)$$

$$\left(E + i\omega E^*\right) \tilde{W}''(0,\omega) = K_{\theta\theta} \tilde{\varphi}_{\theta\theta}(\omega) + i\omega C_{\theta\theta} \tilde{\varphi}_{\theta\theta}(\omega) - \omega^2 I_0 \tilde{\varphi}_{\theta\theta}(\omega)$$
$$-\left(E + i\omega E^*\right) I \tilde{W}'''(0,\omega) = K_{\mathrm{xx}} \tilde{U}(\omega) + i\omega C_{\mathrm{xx}} \tilde{U}(\omega) - \omega^2 M_0 \tilde{U}(\omega) \qquad (6.15)$$
$$\left(E + i\omega E^*\right) I \tilde{W}''(L,\omega) = \left(E + i\omega E^*\right) I \tilde{W}'''(L,\omega) = 0.$$

For simplification in the analysis and given that its influence is negligible, the aerodynamic damping is assumed to be zero ($C_{\mathrm{b}} = 0$). While identifying damping, the model and data extracted from the measurements are used. The studied buildings are described in Table 6.2.

Building name (Group)	H [m]	Found. area [m²]	ρ [$\frac{\mathrm{kg}}{\mathrm{m}^3}$]	K_{b} [$\frac{\mathrm{KN}}{\mathrm{m}}$]	ω_1 [$\frac{\mathrm{rad}}{\mathrm{s}}$]	ξ_1 [%]	$\frac{H}{R0}$	Soil prof.
Churchill (1)	83	1196	300	$1.2e+08$	3.45	1.7	4	1
New E.M.C (1)	121.5	1152	250	$5.8e+08$	3.35	1.6	6	2
Hoftoren (1)	142	1196	300	$1.0e+08$	2.5	1.9	8	3
MonteVideo (1)	131	792	210	$3.2e+07$	2.6	1.7	8	1
Amro tower (1)	94	1166	300	$9.0e+07$	2.5	1.7	5	1
EWI tower (2)	90	1620	165	$9.5e+07$	2.75	1.5	4	1
Bowes (2)	61	513	395	$1.7e+08$	5.5	1.8	5	4
Ned.Bank (2)	58	785	240	$5.1e+08$	3.9	1.6	4	4
Old E.M.C (2)	104	2608	300	$3.2e+07$	3.0	2.1	4	2
CMR (2)	65	990	300	$9.8e+07$	3.95	1.7	4	1
Laakhaven (2)	36	468	430	$2.2e+08$	7.7	2.1	3	3
Ommoord (2)	60	625	295	$1.2e+08$	5.0	1.3	4	2

Table 6.2: Characteristics of the studied buildings.

Data from the Group 1 buildings in Table 6.2 were extracted for this work. However, the data from the Group 2 buildings is collected from given technical information.

The necessary information about the building structure to perform the study is fully described in Table 6.2. However, this is not true for the soil, where the buildings are located. Therefore, experimental data from CPT's of several locations in The Netherlands was collected. The data obtained at the locations where measurement were performed can be

extrapolated to other locations in The Netherlands, meaning that this data is representative of soil characteristics of other locations in The Netherlands. Consequently, four types of soil profiles are described.

Profile 1			Profile 2		
depth[m]	c_s [m/s]	ρ[kg/m3]	depth[m]	c_s [m/s]	ρ[kg/m3]
11	145	1700	3	127	1700
6.5	124	1400	11.5	113	1400
7.5	269	1700	10.9	266	1700
$\overline{V}_{s,30}$	160		$\overline{V}_{s,30}$	149	

Profile 3			Profile 4		
depth[m]	c_s [m/s]	ρ[kg/m3]	depth[m]	c_s [m/s]	ρ[kg/m3]
14	177	1700	14.5	111	1700
2	153	1400	10.5	277	1400
9	254	1700			
$\overline{V}_{s,30}$	195		$\overline{V}_{s,30}$	145	

Table 6.3: Representative soil profiles in The Netherlands.

Because a goal of this study is to quantify the damping contribution of several damping sources to the total damping, two main sources of energy dissipation are described. The building damping (superstructure), which accounts for the energy dissipation generated by the deformation of the building elements and in the material, is represented by the Kelvin–Voigt material damping model, $\sigma = (E + E^*\partial/\partial t)\epsilon$. Foundation damping, represented by dashpots C_{xx} and $C_{\theta\theta}$, accounts for the geometrical and the material damping in the soil.

To determine the damping contribution of the two damping sources the superstructure and the soil-foundation to the total damping, the model depicted in Fig. 6.1b and information given in Table 6.2 are used. Next, an iterative solution procedure can be started.

1. The cone model implemented per Appendix B makes use of the foundation size and the corresponding soil profile at the building location. Thus, the vibration frequency of a high-rise building is relatively low, the soil stiffness does not vary much at this frequency range. A stiffness value for K_{xx} and $K_{\theta\theta}$ at the lowest vibration frequency of the building is selected.

2. Setting all damping parameters, E^*, C_{xx}, C_{xx} and $C_{\theta\theta}$, to zero, estimating the mass density of the building, ρA, and using the identified lowest natural frequency given in in Table 6.2, the stiffness of the building, K_b, can be determined. In the Group 2 cases, the building stiffness is given as a reference value. If, by using this value, the natural frequency is not fully matched by the one identified experimentally, then K_b is tuned such that the match is satisfactory. It is extremely important that the natural frequency of the system is well-identified, because this has a high impact in the overall damping calculation.

3. C_{xx} and $C_{\theta\theta}$ are parametrized based on the cone model (see Appendix B) results using the same strategy that was used for soil stiffness. By solving the system of algebraic equations (Eq. 6.15) a complex-valued natural frequency is obtained. Making use of the expression described by Eq. 6.12 an overall damping ratio can be obtained. This is the result of the foundation damping for the lowest natural frequency, ξ_{found}.

4. Finally, by comparing ξ_{found} with the total damping, ξ, identified by means of the measurements, the damping contribution of the foundation and the building can be established. Consequently, E^* can also be quantified.

Using the above procedure, Fig. 6.7 can be drawn. The y-axis of the figure describes the damping contribution of the foundation to the total damping. Additionally, the x-axis shows the influence of the foundation stiffness to the total stiffness.
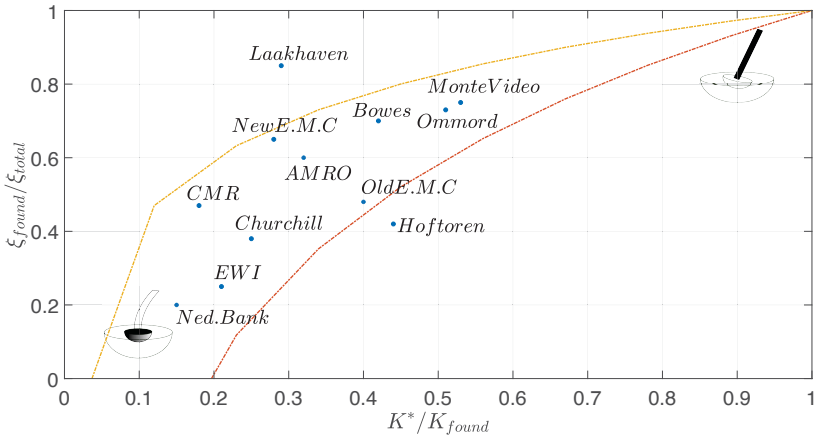
Figure 6.7: Influence of the foundation damping to the total damping for several buildings located in The Netherlands.

The total stiffness and the foundation stiffness are computed as shown in Eqs. 6.16-6.17

$$\frac{1}{K^*} = \frac{1}{K_{\text{b}}} + \frac{1}{K_{\text{found}}} \tag{6.16}$$

where

$$\frac{1}{K_{\text{found}}} = \frac{1}{K_{\text{xx}}} + \frac{(H+h)^2}{K_{\theta\theta}}. \tag{6.17}$$

Looking at Fig. 6.7, several interesting conclusions can be drawn. The dashed lines are the result of plotting two logarithmic functions (red: $y = 0.6\ln(x) + 1$, yellow: $y = 0.25\ln(x) + 1$) starting at $\xi_{\text{found}}/\xi_{\text{total}} = 1$ and $K^*/K_{\text{found}} = 1$. This is done because a logarithmic function well represents the behaviour a high-rise building experiences when

changing the stiffness ratio from $K^*/K_{\text{found}} = 0$ to $K^*/K_{\text{found}} = 1$. This behaviour was more extensively investigated in [69]. In this case, the slopes of the logarithmic functions are chosen such that all dots (buildings) in the graph fall in an area enclosed within the dashed lines. Whereas each building is represented by a single dot, a certain bandwidth can be established, and the building behaviour within this graph can be interpreted.

Looking at the dots representing buildings, there are two that fall outside the area delimited by the dashed lines. However, the height of the Laakhaven building is very low compared to the others. Thus, shorter buildings with larger fundamental frequencies will traverse the higher part of this graph. The other building outside the lines is the Hoftoren. It is a tall building. However, it consists of a tall tower attached to a low-rise building. This may change the overall stiffness ratio behaviour. In any case, this building falls just outside the suggested area. Recall that the two dashed lines are tuned such that most of the buildings fall with in this area. Therefore, they are not created from real data. Finally, it can be noted that all buildings resting on soil profile of Types 2 and 4 per Table 6.2, and corresponding to the softer soils have a larger foundation damping influence: $\xi_{\text{found}} \geq 50\%\xi_{\text{total}}$. In the case of the buildings resting on soil profiles 1 and 3, the influence is lower. However, it is still important to consider the foundation stiffness and damping.

6.7. STUDY OF THE BUILDING DAMPING USING ENERGY INTERPRETATION

Energy dissipation in the superstructure is influenced by dissipation in the foundation and vice versa. Thus, structural damping can by modified by foundation flexibility. The effect of the damping variation in the superstructure of several buildings is studied by means of an energy evaluation.

An objective of the study consists of evaluating the deformation shape of the superstructure. It is shown in the section above that the energy dissipation in the superstructure is assumed to be related to the rotation of building components and the deformation in the material. This is necessarily related to the vibrational shape of the structure. Additionally, maximum energy dissipation in the building caused by rotation is achieved when the foundation is highly stiff. This can be represented in a model as a fixed-base foundation. The relative stiffness between the superstructure and the foundation plays a major role in the rotation of the building. The stiffer the foundation, the higher the building rotation. Therefore, the higher the building damping. Conversely, in the case of a soft foundation, the building rotation is lower, behaving almost as a rigid body. Consequently, the effective damping in the superstructure is lower.

To analyse this behaviour, the following procedure is used. The work done by a dissipative force in a period of vibration, T, can be written as

$$W_{\text{diss}} = \int_0^T F_{\text{D}}\,\mathrm{d}u = \int_0^T F_{\text{D}}v\,\mathrm{d}t \tag{6.18}$$

where, force F_{D} is defined as

$$F_{\text{D}} = E^* I \dot{w}''''(x,t). \tag{6.19}$$

The energy dissipation rate can be described as

$$W_{\text{diss}}^{\text{rate}}(t) = \int_0^L F_D \, \dot{w}(x,t) \mathrm{d}x = \int_0^L E^* I \dot{w}''''(x,t) \, \dot{w}(x,t) \mathrm{d}x. \tag{6.20}$$

To study the influence of the foundation stiffness on building damping Eq. 6.21 is used.

$$\bar{\epsilon}_b(t) = \frac{W_{\text{diss}}^{\text{rate,flex}}(t)}{W_{\text{diss}}^{\text{rate,fix}}(t)} \tag{6.21}$$

The numerator gives the energy dissipation rate of the flexibly supported building, whereas the denominator gives that of the fixed bottom of the building. Using the method of separation of variables, $w(x,t) = \sum_{n=1}^{\infty} W_n(x)\psi_n(t)$, the ratio, $\bar{\epsilon}_b$, can be expressed as

$$\bar{\epsilon}_b(t) = \frac{E^* I \sum_{n=1}^{\infty} \sum_{m=1}^{\infty} \dot{\psi}_{n,\text{flex}}(t) \dot{\psi}_{m,\text{flex}}(t) \int_0^L W_{n,\text{flex}}''''(x) W_{m,\text{flex}}(x) \mathrm{d}x}{E^* I \sum_{n=1}^{\infty} \sum_{m=1}^{\infty} \dot{\psi}_{n,\text{fix}}(t) \dot{\psi}_{m,\text{fix}}(t) \int_0^L W_{n,\text{fix}}''''(x) W_{m,\text{fix}}(x) \mathrm{d}x}. \tag{6.22}$$

If solely the first mode is accounted for ($n = m = 1$) Eq. 6.22 can be rewritten as:

$$\bar{\epsilon}_b(t) = \frac{\int_0^L W_{1,\text{flex}}''''(x) W_{1,\text{flex}}(x) \mathrm{d}x}{\int_0^L W_{1,\text{fix}}''''(x) W_{1,\text{fix}}(x) \mathrm{d}x} \frac{\dot{\psi}_{1,\text{flex}}^2(t)}{\dot{\psi}_{1,\text{fix}}^2(t)} \tag{6.23}$$

For a qualitative assessment of the effect of the foundation stiffness, the time dependence of $\bar{\epsilon}(t)$ is neglected and the following expression is analyzed:

$$\bar{\epsilon}_b = \frac{\int_0^L W_{1,\text{flex}}''''(x) W_{1,\text{flex}}(x) \mathrm{d}x}{\int_0^L W_{1,\text{fix}}''''(x) W_{1,\text{fix}}(x) \mathrm{d}x} \tag{6.24}$$

This study uses four buildings of Group 1 (Table 6.2) having different slenderness ratios. Results are drawn in the graph (Figs. 6.8-6.9). To plot these graphs, the following steps were followed.

1. For engineers, it is more intuitive to describe soil stiffness using soil shear-wave speed. Given that building damping is a function of soil stiffness, the layered soils defined in Table 6.3 can been simplified to a homogeneous half-space using Eq. 6.25. This formula gives an equivalent shear-wave speed in the first 30 m depth.

$$\bar{c}_{s,30} = \frac{30}{\sum_{m=1}^{\text{Nlayers}} \left(\frac{d_m}{\bar{v}_m}\right)}. \tag{6.25}$$

   where d_m is the layer depth, and $\bar{v}_m$ is the averaged shear-wave speed in the layer.

2. For each building case, W_{fix} is computed based on a fixed-base bending-beam model.

3. For each building case, and for each selected soil stiffness, W_{flex} is computed. The difference between W_{fix} and W_{flex} rests with the integration constants, $C_i (i = 1...4)$, as shown in Appendix A.4. They contain the influence of the boundary conditions in this case the foundation flexibility.

4. Finally, $\bar{\epsilon}_b$ is computed. The resultant is directly comparable to the damping ratio between the fixed-base building and the flexible-base building.

The result of applying this procedure to the studied buildings is shown in Figs. 6.8-6.9.
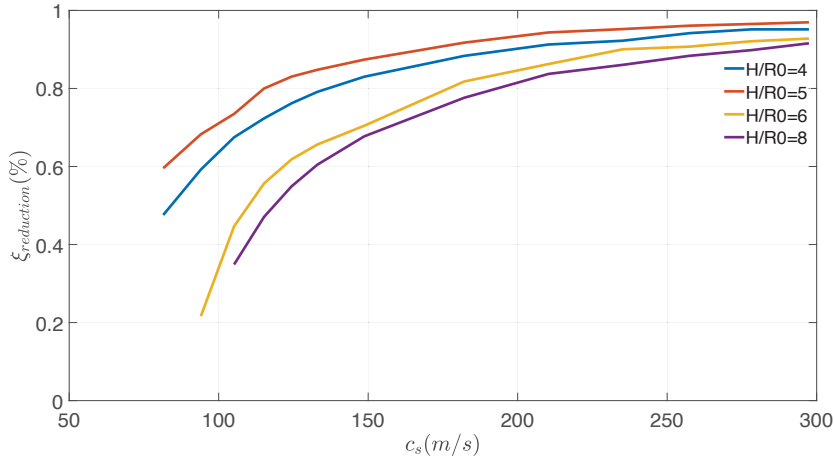
Figure 6.8: Building damping reduction as a function of the soil stiffness for several buildings with different slenderness ratios (H/R0) in The Netherlands.

Figure 6.8 shows the building damping reduction as a function of soil stiffness. The y-axis is bounded between 0 and 1, where 1 corresponds to a fixed-base foundation. It is tempting to think that, for softer soils the overall building damping is lower. This, is principally the case. However, if the soil is sufficiently soft, and depending on the soil material damping, building damping reduction can be compensated by soil damping, which may contribute largely to the overall damping, resulting in a higher overall damping for the building. This behaviour is shown in Figs. 6.8-6.9.

Comparing Figs. 6.8-6.9, it can be observed that the foundation damping grows faster than the building damping decreases for soils with small shear-wave speeds. Therefore, for soft-soil cases, soil damping might play a major role in the overall damping quantification.

6.8. CONCLUDING REMARKS

This chapter was devoted the influence of the different sources of damping in several high-rise buildings by using an analytical model. A beam element was used to mimic building behaviour, and the cone model was used to describe the SSI. An analytical
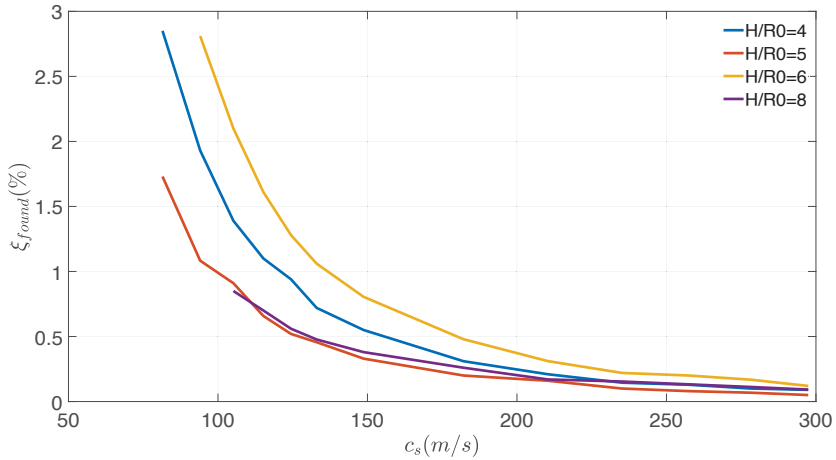
Figure 6.9: Foundation damping as a function of the soil stiffness for several buildings with different slenderness ratios (H/R0), located in The Netherlands.

model was used, because with a unique model, several buildings can be studied, and results can be compared. Additionally, experimental data collected from the measurement campaign for each building was used. The results presented in this chapter show that foundation damping can play a major role in the overall damping if the soil has soft characteristics, such as the soils in The Netherlands present. Moreover, it is shown that aerodynamic damping can be considered negligible for the studied buildings under certain wind conditions. However, if building characteristics were to change (e.g. they become much more lightweight), aerodynamic damping may play a role in the overall damping of the building.

7

CONCLUSIONS

The aim of this research was to develop a tool for damping prediction in high-rise buildings located in The Netherlands. To this end, experimental data was collected from measurement campaigns on several buildings located in The Netherlands. See Chapter 2. To identify the equivalent building damping, two techniques were used: half-power bandwidth (HPBW) and random decrement technique (RDT). The HPBW method is a technique based on an SDoF system in the frequency domain. Vibrations in high-rise buildings occur in all directions at the same time, and usually, the vibrational modes are closely spaced. This means that the HPBW technique, in most cases, cannot be directly applied to building damping identification. Therefore, some manipulations were made prior to applying the technique. Moreover, because the obtained damping value is real-valued, it is essential to assume damping matrices are diagonal. Therefore, the damping cannot precisely correspond to the modal damping. However, it provided a good estimate of the equivalent viscous damping, given the low damping characteristic of tall buildings.

In the past, several ready-to-use damping predictors for high-rise buildings were developed. Results of RDT, as applied to the instrumented buildings, were compared to the resultant damping, calculated by means of the amplitude-dependent damping predictors. However, the damping values obtained with these predictors provided an unacceptable scatter, compared to the experimentally identified damping values. Furthermore, the human perception to building vibrations was studied by means of the H. van Koten criteria, which shows that the accelerations experienced by the instrumented buildings during wind-induced vibrations did no overstep a level-F threshold, and no crack formation on the structure was detected. Therefore, it was reasonable to use linear elastic models to study the influence of damping on high-rise structures subject to wind-induce vibrations. Moreover, these criteria established that the acceleration levels experienced by the instrumented buildings were barely perceptible.

However, it was evidenced that one can still feel insecure in the interior of the buildings. This leads us to assume that human perception to vibration is extremely subjective. For all the above-mentioned reasons, it seems therefore necessary to investigate deeper the

phenomena of damping in high-rise buildings. To this end, the possible sources of energy dissipation were identified, as discussed in Chapter 1. Generally, the main sources of energy dissipation are related to the structure, the soil that interacts with the foundation and the wind around the building. In this work, additional damping was not considered, given that the focus was placed on using the dissipation mechanisms of the building to improve building design.

In Chapter 6, the aerodynamic damping generated by wind gusts around the building was shown to be negligible compared to the structural and soil damping for the studied cases. However, if the characteristics of the building were to change, aerodynamic damping may play an important role in the overall quantification of damping. The structure and the soil-foundation can dissipate energy in different forms. In the structure, the deformation of the material or the friction between the structural elements consist of two forms of energy dissipation. If the building vibration amplitude is sufficiently large, crack formation can occur, generating an additional energy sink. However, this phenomenon was not observed in the instrumented buildings. In the soil, energy is dissipated in the form of wave propagation and friction between the soil particles. Separately identifying each energy dissipation source should, in principle, lead to better quantification of overall building damping. This creates difficulties, however, and when these are combined, the identification of each energy source becomes extremely uncertain. In the case of modal analysis, extensive information of the structural behaviour is needed. This is unfortunately not possible in the case of high-rise buildings subject to ambient vibrations, given that wind loads only excite the lower frequency modes of the building.

To overcome this issue, an alternative method to identify energy dissipation in specific parts of a structure was proposed and used. This method is based on energy-flux analysis. Energy flux is a well-established concept in several fields, but not in the field of structural mechanics. This method was used because it did not require a modal representation for the analysis. Making use of the energy method, the energy dissipated at certain parts of the structure can be quantified by formulating the energy-balance equation, which is extensively described in Chapter 3. The interaction with the rest of the structure was then made using the energy-flux term. This term quantifies the amount of energy coming in and going out of a selected area of the structure. Practical applications of the energy method for identification purposes are extensively described in Chapters 4 and 5. The energy-flux analysis was used in a cantilever lab-scale beam to identify material damping. Then, a more complex steel-frame lab-scale structure was used for damping identification in the connections. The energy method was used to identify the energy dissipation in a full-scale building. Given the limitation already explained in Chapter 5, the analysis extends separately to the identification of the energy dissipation in the superstructure and the soil-foundation. The quantification of energy dissipation of localized areas is an approach that enables us to study the suitability of different damping mechanisms by computing the energy dissipation only once. Thus, based on results presented in Chapters 4 and 5, the energy-flux analysis consisted of a solid framework for damping identification. Whereas the benefits of using the energy approach are evident, it is still not a ready-to-use tool for engineering practice. Therefore, further effort should be made to generalize the approach, especially when identifying energy dissipation with a damping mechanism.

In Chapter 6, basic mechanical models with full-scale experimental data were used for damping assessment. The main sources of energy dissipation in high-rise buildings are related to the structure, the soil-structure interaction (SSI) and the wind around the building. Because the damping generated by wind around the building was negligible, the other energy dissipation sources were more important. Thus, quantifying the damping of each dissipation source acting together is extremely uncertain. From the modelling perspective, there are no reliable models to quantify the damping in the building structure. However, for the SSI, several models exist. The parameters in the soil are very uncertain, making the analysis of SSI equally uncertain. Therefore, a simplified model for the SSI was selected. The cone model, developed by Wolf, was used. This model helped us quantify stiffness and damping via a spring and a dashpot of the SSI in both dissipation capacities of the soil (i.e. geometrical damping and material damping). Given the low frequency range of vibration, material damping became the main source of dissipation energy in the soil. As noted, the sources of energy dissipation in the building structure are caused by the material deformation and crack propagation in the material. The recorded data from the instrumented buildings evidenced that these buildings experienced small vibration amplitudes. Consequently, an attempt to relate building damping with the relative deformation of the building was made. Given that the damping assessment was aimed at the modal vibration, we presumed a certain deformation shape of the building. This was done because energy dissipated is based on the bending moments in the building, which is maximal when the foundation stiffness is infinite. Based on this analysis, graphs were plotted and interesting conclusions were drawn.

A structure with a more flexible base decreases the effective damping. However, this can be compensated in cases where soils are very soft, thus significantly increasing the overall damping. Therefore, foundation damping may play a major role in the overall damping for certain soil characteristics. During this research, it was induced that the proper damping identification must begin with the correct identification of the modal frequencies of the structure. This result of this work encompasses the development and application of a new approach for damping identification and the investigation of the damping contribution sources in several high-rise buildings via basic mechanical models and experimental data.

BIBLIOGRAPHY

REFERENCES

[1] A. G. Davenport and P. H. Caroll, *Damping in tall buildings: its variability and treatment in design,* Proc. of ASCE Spring Convention, Seattle, USA , 42–57 (1986).

[2] C. K. Wong, J. Q. Fang, and A. P. Jeary, *Random damping in buildings and its ar model,* Journal of wind engineering and industrial aerodynamics **79**, 159–167 (1999).

[3] A. P. Jeary, *Damping in tall buildings—a mechanism and a predictor,* Earthquake Engineering & Structural Dynamics **14**, 733–750 (1986).

[4] S. Lagomarsino, *Forecast models for damping and vibration poriods of buildings,* Wind Engineering and Industrial Aerodynamics **48**, 221–239 (1993).

[5] Y. Tamura, N. Satake, T. Arakawa, and A. Sasaki, *Damping evaluation using full-scale data of buildings in japan,* Journal of Structural Engineering **129**, 470–477 (2003).

[6] E. R. Aquino and Y. Tamura, *On stick–slip phenomenon as primary mechanism behind structural damping in wind-resistant design applications,* Journal of Wind Engineering and Industrial Aerodynamics **115**, 121–136 (2013).

[7] R. E. Aquino and Y. Tamura, *Framework for structural damping predictor models based on stick-slip mechanism for use in wind-resistant design of buildings,* Journal of Wind Engineering and Industrial Aerodynamics **117**, 25–37 (2013).

[8] H. Marukawa, N. Kato, K. Fujii, and Y. Tamura, *Experimental evaluation of aerodynamic damping of tall buildings,* Journal of Wind Engineering and Industrial Aerodynamics **59**, 177–190 (1996).

[9] J. Wohlever and R. Bernhard, *Mechanical energy flow models of rods and beams,* Journal of Sound and Vibration **153**, 1–19 (1992).

[10] J. A. Wickert and C. Mote, *On the energetics of axially moving continua,* The Journal of the Acoustical Society of America **85**, 1365–1368 (1989).

[11] R. Barakat, *Transverse vibrations of a moving thin rod,* Journal of The Acoustical Society of America **43** (1968).

[12] Y. Lase, M. Ichchou, and L. Jezequel, *Energy flow analysis of bars and beams: Theoretical formulations,* Journal of Sound and Vibration **192**, 281–305 (1996).

[13] O. Bouthier and R. Bernhard, *Simple models of the energetics of transversely vibrating plates,* Journal of Sound and Vibration **182**, 149–164 (1995).

[14] F. Han, R. Bernhard, and L. Mongeau, *Energy flow analysis of vibrating beams and plates for discrete random excitations,* Journal of Sound and Vibration **208**, 841–859 (1997).

[15] A. Lebot and L. Jezequel, *Energy methods applied to transverse vibraitons of beams,* in *Proceedings of the 4th International Congress on Intensity Techniques* (Senlis (France), 1993) p. 371–378.

[16] R. Pinnington and D. Lednik, *Transient energy flow between two coupled beams,* Journal of Sound and Vibration **189**, 265–287 (1996).

[17] K. S. Alfredsson, *Active and reactive structural energy flow.* ASME. J. Vib. Acoust. **119**, 70–79 (1997).

[18] S. V. Sorokin, J. B. Nielsen, and N. Olhoff, *Analysis and optimization of energy flows in structures composed of beam elements–part i: problem formulation and solution technique,* Structural and Multidisciplinary Optimization **22**, 3–11 (2001).

[19] O. Bouthier and R. Bernhard, *Simple models of energy flow in vibrating membranes,* Journal of Sound and Vibration **182**, 129–147 (1995).

[20] T. Balendra, *Vibration of buildings to wind and earthquake loads* (Springer-verlag, London, 1993).

[21] Y. Tamura and A. Kareem, *Advanced structural wind engineering.* (Springer Verlag, Japan, 2014).

[22] E. Simiu and R. H. Scanlan, *Wind Effects On Structures : An Introduction To Wind Engineering / Emil Simiu, Robert H. Scanlan* (Wiley New York, 1978).

[23] J. T. Snæbjörnsson and C. P. Geurts, *Modelling surface pressure fluctuations on medium-rise buildings,* Journal of Wind Engineering and Industrial Aerodynamics **94**, 845 (2006).

[24] B. J. Vickery, *On the Flow Behind a Coarse Grid and Its Use as a Model of Atmospheric Turbulence in Studies Related to Wind Loads on Buildings,* NPL Aero report (Department of Scientific and Industrial Research, National Physical Laboratory, Aerodynamics Division, 1965).

[25] D. L. Woodcock, *An introduction to random vibration,* The Journal of the Royal Aeronautical Society **68**, 570–570 (1964).

[26] H. A. Cole., *On-the-line analysis of random vibrations,* (American Institute of Aeronautics and Astronautics, 2018).

[27] H. A. Cole., *Failure detection of a space shuttle wing flutter model by random decrement,* Tech. Rep. (American Institute of Aeronautics and Astronautics, 1971).

7

[28] J. Butterworth, J. Hee Lee, and B. Davidson, *Experimental determination of modal damping from full scale testing,* in *Proceedings of the 13th World Conferene on Earthquake Engineering* (2004).

[29] A. P. Jeary, *The description and measurement of nonlinear damping in structures,* Journal of Wind Engineering and Industrial Aerodynamics **59**, 103 (1996).

[30] T. Kijewski-Correa and J. D. Pirnia, *Dynamic behavior of tall buildings under wind: insights from full-scale monitoring,* The Structural Design of Tall and Special Buildings **16**, 471.

[31] Q. Li, J. Wu, S. Liang, Y. Xiao, and C. Wong, *Full-scale measurements and numerical evaluation of wind-induced vibration of a 63-story reinforced concrete tall building,* Engineering Structures **26**, 1779 (2004).

[32] A. Jeary, *Establishing non-linear damping characteristics of structures from nonstationary response time-histories,* The Structural Engineer **70**, 61 (1992).

[33] B. R. Ellis, *The significance of dynamic soil-structure interaction in tall buildings, Ice Proceedings,* **81**, 221–242 (1986).

[34] P. W. Chen and L. E. Robertson, *Human perception thresholds of horizontal motion,* Journal of the structural division **92**, 1681–1695 (1972).

[35] R. J. Hansen, J. W. Reed, and E. H. Vanmarcke, *Human response to wind-induced motion of buildings, ASCE J Struct Div,* **99**, 1589–1605 (1973).

[36] A. Jeary, R. Morris, and R. Tomlinson, *Perception of vibration — test in a tall building,* Journal of Wind Engineering and Industrial Aerodynamics **28**, 361–370 (1988).

[37] H. v. Koten, *Grenzen voor dynamische bewegingen*, Tech. Rep. (TNO, 1967).

[38] B. de Saint-Venant, *Memoire sur la torsion des prismes: avec des considérations sur leur fléxion ainsi que sur l'équilibre intérieur des solides élastiques en général, et des formules pratiques pour le calcul de leur résistance à divers efforts s'exerçant simultanément* (S.l., 1853).

[39] V. Vlasov, *Thin-walled elastic beams* (National Technical Information Service, 1984).

[40] D. Ewins, *Modal Testing: Theory, Practice and Application* (Research Studies Press, 2000).

[41] B. Peeters and G. D. Roeck, *Stochastic system identification for operational modal analysis: A review,* ASME Journal of Dynamic systems, Measurement and Control **123**, 659–667 (2001).

[42] J. He and Z.-F. Fu, *Modal Analysis* (Butterworth-Heinemann, 2001).

[43] S. A. Neild, P. D. McFadden, and M. S. Williams, *A review of time-frequency methods for structural vibration analysis,* Journal of Engineering Structures **25**, 713–728 (2003).

7

[44] E. Sejdić, I. Djurović, and J. Jiang, *Time–frequency feature representation using energy concentration: An overview of recent advances,* Digital Signal Processing **19**, 153–183 (2009).

[45] H. Feichtinger and T. Strohmer, *Gabor Analysis and Algorithms: Theory and Applications*, Applied and Numerical Harmonic Analysis (Birkhäuser Boston, 2012).

[46] K. S. Tony L.Schmitz, *Mechanical vibrations* (Springer, 2012).

[47] S. S. Gómez and A. Metrekine, *Evaluation of the applicability of an energy method to calculate the damping in a lab-scale structure,* in *Procedia Engineering: X International Conference on Structural Dynamics (EURODYN)*, Vol. 199 (2017) p. 459–464.

[48] *Welkom | dinoloket,* https://www.dinoloket.nl/, accessed: 23-5- 2018.

[49] Hegazy, YA, and Mayne, *Statistical correlations between vs and cone penetration data for different soil types,* in *Proceedings, Cone Penetration Testing (CPT 1995)*, Vol. 2 (1995) p. 173–178.

[50] P. W. Mayne and G. J. Rix, *Correlations between shear wave velocity and cone tip resistance in natural clays,* Soils and Foundations **35**, 107–110 (1995).

[51] R. D. Andrus, N. P. Mohanan, P. Piratheepan, B. Ellis, and T. L. Holzer, *Predicting shear-wave velocity from cone penetration resistance,* in *Proceedings of the 4th International Conference on Earthquake Geotechnical Engineering* (2007).

[52] P. K. Robertson, *Interpretation of cone penetration tests — a unified approach,* Canadian Geotechnical Journal **46**, 1337–1355 (2009).

[53] G. A. Papagiannopoulos and G. D. Hatzigeorgiou, *On the use of the half-power bandwidth method to estimate damping in building structures,* Soil Dynamics and Earthquake Engineering **31**, 1075–1079 (2011).

[54] E. Kausel, *Early history of soil–structure interaction,* Soil Dynamics and Earthquake Engineering **30**, 822–832 (2010).

[55] M. Novak, *Dynamic stiffness and damping of piles,* Canadian Geotechnical Journal **11**, 574–598 (1974).

[56] G. Gazetas and N. Makris, *Dynamic pile-soil-pile interaction. part i: Analysis of axial vibration,* Earthquake Engineering & Structural Dynamics **20**, 115–132 (1991).

[57] B. Stankovic and T. M. Atanackovic, *Dynamics of a rod made of generalized kelvin–voigt visco-elastic material,* Journal of Mathematical Analysis and Applications **268**, 550–563 (2002).

[58] P. K. Pradhan, D. K. Baidya, and D. P. Ghosh, *Dynamic response of foundations resting on layered soil by cone model,* Soil Dynamics and Earthquake Engineering **24**, 425–434 (2004).

7

[59] M. Khakpour and M. H. Bonab, *Soil-structure-interaction using cone model in time domain for horizontal and vertical motions in layered half space,* Journal of Earthquake Engineering **0**, 1–26 (2018).

[60] J. Avilés and L. E. Pérez-Rocha, *Effects of foundation embedment during building–soil interaction,* Earthquake Engineering & Structural Dynamics **27**, 1523–1540 (1998).

[61] N. Makris and G. Gazetas, *Dynamic pile-soil-pile interaction. part ii: Lateral and seismic response,* Earthquake Engineering & Structural Dynamics **21**, 145–162 (1992).

[62] R. Dobry and G. Gazetas, *Simple method for dynamic stiffness a damping of floating pile groups, Geotechnique,* **38**, 557–574 (1988).

[63] G. Mylonakis, S. Nikolaou, and G. Gazetas, *Footings under seismic loading: Analysis and design issues with emphasis on bridge foundations,* Soil Dynamics and Earthquake Engineering **26**, 824–853 (2006).

[64] A. Maravas, G. Mylonakis, and D. L. Karabalis, *Simplified discrete systems for dynamic analysis of structures on footings and piles,* Soil Dynamics and Earthquake Engineering **61**, 29–39 (2014).

[65] S. Kocak and Y. Mengi, *A simple soil–structure interaction model,* Applied Mathematical Modelling **24**, 607–635 (2000).

[66] A. Kaynia and E. Kausel, *Dynamic stiffness and seismic response of pile groups,* NASA STI/Recon Technical Report N **83** (1982).

[67] J. Wolf, *Foundation vibration analysis using simple physical models* (Pretince Hall, 1995).

[68] J. P. Wolf and A. Deeks, *Foundation Vibration Analysis: A Strength of Materials Approach* (Elsevier Science, 2004).

[69] S. S. Gómez, C. P. W. Geurts, and A. Metrikine, *On the importance of soil damping for tall buildings loaded by wind,* Journal of Engineering Structures **163**, 426–435 (2018).

7

A

INTERFACE AND BOUNDARY CONDITIONS FOR EULER-BERNOULLI BEAM

A.1. COEFFICIENTS OF A BENDING BEAM EQUATION WITH FIXED-FREE BOUNDARY CONDITIONS

The coefficients of the boundary equations written in a matrix form, $\mathbf{A}(\beta_m)$, of a fixed-free beam are

$$
\begin{aligned}
a_{1,1} &= 1; a_{1,2} = 0; a_{1,3} = 1; a_{1,4} = 0 \\
a_{2,1} &= 0; a_{2,2} = \beta_m; a_{2,3} = 0; a_{2,4} = \beta_m \\
a_{3,1} &= \cosh(\beta_m L); a_{3,2} = \sinh(\beta_m L); a_{3,3} = -\cos(\beta_m L); a_{3,4} = -\sin(\beta_m L) \\
a_{4,1} &= -\sinh(\beta_m L); a_{4,2} = -\cosh(\beta_m L); a_{4,3} = -\sin(\beta_m L); a_{4,4} = \cos(\beta_m L)
\end{aligned}
\tag{A.1}
$$

with

$$
\beta_m = \frac{\omega_m^2 EI}{\rho A}
\tag{A.2}
$$

A.2. COEFFICIENTS OF A BENDING BEAM EQUATION WITH FLEXIBLE-FREE BOUNDARY CONDITIONS

The elements of the matrix $\mathbf{A}(\omega_n)$ describe the coefficients of the boundary and interface equations of a Euler-Bernoulli beam with flexible-free boundary conditions.

A

$$
\begin{aligned}
&a_{1,1} = EI; a_{1,2} = -\mathrm{i}C_{\theta m}^{\mathrm{SSI}}\omega - K_{\theta m}\beta_n; \\
&a_{1,3} = -EI; a_{1,4} = -\mathrm{i}C_{\theta m}^{\mathrm{SSI}}\omega - K_{\theta m}\beta_n; \\
&a_{1,5} = 0; a_{1,6} = 0; a_{1,7} = 0\, a_{1,8} = 0; \\
&a_{1,9} = 0; a_{1,10} = 0; a_{1,11} = 0; a_{1,12} = 0;
\end{aligned}
\tag{A.3}
$$

$$
\begin{aligned}
&a_{2,1} = -K_m; a_{2,2} = -EI\beta_n^3; \\
&a_{2,3} = -K_m; a_{2,4} = EI\beta_n^3; \\
&a_{2,5} = 0; a_{2,6} = 0; a_{2,7} = 0\, a_{2,8} = 0; \\
&a_{2,9} = 0; a_{2,10} = 0; a_{2,11} = 0; a_{2,12} = 0;
\end{aligned}
\tag{A.4}
$$

$$
\begin{aligned}
&a_{3,1} = -\cosh(\beta_n L_{\mathrm{l}}); a_{3,2} = -\sinh(\beta_n L_{\mathrm{l}}); a_{3,3} = -\cos(\beta_n L_{\mathrm{l}}); a_{3,4} = -\sin(\beta_n L_{\mathrm{l}}); \\
&a_{3,5} = \cosh(\beta_n L_{\mathrm{l}}); a_{3,6} = \sinh(\beta_n L_{\mathrm{l}})\, a_{3,7} = \cos(\beta_n L_{\mathrm{l}}); a_{3,8} = \sin(\beta_n L_{\mathrm{l}}); \\
&a_{3,9} = 0; a_{3,10} = 0; a_{3,11} = 0; a_{3,12} = 0;
\end{aligned}
\tag{A.5}
$$

$$
\begin{aligned}
&a_{4,1} = -\sinh(\beta_n L_{\mathrm{l}}); a_{4,2} = -\cosh(\beta_n L_{\mathrm{l}}); a_{4,3} = \sin(\beta_n L_{\mathrm{l}}); a_{4,4} = -\cos(\beta_n L_{\mathrm{l}}); \\
&a_{4,5} = \sinh(\beta_n L_{\mathrm{l}}); a_{4,6} = \cosh(\beta_n L_{\mathrm{l}}); a_{4,7} = -\sin(\beta_n L_{\mathrm{l}}); a_{4,8} = \sin(\beta_n L_{\mathrm{l}}); \\
&a_{4,9} = 0; a_{4,10} = 0; a_{4,11} = 1; a_{4,12} = 0;
\end{aligned}
\tag{A.6}
$$

$$
\begin{aligned}
&a_{5,1} = \mathrm{i}C_m\omega\cosh(\beta_n L_{\mathrm{l}}) - EI\beta_n^3\sinh(\beta_n L_{\mathrm{l}}); \\
&a_{5,2} = -EI\beta_n^3\cosh(\beta_n L_{\mathrm{l}}) + \mathrm{i}C_m\omega\sinh(\beta_n L_{\mathrm{l}}); \\
&a_{5,3} = \mathrm{i}C_m\omega\cos(\beta_n L_{\mathrm{l}}) - \sin(\beta_n L_{\mathrm{l}})EI\beta_n^3; \\
&a_{5,4} = EI\beta_n^3\cos(\beta_n L_{\mathrm{l}}) + \mathrm{i}C_m\omega\sin(\beta_n L_{\mathrm{l}}); \\
&a_{5,5} = EI\beta_n^3\sinh(\beta_n L_{\mathrm{l}}); a_{5,6} = EI\beta_n^3\cosh(\beta L_{\mathrm{l}}); a_{5,7} = \sin(\beta_n L_{\mathrm{l}})EI\beta_n^3; \\
&a_{5,8} = -EI\beta_n^3\cos(\beta_n L_{\mathrm{l}}); a_{5,9} = 0; a_{5,10} = 0; a_{5,11} = 0; a_{5,12} = 0;
\end{aligned}
\tag{A.7}
$$

$$
\begin{aligned}
&a_{6,1} = -EI\beta_n\cosh(\beta_n L_{\mathrm{l}}); a_{6,2} = -EI\beta_n\sinh(\beta_n L_{\mathrm{l}}); \\
&a_{6,3} = EI\beta_n\cos(\beta L_{\mathrm{l}}); a_{6,4} = \sin(\beta_n L_{\mathrm{l}})EI\beta_n; \\
&a_{6,5} = EI\beta_n\cosh(\beta_n L_{\mathrm{l}}); a_{6,6} = EI\beta_n\sinh(\beta_n L_{\mathrm{l}}); \\
&a_{6,7} = -EI\beta_n\cos(\beta_n L_{\mathrm{l}}); a_{6,8} = -\sin(\beta_n L_{\mathrm{l}})EI\beta_n; \\
&a_{6,9} = 0; a_{6,10} = 0; a_{6,11} = 0; a_{6,12} = 0;
\end{aligned}
\tag{A.8}
$$

$$
\begin{aligned}
&a_{7,1} = 0; a_{7,2} = 0; a_{7,3} = 1; a_{7,4} = 0; \\
&a_{7,5} = -\cosh(\beta_n L_{\mathrm{f}}); a_{7,6} = -\sinh(\beta_n L_{\mathrm{f}}); a_{7,7} = -\cos(\beta_n L_{\mathrm{f}}); a_{7,8} = -\sin(\beta_n L_{\mathrm{f}}); \\
&a_{7,9} = \cosh(\beta_n L_{\mathrm{f}}); a_{7,10} = \sinh(\beta_n L_{\mathrm{f}}); a_{7,11} = \cos(\beta_n L_{\mathrm{f}}); a_{7,12} = \sin(\beta_n L_{\mathrm{f}});
\end{aligned}
\tag{A.9}
$$

$$
\begin{aligned}
&a_{8,1} = 0; a_{8,2} = 0; a_{8,3} = 1; a_{8,4} = 0; a_{8,5} = -\sinh(\beta_n L_{\mathrm{f}}); a_{8,6} = -\cosh(\beta_n L_{\mathrm{f}}); \\
&a_{8,7} = \sin(\beta_n L_{\mathrm{f}}); a_{8,8} = -\cos(\beta_n L_{\mathrm{f}}); a_{8,9} = -\sinh(\beta_n L_{\mathrm{f}}); \\
&a_{8,10} = -\cosh(\beta_n L_{\mathrm{f}}); a_{8,11} = -\sin(\beta_n L_{\mathrm{f}}); a_{8,12} = \cos(\beta_n L_{\mathrm{f}});
\end{aligned}
\tag{A.10}
$$

$a_{9,1} = 0; a_{9,2} = 0; a_{9,3} = 0; a_{9,4} = 0;$

$a_{9,5} = iC_m\omega\cosh(\beta_n L_f) - EI\beta_n^3\sinh(\beta_n L_f); a_{9,6} = -\cosh(\beta_n L_f);$

$a_{9,7} = iC_m\omega\cos(\beta_n L_f) - \sin(\beta_n L_f)EI\beta_n^3; a_{9,8} = EI\beta_n^3\cos(\beta L_f) + i\sin(\beta_n L_f)C_m\omega;$ (A.11)

$a_{9,9} = EI\beta_n^3\sinh(\beta_n L_f); a_{9,10} = EI\beta_n^3\cosh(\beta_n L_f);$

$a_{9,11} = EI\beta_n^3\sin(\beta_n L_f); a_{9,12} = -\cos(\beta_n L_f)EI\beta_n^3;$

$$a_{10,1} = 0; a_{10,2} = 0; a_{10,3} = 0; a_{10,4} = 0;$$
$$a_{10,5} = -EI\beta_n\cosh(\beta_n L_f); a_{10,6} = -EI\beta_n\sinh(\beta L_f);$$
$$a_{10,7} = EI\beta_n\cos(\beta_n L_f); a_{10,8} = \sin(\beta_n L_f)EI\beta_n;$$ (A.12)
$$a_{10,9} = EI\beta_n\cosh(\beta_n L_f); a_{10,10} = EI\beta_n\sinh(\beta_n L_f);$$
$$a_{10,11} = -EI\beta_n\cos(\beta L_f); a_{10,12} = -\sin(\beta_n L_f)EI\beta_n;$$

$$a_{11,1} = 0; a_{11,2} = 0; a_{11,3} = 1; a_{11,4} = 0;$$
$$a_{11,5} = 0; a_{11,6} = 0; a_{11,7} = 0; a_{11,8} = 0;$$
$$a_{11,9} = EI\sinh(\beta_n L_{top}); a_{11,10} = EI\cosh(\beta_n L_{top});$$ (A.13)
$$a_{11,11} = EI\sin(\beta_n L_{top}); a_{11,12} = -EI\cos(\beta_n L_{top});$$

$$a_{12,1} = 0; a_{12,2} = 0; a_{12,3} = 1; a_{12,4} = 0;$$
$$a_{12,5} = 0; a_{12,6} = 0; a_{12,7} = 0; a_{12,8} = 1;$$
$$a_{12,9} = EI\cosh(\beta_n L_{top}); a_{12,10} = EI\sinh(\beta_n L_{top});$$ (A.14)
$$a_{12,11} = -EI\cos(\beta_n L_{top}); a_{12,12} = -EI\sin(\beta_n L_{top})$$

and,

$$\beta_n^4 = \sqrt{\frac{\rho A\omega_n^2}{EI}}.$$ (A.15)

A.3. Coefficients of a torsion beam equation with flexible-free boundary conditions

The elements of the matrix $\mathbf{B}(\omega_n)$ describe the coefficients of the boundary and interface equations of a torsion beam with flexible-free boundary conditions.

$a_{1,1} = GJ\beta_n; a_{1,2} = -K_{\theta x} - iC_{\theta x}^{SSI}; a_{1,3} = 0; a_{1,4} = 0; a_{1,5} = 0; a_{1,6} = 0;$

$a_{2,1} = -\sin(\beta_n L_l); a_{2,2} = -\cos(\beta_n L_l); a_{2,3} = \sin(\beta_n L_l); a_{2,4} = \cos(\beta_n L_l); a_{2,5} = 0; a_{2,6} = 0;$

$a_{3,1} = -GJ\beta_n\cos(\beta_n L_l) - iC_{\theta x}\omega\sin(\beta_n L_l); a_{3,2} = GJ\beta_n\sin(\beta_n L_l) - iC_{\theta x}\omega\cos(\beta_n L_l);$

$a_{3,3} = GJ\beta_n\cos(\beta_n L_l); a_{3,4} = -GJ\beta_n\sin(\beta_n L_l); a_{3,5} = 0; a_{3,6} = 0;$

$a_{4,1} = 0; a_{4,2} = 0; a_{4,3} = -\sin(\beta_n L_f); a_{4,4} = -\cos(\beta_n L_f); a_{4,5} = \sin(\beta_n L_f); a_{4,6} = \cos(\beta_n L_f)$

$a_{5,1} = 0; a_{5,2} = 0; a_{5,3} = -GJ\beta_n\cos(\beta_n L_f) - iC_{\theta x}\omega\sin(\beta_n L_f);$

$a_{5,4} = GJ\beta_n\sin(\beta_n L_f) - iC_{\theta x}\omega\cos(\beta_n L_f); a_{5,5} = GJ\beta_n\cos(\beta_n L_f); a_{5,6} = -GJ\beta_n\sin(\beta_n L_f)$

$a_{6,1} = 1; a_{6,2} = 0; a_{6,3} = 0; a_{6,4} = 0; a_{6,5} = GJ\cos(\beta_n L_{top}); a_{6,6} = -GJ\sin(\beta_n L_{top})$

(A.16)

and,

$$\beta_n^4 = \sqrt{\frac{\rho I_p \omega_n^2}{GJ}}.\tag{A.17}$$

A.4. Coordinate dependent solution of a Euler-Bernoulli beam for fixed-base and flexible-base boundary conditions

The coefficients of the coordinate dependent general solution for a fixed-base bending beam, $W_{\text{fix}}(z)$, was sought in the following form:

$$W(z) = C_1 \cosh(\beta_n z) + C_2 \sinh(\beta_n z) + C_3 \cos(\beta_n z) + C_4 \sin(\beta_n z)\tag{A.18}$$

where the constant $C_1..C_4$ are defined as:

$$C_1 = -C_3 = \frac{\sinh(\beta_n L) + \sin(\beta_n L)}{\cosh(\beta_n L) + \cos(\beta_n L)}; C_2 = -C_4 = 1.\tag{A.19}$$

For the case of the flexible foundation, the constant coefficients of, W_{flex}, read

$$C_1 = -\frac{EI^2\sinh(\beta_n L)\beta_n^4 - EI^2\sin(\beta_n L)\beta_n^4 + 2EIK_\theta\cos(\beta_n L)\beta_n^3 + K_\theta K_t * \sinh(\beta_n L) + K_\theta K_t\sin(\beta_n L)}{EI^2\cosh(\beta_n L)\beta_n^4 - EI^2\cos(\beta_n L)\beta_n^4 - 2EIK_t\sinh(\beta_n L)\beta_n - K_\theta K_t\cosh(\beta_n L) - K_\theta K_t\cos(\beta_n L)}$$

$$C_2 = \frac{EI^2\cosh(\beta_n L)\beta_n^4 - EI^2\cos(\beta_n L)\beta_n^4 + 2EIK_\theta\sin(\beta_n L)\beta_n^3 + K_\theta K_t * \cosh(\beta_n L) + K_\theta K_t\cos(\beta_n L)}{EI^2\cosh(\beta_n L)\beta_n^4 - EI^2\cos(\beta_n L)\beta_n^4 - 2EIK_t\sinh(\beta_n L)\beta_n - K_\theta K_t\cosh(\beta_n L) - K_\theta K_t\cos(\beta_n L)}$$

$$C_3 = -\frac{EI^2\sinh(\beta_n L)\beta_n^4 - EI^2\sin(\beta_n L)\beta_n^4 + 2EIK_\theta\cos(\beta_n L)\beta_n^3 + K_\theta K_t * \sinh(\beta_n L) + K_\theta K_t\sin(\beta_n L)}{EI^2\cosh(\beta_n L)\beta_n^4 - EI^2\cos(\beta_n L)\beta_n^4 - 2EIK_t\sinh(\beta_n L)\beta_n - K_\theta K_t\cosh(\beta_n L) - K_\theta K_t\cos(\beta_n L)}$$

$$C_4 = 1$$

$$\tag{A.20}$$

with

$$\beta_n^4 = \sqrt{\frac{\rho A \omega_n^2}{EI}}.\tag{A.21}$$

B

IMPLEMENTATION OF THE DYNAMIC STIFFNESS OF A FOUNDATION EMBEDDED IN A LAYERED HALF‑SPACE

In this Appendix, a procedure to compute the dynamic-stiffness matrix developed by Wolf [67] of a disk embedded in a layered soil (Fig. B.1) is described. By computing the dynamic-stiffness matrix, an equivalent frequency-dependent spring stiffness and dashpot damping for each DoF can be obtained. These values can be later used to parametrize the spring and dashpot elements of the model depicted in Fig .6.1b.

First, the radius of any cross-section of the cone depth can be determined as

$$r_{j+1} = \frac{z_{0j} + d_j}{z_{0j}} r_j. \tag{B.1}$$

The imaginary line described by the cone opening from the disk radius to the next disk in depth is linear with uniform properties. The dynamic-stiffness matrix, $S_j(\omega)$, depends on the soil properties, the geometry of the rigid disk and relates the dynamic loads and the motions.

$$\left\{ \begin{array}{c} P_j(\omega) \\ P_{j+1}(\omega) \end{array} \right\} = \left[S_j(\omega) \right] \left\{ \begin{array}{c} u_j(\omega) \\ u_{j+1}(\omega) \end{array} \right\} \tag{B.2}$$

To compute the dynamic-stiffness matrix, $S_j(\omega)$, a unitary dynamic load at the surface of the rigid disk is applied. The resultant motion of the wave pattern is described by a superposition of Green's functions corresponding to the double cones.

$$u_{11}(\omega) = 2g(0,\omega) + 4g(2d,\omega) + 4g(4d,\omega) + ...$$
$$u_{21}(\omega) = 4g(d,\omega) + 4g(3d,\omega) + 4g(5d,\omega) + ... \tag{B.3}$$
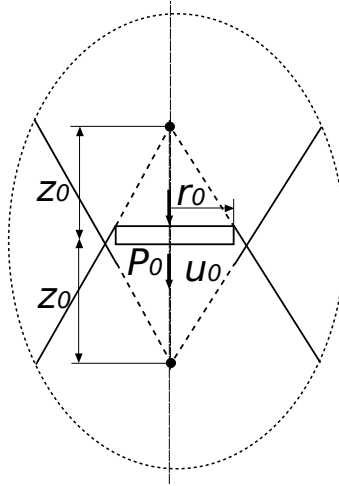
(a) Disk embedded in half-space with cone model.
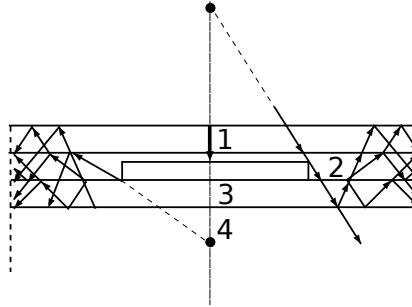
(b) Wave propagation in cone segments for embedded disk on layered half-space.

Figure B.1: Cone model for embedded foundations description.

where the Green's functions for the translational and rotational motions are

$$g^{\mathrm{t}}(d,\omega) = \frac{1}{2K^{\mathrm{t}}} \frac{1}{1+\frac{d}{z_0}} \frac{e^{-\mathrm{i}\frac{\omega d}{c}}}{1+\mathrm{i}\frac{\omega z_0}{c}} \tag{B.4}$$

and

$$g^{\theta}(d,\omega) = \frac{3}{2K^{\theta}} \left(\frac{1}{\left(1+\frac{d}{z_0}\right)^3} + \mathrm{i}\frac{\omega z_0}{c} \frac{1}{\left(1+\frac{d}{z_0}\right)^2} \right) \frac{e^{-\mathrm{i}\frac{\omega d}{c}}}{3+3\mathrm{i}\frac{\omega z_0}{c}+\left(\mathrm{i}\frac{\omega z_0}{c}\right)^2} \tag{B.5}$$

respectively. By introducing Eqs. B.4-B.5 into Eq. B.3, the displacement, u_{ij}, can be written as

$$u_{ij}(\omega) = \frac{T_{ij}^{\mathrm{t}}(\omega)}{S_1^{\mathrm{t}}(\omega)}. \tag{B.6}$$

The dynamic-flexibility matrix relates force and displacement and can be described as follows:

$$\left\{ \begin{array}{c} u_j(\omega) \\ u_{j+1}(\omega) \end{array} \right\} = \left[\begin{array}{cc} \frac{T_{i,j}^{\mathrm{t}}(\omega)}{S_j^{\mathrm{t}}(\omega)} & \frac{T_{i,j+1}^{\mathrm{t}}(\omega)}{S_{j+1}^{\mathrm{t}}(\omega)} \\ \frac{T_{i+1,j}^{\mathrm{t}}(\omega)}{S_j^{\mathrm{t}}(\omega)} & \frac{T_{i+1,j+1}^{\mathrm{t}}(\omega)}{S_{j+1}^{\mathrm{t}}(\omega)} \end{array} \right] \left\{ \begin{array}{c} P_j(\omega) \\ P_{j+1}(\omega) \end{array} \right\}. \tag{B.7}$$

Inverting Eq. B.7:

$$\left\{ \begin{array}{c} P_j(\omega) \\ P_{j+1}(\omega) \end{array} \right\} = \frac{S_j^{\mathrm{t}}(\omega) S_{j+1}^{\mathrm{t}}(\omega)}{T_{i,j}^{\mathrm{t}}(\omega) T_{i+1,j+1}^{\mathrm{t}}(\omega) - T_{i,j+1}^{\mathrm{t}}(\omega) T_{i+1,j}^{\mathrm{t}}(\omega)} \left[\begin{array}{cc} \frac{T_{i+1,j+1}^{\mathrm{t}}(\omega)}{S_{j+1}^{\mathrm{t}}(\omega)} & -\frac{T_{i+1,j}^{\mathrm{t}}(\omega)}{S_j^{\mathrm{t}}(\omega)} \\ -\frac{T_{i,j+1}^{\mathrm{t}}(\omega)}{S_{j+1}^{\mathrm{t}}(\omega)} & \frac{T_{i,j}^{\mathrm{t}}(\omega)}{S_j^{\mathrm{t}}(\omega)} \end{array} \right] \left\{ \begin{array}{c} u_j(\omega) \\ u_{j+1}(\omega) \end{array} \right\}. \tag{B.8}$$

The dynamic-stiffness matrix can be computed.

$$\left[S^{\mathrm{t}}(\omega) \right] = \frac{S_j^{\mathrm{t}}(\omega)}{T_{i,j}^{\mathrm{t}}(\omega) T_{i+1,j+1}^{\mathrm{t}}(\omega) - T_{i,j+1}^{\mathrm{t}}(\omega) T_{i+1,j}^{\mathrm{t}}(\omega)} \left[\begin{array}{cc} T_{i+1,j+1}^{\mathrm{t}}(\omega) & -\frac{S_{j+1}^{\mathrm{t}}(\omega)}{S_j^{\mathrm{t}}(\omega)} T_{i+1,j}^{\mathrm{t}}(\omega) \\ -T_{i,j+1}^{\mathrm{t}}(\omega) & \frac{S_{j+1}^{\mathrm{t}}(\omega)}{S_j^{\mathrm{t}}(\omega)} T_{i,j}^{\mathrm{t}}(\omega) \end{array} \right] \tag{B.9}$$

where

$$T_{i,j}^{\mathrm{t}}(\omega) = 1 + 2 \sum_{n=1}^{\infty} \frac{e^{-\mathrm{i}n\omega T}}{1 + n\frac{2d}{z_0}}$$

$$T_{i+1,j}^{\mathrm{t}}(\omega) = 2 \sum_{n=1}^{\infty} \frac{e^{-\mathrm{i}(n-0.5)\omega T}}{1 + (n-0.5)\frac{2d}{z_0}}$$

$$T_{i,j+1}^{\mathrm{t}}(\omega) = 2 \sum_{n=1}^{\infty} \frac{e^{-\mathrm{i}(n-0.5)\omega T}}{1 + (n-0.5)\frac{2d}{z_0+d}} \tag{B.10}$$

$$T_{i+1,j+1}^{\mathrm{t}}(\omega) = 1 + 2 \sum_{n=1}^{\infty} \frac{e^{-\mathrm{i}n\omega T}}{1 + n\frac{2d}{z_0+d}}$$

and

$$S_j^{\mathrm{t}}(\omega) = K_j^{\mathrm{t}} \left(1 + \mathrm{i}\frac{\omega z_0}{c} \right)$$

$$S_{j+1}^{\mathrm{t}}(\omega) = K_{j+1}^{\mathrm{t}} \left(1 + \mathrm{i}\frac{\omega(z_0+d)}{c} \right) \tag{B.11}$$

and

B

$$K_j^{\mathrm{t}} = \frac{\rho c^2 \pi r_j^2}{z_0}$$

$$K_{j+1}^{\mathrm{t}} = \frac{\rho c^2 \pi r_{j+1}^2}{z_0 + d}$$

(B.12)

with $T = 2d/c$. For the rotational DoF, the dynamic-stiffness matrix can be computed following the same procedure. Therefore, the dynamic-stiffness matrix appears as follows:

$$\left[S^\theta(\omega)\right] = \frac{S_j^\theta(\omega)}{T_{i,j}^\theta(\omega)\,T_{i+1,j+1}^\theta(\omega) - T_{i,j+1}^\theta(\omega)\,T_{i+1,j}^\theta(\omega)} \begin{bmatrix} T_{i+1,j+1}^\theta(\omega) & -\frac{S_{j+1}^\theta(\omega)}{S_j^\theta(\omega)}\,T_{i+1,j}^\theta(\omega) \\[2mm] -T_{i,j+1}^\theta(\omega) & \frac{S_{j+1}^\theta(\omega)}{S_j^\theta(\omega)}\,T_{i,j}^\theta(\omega) \end{bmatrix}$$

(B.13)

with,

$$T_{i,j}^\theta(\omega) = 1 + 2 \sum_{n=1}^{\infty} e^{-\mathrm{i}n\omega T}\left(\frac{1}{\left(1+n\frac{2d}{z_0}\right)^2} + \left(\frac{1}{\left(1+n\frac{2d}{z_0}\right)^3} - \frac{1}{\left(1+n\frac{2d}{z_0}\right)^2}\right)\frac{1}{\left(1+\mathrm{i}\frac{\omega z_0}{c}\right)}\right)$$

$$T_{i+1,j}^\theta(\omega) = 2 \sum_{n=1}^{\infty} e^{-\mathrm{i}(n-0.5)\omega T}$$

$$\left(\frac{1}{\left(1+(n-0.5)\frac{2d}{z_0}\right)^2} + \left(\frac{1}{\left(1+(n-0.5)\frac{2d}{z_0}\right)^3} - \frac{1}{\left(1+(n-0.5)\frac{2d}{z_0}\right)^2}\right)\frac{1}{\left(1+\mathrm{i}\frac{\omega z_0}{c}\right)}\right)\omega T$$

$$T_{i,j+1}^\theta(\omega) = 2 \sum_{n=1}^{\infty} e^{-\mathrm{i}(n-0.5)\omega T}$$

$$\left(\frac{1}{\left(1+(n-0.5)\frac{2d}{z_0+d}\right)^2} + \left(\frac{1}{\left(1+(n-0.5)\frac{2d}{z_0+d}\right)^3} - \frac{1}{\left(1+(n-0.5)\frac{2d}{z_0+d}\right)^2}\right)\frac{1}{\left(1+\mathrm{i}\frac{\omega z_0+d}{c}\right)}\right)\omega T$$

$$T_{i+1,j+1}^\theta(\omega) = 1 + 2 \sum_{n=1}^{\infty} e^{-\mathrm{i}n\omega T}\left(\frac{1}{\left(1+n\frac{2d}{z_0+d}\right)^2} + \left(\frac{1}{\left(1+n\frac{2d}{z_0+d}\right)^3} - \frac{1}{\left(1+n\frac{2d}{z_0+d}\right)^2}\right)\frac{1}{\left(1+\mathrm{i}\frac{\omega z_0+d}{c}\right)}\right)$$

(B.14)

and,

$$S_j^\theta(\omega) = K_j^\theta \left(1 - \frac{1}{2} \frac{\left(\frac{\omega z_0}{c}\right)^2}{1 + \left(\frac{\omega z_0}{c}\right)^2} + i \frac{\omega z_0}{3c} \frac{\left(\frac{\omega z_0}{c}\right)^2}{\left(1 + \frac{\omega z_0}{c}\right)^2} \right)$$

$$S_{j+1}^\theta(\omega) = K_{j+1}^\theta \left(1 - \frac{1}{2} \frac{\left(\frac{\omega(z_0+d)}{c}\right)^2}{1 + \left(\frac{\omega(z_0+d)}{c}\right)^2} + i \frac{\omega(z_0+d)}{3c} \frac{\left(\frac{\omega(z_0+d)}{c}\right)^2}{\left(1 + \frac{(\omega z_0+d)}{c}\right)^2} \right) \tag{B.15}$$

B

and,

$$K_j^\theta = \frac{3\rho c^2 \pi r_0^4}{4 z_0}$$

$$K_{j+1}^\theta = \frac{3\rho c^2 \pi r_0^4}{4(z_0+d)}. \tag{B.16}$$

Moreover, the dynamic-flexibility matrix is not symmetric as can be noted from the transfer function coefficients, $T_{i,j}$, where $i = 1, 2$ and $j = 1..N_{\text{layers}}$.

Finally, by computing $S^t(\omega)$ and $S^\theta(\omega)$, the stiffness and damping function of the frequency can be obtained. This is done by relating the real part of the dynamic stiffness matrix to the spring stiffness and the imaginary part to the damping, which corresponds to the geometrical damping. The soil material damping can be considered in the computation of the dynamic stiffness matrix as an additional damping through the complex-valued wave speed, as shown in Eq. B.17.

$$c \rightarrow c\sqrt{1 + 2i\xi_s} \approx c(1 + i\xi_s) \tag{B.17}$$

$c = c_s$ for the transverse and torsional DoFs, and $c = c_p$ for the translational and rotational DoFs.

C

CROSS-SECTIONAL CONSTANTS OF THE PRISMATIC BEAMS

The integrals of the cross-sectional constants are

$$
\begin{aligned}
&A = \int_A \mathrm{d}A \qquad A_y = \alpha_y A \qquad A_z = \alpha_z A \\
&R_y = \int_A \left(\frac{\partial \omega}{\partial y} - z \right) \mathrm{d}A \qquad R_z = \int_A \left(\frac{\partial \omega}{\partial y} + y \right) \mathrm{d}A \\
&S_y = \int_A z \, \mathrm{d}A \qquad S_z = \int_A y \, \mathrm{d}A \qquad S_\omega = \int_A \omega \, \mathrm{d}A \\
&I_{yy} = \int_A z^2 \, \mathrm{d}A \qquad I_{zz} = \int_A y^2 \, \mathrm{d}A \qquad I_{yz} = \int_A yz \, \mathrm{d}A \\
&I_{\omega y} = \int_A y\omega \, \mathrm{d}A \qquad I_{\omega z} = \int_A z\omega \, \mathrm{d}A \\
&K = \int_A \left(y^2 + z^2 + y \frac{\partial \omega}{\partial z} - z \frac{\partial \omega}{\partial y} \right) \mathrm{d}A.
\end{aligned}
\tag{C.1}
$$

D

EQUIVALENCE OF WORK OF THE MOMENT AND SHEAR FORCE IN THE ENERGY FLUX OF A EULER-BERNOULLI BEAM

The energy flux through a cross-section of a Euler-Bernoulli bending beam can be described as

$$S(z,t) = EI \left(\frac{\partial^2 w(z,t)}{\partial z^2} \frac{\partial^2 w(z,t)}{\partial z \partial t} - \frac{\partial^3 w(z,t)}{\partial z^3} \frac{\partial w(z,t)}{\partial t} \right) =$$
$$M \frac{\partial^2 w(z,t)}{\partial z \partial t} - Q \frac{\partial w(x,t)}{\partial t}. \tag{D.1}$$

Assuming the displacement, $w(z,t)$, in the form of a travelling wave, $w(z,t) = W_0 \sin(\omega t - kz)$, the following expression for the energy flux can be obtained:

$$S(z,t) = M \frac{\partial^2 w(z,t)}{\partial z \partial t} - Q \frac{\partial w(x,t)}{\partial t} = W_0^2 k^3 \omega EI \left(\cos^2(\omega t - kz) + \sin^2(\omega t - kz) \right) \tag{D.2}$$

Next, by using the following trigonometric relations

$$\sin^2(\alpha) = \frac{1}{2} + \frac{1}{2} \cos(2\alpha) \tag{D.3}$$

and

$$\cos^2(\alpha) = \frac{1}{2} - \frac{1}{2} \cos(2\alpha) \tag{D.4}$$

one can show that for, $w(z, t) = W_0 \sin(\omega t - kz)$,

$$\overline{M \frac{\partial^2 w(z, t)}{\partial z \partial t}} = \frac{1}{T} \int_0^T M \frac{\partial^2 w(z, t)}{\partial z \partial t} dt = \frac{1}{2} EI W_0^2 k^3 \omega \tag{D.5}$$

and

$$-\overline{Q \frac{\partial w(z, t)}{\partial t}} = \frac{1}{T} \int_0^T Q \frac{\partial w(z, t)}{\partial t} dt = \frac{1}{2} EI W_0^2 k^3 \omega \tag{D.6}$$

therefore

$$\overline{S} = \frac{1}{T} \int_0^T S(z, t) dt = 2M \frac{\partial^2 w(z, t)}{\partial z \partial t}. \tag{D.7}$$

In the above expressions $T = \frac{2\pi}{\omega}$. It is known that this approximation can also be applied to more complex wave trains in the beam.

SAMENVATTING

Gebouwen worden hoger, lichter en slanker. Deze veranderende eigenschappen maken hoge gebouwen gevoeliger voor omgevingsbelastingen zoals windvlagen. Een gebouw wordt als "hoog" beschouwd wanneer zijn hoogte en slankheid het ontwerp beïnvloeden. Gegeven de vraag naar verbeterende prestaties van gebouwen is de bruikbaarheidsgrenstoestand het belangrijkste criterium voor het ontwerp van hoge gebouwen. The structurele bruikbaarheid is direct gerelateerd aan de bewegingen van een gebouw onder invloed van windvlagen. Deze bewegingen kunnen het welzijn van mensen in het gebouw beïnvloeden. Terwijl de menselijke waarneming van bewegingen gebaseerd is op het voelen van schokken, is de versnelling algemeen geaccepteerd als parameter voor het meten van het comfortniveau. In de literatuur zijn er enkele gevestigde criteria te vinden om de menselijke perceptie van trillingen in gebouwen te bepalen. In dit werk worden de Van Koten-criteria toegepast om de menselijke waarneming van trillingen in gebouwen te bestuderen aan de hand van data die is verkregen bij verschillende metingen van bestaande hoogbouw in Nederland. Terwijl de resultaten duidelijk laten zien dat versnellingen nauwelijks waar te nemen zijn, voelen mensen in bestaande hoogbouw zich vaak onveilig, waar uit blijkt dat de menselijke perceptie zeer subjectief is. Het gedrag van dynamische systemen wordt bepaald door zijn massa, demping en stijfheid. De demping kan beschouwd worden als de oorzaak van energieverlies in het systeem. Daarom bepaald het de maximale versnelling die gevoeld kan worden. Vanwege zijn fysieke complexiteit is de demping de meest onzekere parameter om te voorspellen. Momenteel zijn er verschillende demping predictors om demping in hoge gebouwen te bepalen. The totale demping die verkregen wordt via demping predictors volgt uit contributies van twee bronnen, namelijk het energieverlies in de interactie tussen grond en fundering en het energieverlies in de constructie. In principe zijn dit de twee voornaamste bronnen van energieverlies in hoge gebouwen. Bij het gebruik van deze predictors is de demping die volgt uit de interactie tussen grond en fundering een constante waarde, terwijl de demping in de constructie toeneemt met de amplitude van de trillingen in het gebouw. Het gebruik van deze predictors leidt helaas tot een grote spreiding van de dempingwaardes in vergelijking met de dempingwaardes die bij metingen zijn vastgesteld voor de hoogbouw in Nederland. Aangezien de parameters voor deze predictors zijn bepaald aan de hand van data verkregen bij metingen aan bestaande hoogbouw is het moeilijk om het verschil tussen de gemeten dempingwaardes voor hoge gebouwen en de resulterende waardes die volgen uit de demping predictors uit te leggen. In dit werk wordt een predictor gepresenteerd en toegepast die is gebaseerd op dezelfde principes en die is afgestemd om overeen te komen met de data die verkregen is bij metingen van bestaande hoogbouw. Deze predictor geeft helaas niet voldoende inzicht om het gedrag van de mechanismes van energieverlies in hoge gebouwen te begrijpen. Het is daarom het doel van deze dissertatie om een hulpmiddel te ontwikkelen om het energieverlies in gebouwen beter te kunnen bepalen en daarbij de prognose van de demping te verbeteren. In

hoge gebouwen zijn er drie voorname types van energieverlies (i.e. energieverlies in de constructie, energieverlies in de grond en energieverlies door wind om het gebouw). In dit werk is aangenomen dat de aerodynamische demping door de wind om een gebouw nihil is. Om een betere prognose te verkrijgen van de algehele demping is er een poging gedaan om de contributies van de verschillende bronnen van demping aan de algehele demping vast te stellen. Omdat windbelastingen geen hogere frequentiemodes kunnen opwekken in hoge gebouwen, kan het energieverlies van specifieke delen van de constructie niet adequaat geïdentificeerd worden aan de hand van technieken gebaseerd op modale analyse. Daarom is er een andere aanpak nodig die het energieverlies van specifieke delen van de constructie kan bepalen zonder een modale beschrijving van de constructie. In deze dissertatie wordt energieflux-analyse voorgesteld als een hulpmiddel om demping te identificeren. In deze methode wordt een lokaal deel van de constructie geïsoleerd om van dat gedeelte de energiebalans op te stellen. De verbinding van dit lokale deel met de rest van de constructie vind plaats via de energieflux, die voor dit gedeelte de inkomende en uitgaande energie beschrijft. Met behulp van deze analyse kan de demping van een deel van de constructie worden vastgesteld. In hoofdstukken 4 en 5 wordt de energieflux-analyse toegepast om voor verschillende delen van de constructie het energieverlies te bepalen. Daarna kan er een operator voor de demping worden gekwantificeerd. Een bijkomend voordeel van deze methode is de mogelijkheid om het gedrag van verschillende demping-operators te bestuderen door het bijbehorende energieverlies voor elke operator te berekenen. Om de methode te valideren zijn er twee schaalmodellen van de constructie, zijnde een schaalmodel van een balk en een schaalmodel van een stalen gebouwframe, en een hoog gebouw op werkelijke schaal gebruikt. En wel op de volgende manier. Als eerste is het schaalmodel van de balk uitgerust met versnellingsmeters, terwijl het schaalmodel van het stalen gebouwframe en het hoge gebouw op werkelijke schaal zijn uitgerust met versnellingsmeters en rekstrookjes. Aan de hand van de verzamelde data is vervolgens de viskeuze demping bepaald. Daarnaast is er ook een analytisch model voor elke constructie ontwikkeld dat bestaat uit continue en discrete elementen (e.g. balken, veren, dempers). Deze modellen zijn gebruikt om de energieverandering, de energieflux en het energieverlies te interpreteren. Ook voor het model kan de energiebalans opgesteld worden voor een specifiek onderdeel van de constructie. Door gebruik van de testdata kan dan de energie in dit gebied van een constructie berekend worden en kan het bijbehorende energieverlies geïdentificeerd worden. Om percentages van de kritische demping te vergelijken wordt het energieverlies uitgedrukt in termen van een demping-operator. Deze constante kan toegepast worden om de equivalente viskeuze demping te berekenen door gebruik te maken van de energieflux-analyse en deze te vergelijken met de equivalente dempingwaardes die in de testen geïdentificeerd zijn. De resultaten gepresenteerd in deze dissertatie bewijzen dat deze methode een consistent kader geeft voor de identificatie van de demping. In hoofdstuk 6 is een basismodel gepresenteerd waarmee de demping in hoogbouw bepaald kan worden gedurende de ontwerpfase. De interactie tussen grond en fundering is hierbij beschreven door het conusmodel en het gebouw wordt vertegenwoordigd door een Euler-Bernoulli-balk. Aannemende dat er een klein trillingsveld is, is verondersteld dat het mechanisme dat verantwoordelijk is voor het energieverlies direct gerelateerd is aan de vervorming van het gebouw. Daarom is de invloed van de demping in het gebouw

bestudeerd op basis van het balkmodel dat het gebouw representeert. Deze invloed varieert afhankelijk van de rotatie van het gebouw zoals deze veroorzaakt wordt door verschillende stijfheden van de fundering. Op dezelfde wijze varieert de demping door de interactie tussen grond en fundering afhankelijk van de stijfheid in de interactie tussen grond en fundering. De resultaten tonen aan dat voor hoge gebouwen, de interactie tussen grond en fundering mogelijk een belangrijke rol speelt bij de identificatie van de algehele demping voor bepaalde grondeigenschappen, zoals die van grondsoorten die in Nederland voorkomen.

PUBLICATIONS BY THE AUTHOR

JOURNAL PUBLICATIONS

1. **S.S. Gómez**, A. Metrikine, B. Carboni, and W. Lacarbonara. Identification of Energy Dissipation in Structural Joints by Means of the Energy Flow Analysis. *Journal of Vibration and Acoustics*, 140(1):011007-011007-8, 2017.

2. **S.S. Gómez**, C.P.W. Geurts, and A. Metrikine. On the importance of soil damping for tall buildings loaded by wind. *Journal of Engineering Structures*, 163:426-435, 2018.

3. **S.S. Gómez**, and A. Metrikine. The energy flow analysis as a tool for identification of damping in tall buildings subjected to wind: Contributions of the foundation and the building structure. *Journal of Vibration and Acoustics*, 141(1):011013-011013-11, 2018.

CONFERENCE PUBLICATIONS

1. **S.S. Gómez**, and A. Metrikine. Evaluation of the applicability of an energy method to calculate the damping in a lab-scale structure. *Procedia Engineering: X International Conference on Structural Dynamics (EURODYN)*, 199:459-464, 2017.

2. **S.S. Gómez**, and J. Pruiksma. Effects of Soil-Structure in High-Rise Buildings by Means of Dimensionless Analysis and a Simplified Model. *High Tech Concrete: Where Technology and Engineering Meet (Fib symposium)*, Springer International Publishing 1371-1379, 2017.

3. **S.S. Gómez**, M.I. Badila, and A. Metrikine. Evaluation of the applicability of the LuGre model for modelling the dynamic behaviour of bolt connected frames. *5th ECCOMAS Thematic Conference on, Computational Methods in Structural Dynamics and Earthquake Engineering (COMPDYN)*, 199:459-464, Crete Island, Greece, May 2015.

TECHNICAL MAGAZINE PUBLICATIONS

1. C.P.W. Geurts, C. van Bentum, J. Pruiksma, and **S. S. Gómez**. Involved bodem op demping hoogbouw (*In Dutch*). *Cement Technical Magazine*, 2016.

2. C.P.W. Geurts, C. van Bentum, **S.S. Gómez**, and S. van Dijk. Demping hoogbouw voorspeld (*In Dutch*), *Cement Technical Magazine*, 2015.

CURRICULUM VITÆ

Sergio SÁNCHEZ GÓMEZ

06-11-1984   Born in Reus, Catalunya.

EDUCATION

2003-2008   Ingeniero Técnico Ind. Mecánica
                   Escola Tècnica Superior d'Enginyeria
                   University Rovira i Virgili, Spain

2008-2012   Ingeniero Industrial
                   Centro Politécnico Superior
                   University of Zaragoza, Spain

2014-2018   PhD. Research
                   Technical University of Delft, The Netherlands
                   Faculty of Civil Engineering and Geosciences
                   Section of Structural Mechanics
                   Dynamics of Solids and Structures

PROFESSIONAL

2012-2014   Reseach Engineer
                   R & D Department
                   Ballast Nedam

2014-2018   Scientist Innovator
                   Structural Dynamics Department
                   TNO

2018-present   Post-Doc researcher
                   Technical University of Delft, The Netherlands
                   Faculty of Civil Engineering and Geosciences
                   Section of Offshore Engineering
                   Hydraulic Engineering